**This electronic thesis or dissertation has been downloaded from Explore Bristol Research, http://research-information.bristol.ac.uk**

*Author:*
**Willson, Jolyon**

*Title:*
**Parvocellular and magnocellular responses in peripheral vision**

**Parvocellular and Magnocellular Responses in Peripheral Vision**

Jolyon Willson

University of Bristol

A dissertation submitted to the University of Bristol in accordance with the
requirements for award of the degree of Master of Science by Research in the Faculty of Life
Sciences

School of Psychological Science

September 2022

Word count: 20,477

# Abstract

Direct psychophysical discrimination of the spatial and temporal characteristics of the retinal magnocellular and parvocellular pathways in the primate visual system has proved elusive. However, the results of the experiment reported here suggest that such discrimination is possible using stimuli tailored to the underlying physiology of the M and P retinal ganglion cells. To maximise the sensitivity, the visual stimuli used were tangential sinusoidal gratings with a linearly varying spacing matched to the retinal ganglion cell spacing. The results - support the hypothesised dual-segment characteristic of the contrast sensitivity function and are consistent with the known contrast gain and spatial physiological characteristics of the P and M pathways in the primate visual system. The results are consistent with previous observations that the overall system response is that of the most sensitive of the two channels at a given contrast, rather than summing the two channel responses.

In order to visualise how the two pathways transmit visual information to the lateral geniculate nucleus (LGN) and the higher visual areas, I developed a simple algorithm for determining local contrast as a function of scale in natural images, allowing the derivation of contrast heat maps. The algorithm was validated using simple sine wave images and the results on natural images were consistent with previous studies. I then used the same algorithm to plot contrast response images at the characteristic scales of the M and P pathways, which allowed visualisation of the spatial contrast responses of two pathways at an eccentricity of 23.5 degrees. The visualisation can be interpreted as indicating that the P and M pathways perform different filter functions of edge enhancement and contrast enhancement, respectively.

**Dedication and Acknowledgements**

I'm not sure that Iain Gilchrist fully understood what he was taking on when he agreed to supervise me for this MScR. He kindly humoured me in the initial stages when we discussed my interests and ideas, and then gave patient help, guidance, and challenges as I worked through the project. It's been an enjoyable and enlightening journey from physics to psychophysics and like all good research it has shown me that my ignorance is boundless. Thank you, Iain. I'd also like to thank Cas Ludwig for his insight and clear thinking, and to the other members of staff in the School for their help and assistance.

Many thanks also to my fellow postgrads in No. 5 for their support and friendly acceptance of a Boomer in their midst. And not least the entertaining and occasionally eccentric conversations at lunchtimes.

Lastly but most importantly, I'd like to thank my wife Heather for her encouragement and support for this endeavour over the last three years.

# Author's Declaration

I declare that the work in this dissertation was carried out in accordance with the requirements of the University's *Regulations and Code of Practice for Research Degree Programmes* and that it has not been submitted for any other academic award. Except where indicated by specific reference in the text, the work is the candidate's own work. Work done in collaboration with, or with the assistance of, others, is indicated as such. Any views expressed in the dissertation are those of the author.

SIGNED:                                        DATE: 15th September 2022

**Table of Contents**

(Reproduced from Rovamo, Virsu, & Nasanen, 1978). (D) Temporal CSF, as a function of adaptation for luminance values 0.06 to 9300 trolands (Reproduced from Kelly, 1961).

**Figure 2**. (A) Model of the achromatic contrast sensitivity function from Kulikowski (Reproduced from J.J. Kulikowski, 1987). (B) Model of combined response of an array of P and M RGCs from Kaplan (Reproduced from Kaplan, Lee, & Shapley, 1990).

**Figure 3.** (A) Schematic of the human eye (Reproduced from Sekuler & Blake, 2006). (B) Modulation transfer function (MTF) as a function of eccentricity for horizontal meridian in temporal, determined at circle of east confusion (Reproduced from Navarro, Artal, & Williams, 1993).

**Figure 4.** (A) Schematic of main neurons in the primate retina (Reproduced from Sekuler & Blake, 2006). (B) Images of horizontal (top) and vertical (bottom) cross-sections of human fovea (Reproduced from Bringmann et al., 2018).

**Figure 5**. Relative sensitivity of the L, M and S cones as a function of wavelength (Reproduced from Solomon & Lennie, 2007).

**Figure 6**. Distribution of the cones and rods as a function of eccentricity (along the horizontal meridian) (Reproduced from Sekuler & Blake, 2006).

**Figure 7.** Luminance sensitivity of the human visual system (Reproduced from D. Cao, 2013)

**Figure 8.** Contrast gain functions of the magnocellular and parvocellular retinal ganglion cells (based on data from (Kaplan & Shapley, 1986))

**Figure 9.** (A) Spatial centre/surround structure for "Difference of Gaussian" RGC sensitivity model, with the blue, red and yellow lines being the centre, surround and DoG responses respectively.

**Figure 10**. Frequency response as a function of spatial frequency for different centre-surround structures. The orange line corresponds to a centre/surround weighting of 10:1, showing a strong bandpass response. The blue line corresponds to a centre/surround weighting of 100:1, showing a band-pass response.

**Figure 11.** Dendritic field diameters as a function of eccentricity for midget (P, parvocellular) signified by the small circles and parasol (M, magnocellular) retinal ganglion cells signified by the large circles. The filled circles are for the nasal quadrant and the unfilled circles for the other quadrants. (Reproduced from Figure 2(b) from (Dacey & Petersen, 1992))

**Figure 12.** Centre radius of receptive fields of primate parvocellular and magnocellular retinal ganglion cells (Reproduced from Croner & Kaplan, 1995).

**Figure 13.** (A) Cone density as a function of eccentricity for the four meridians (Reproduced from Watson, 2014, after Curcio et al, 1990). (B) P RGC density as a function of eccentricity for the four meridians (Reproduced from Watson, 2014, after Curcio et al, 1990).

**Figure 14**. Array spacing as a function of eccentricity for the four meridians, including the overall mean and the mean for the horizontal meridian (Reproduced from Watson, 2014).

**Figure 15.** Comparison of dendritic field diameter vs eccentricity to the P RGC spacing. The black and white circles are dendritic field sizes for individual nasal and non-nasal meridians respectively and the red and blue lines are the RGC array spacing fits for nasal and non-nasal meridians, respectively (Reproduced from Watson, 2014, with dendritic field size data after Dacey, 1993).

**Figure 16** (A). Population receptive field (pRF) as a function of eccentricity for the primary areas in the visual cortex determined using fMRI (V1-V3AB are in the primary visual cortex and V01-2, LO1-2 and TO1-2 are the ventral occipital, lateral occipital, and temporal occipital regions (Reproduced from Wandell & Winawer, 2015). (B) Visualisation of the variation of the RF diameter as a function of eccentricity for V1, V2 and hV4 (Reproduced from Wandell and Winawer, 2015).

**Figure 17.** Example of a test stimulus with a scale factor of 0.016 and 50% Michelson contrast, at a nominal 23.5° eccentricity. The white dot on the right-hand side is the fixation point.

**Figure 18.** Example cut-off wavelength data for JW (blue), NM (magenta) and TH (green) for 10Hz temporal modulation. The solid and dotted curves are dual-segment model fits discussed in the "Model Fitting" section. The error bars are the 95% confidence limits.

**Figure 19.** Contrast sensitivity functions for JW (top row), NM (middle row) and TH (bottom row), at 2Hz, 10Hz, 30Hz and 60Hz temporal modulation. The red and blue curves are the model fit for a 16-parameter frequency Gaussian model discussed in the Results section.

**Figure 20.** Inferred peak temporal contrast sensitivity functions at 2.5 cpd based on the 16-parameter frequency Gaussian model for JW, NM, and TH combined dataset (Table 3). The blue curve is for the low-contrast segment, and the red curve is for the high-contrast segment.

**Figure 21.** Top row is based on the MTF-corrected P pathway data. (A) is the frequency Gaussian model (black dashed line) fitted to the frequency DoG (green line), with estimated centre and surround functions shown in mauve and blue, respectively. (B) is the equivalent spatial DoG structure. The bottom row is the same for the MTF-corrected M pathway data (C) and (D).

**Figure 22.** Comparison of MTF/aliasing model (red) (assuming a simple Gaussian function for the low-frequency curve and a 6.3 cpd Nyquist frequency for the pathway (Williams, Artal, Navarro, McMahon, & Brainard, 1996)) to the frequency Gaussian model (blue).

**Figure 23.** (A) Example RGB image. (B) Luminance image based on (A) cropped to remove the reference ball in the lower left-hand corner.

**Figure 24.** (A) Full-image sine wave (wavelength = 21 pixels/0.34°) and 20% Michelson contrast. (B) Contrast versus scale, with the Z axis showing the bin count. (C) Standard deviation vs scale. (D) Mean luminance vs scale.

**Figure 25.** (A) Four sine waves (wavelengths/contrast: 0.74/4.5%, 0.34/14.5%, 0.18/34.5%, 0.11/64.5%) (B) Contrast versus scale, with the z axis showing bin count. (C) Standard deviation vs scale. (D) Mean luminance vs scale.

**Figure 26.** The top row shows the RGB (A) and luminance image (B). The middle row shows the cell-based contrast maps, with (C) showing the raw data and (D) having a small amount of Gaussian filtering applied to reduce the noise. The bottom row shows (E) the raw standard deviation data and (F) the mean luminance data.

**Figure 27.** The top row shows the RGB (A) and luminance image (B). The middle row shows the cell-based contrast maps, with (C) showing the raw data and (D) having a small amount of Gaussian filtering applied to reduce the noise. The bottom row shows (E) the raw standard deviation data and (F) the mean luminance data.

**Figure 28.** (A) Luminance as a function of scale for segments of images categorised as Rural, Foliage, Ground, Sky, Backlit and Urban. (B) RMS variation as a function of scale for the same segments. Note that the x axis scale is patch radius in degrees. (Reproduced from Frazor & Geisler, 2006).

**Figure 29.** Plot of Figure 27(D) as log10(Contrast) vs log10(spatial frequency). The red dashed line is a 1/f slope, and the green dashed line is a $1/f^{\alpha}$ slope where $\alpha = 0.5$.

**Figure 30.** Contrast maps for example images from each category, with each row showing an example RGB image from the group (Sand, Natural, Forest and Urban), the corresponding contrast vs scale plot, and the contrast vs scale plot averaged over 5 images from the group.

**Figure 31.** Plot of Figure 30(K) as log10(1/contrast) vs log10(1/scale) overlaid with the contrast sensitivity functions for the M pathway (black dotted line) and P pathway (red dotted line) at 2Hz temporal modulation frequency.

**Figure 32.** (A) RGB image. (B) Luminance image. (C) P contrast image (0.10 °characteristic scale). (D) M pathway contrast image (0.16° characteristic scale).

**Figure 33.** Luminance, contrast, and contrast response images for five different images (one per row). Column (A) are luminance images. Column (B) are P pathway contrast images. Column (C) are M pathway contrast images. Column (D) are P pathway contrast response images. Column (E) are M pathway contrast response images. The red dashed circles highlight regions of edge enhancement.

**Figure 34.** (A) Application of Sobel filter (pixel based).  (B) Application of Canny filter (pixel based). (C) Cell-based P pathway based on Figure 33 (4 D) with a 50% threshold applied. (D) Pixel-based P pathway (also with 50% thresholds applied).

**Figure 35.** Image of watercolour painting by Abraham Walkowitz.

**Chapter 1 General Introduction**

**1.1 Introduction**

The contrast sensitivity function (CSF) is a powerful tool for analysing the response of the visual system to spatial information. The CSF was first reported in the 1960's (Campbell & Green, 1965; Campbell, Kulikowski, & Levinson, 1966; Westheimer, 1960), and has been extensively used for characterising the spatial sensitivity of the visual system across a range of parameters (De Valois, 1988; Hoekstra, van der Goot, van den Brink, & Bilsen, 1974; Johnston, 1987; Rovamo, Franssila, & Nasanen, 1992; Rovamo et al., 1978). Figure 1 shows examples of the dependence of the CSF on a number of parameters, including luminance, eccentricity and temporal frequency.

*A*
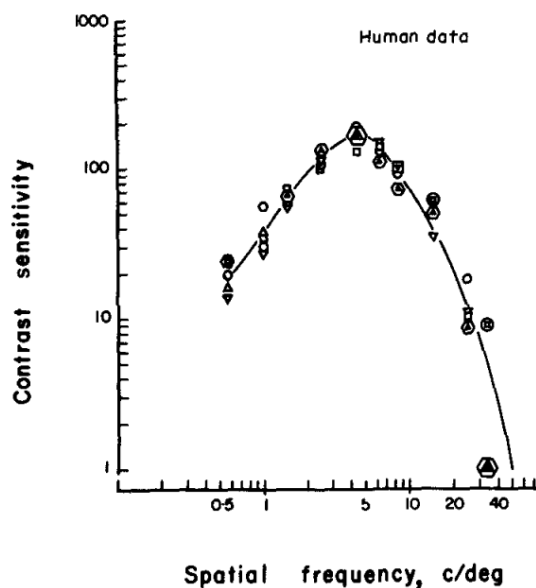


*B*
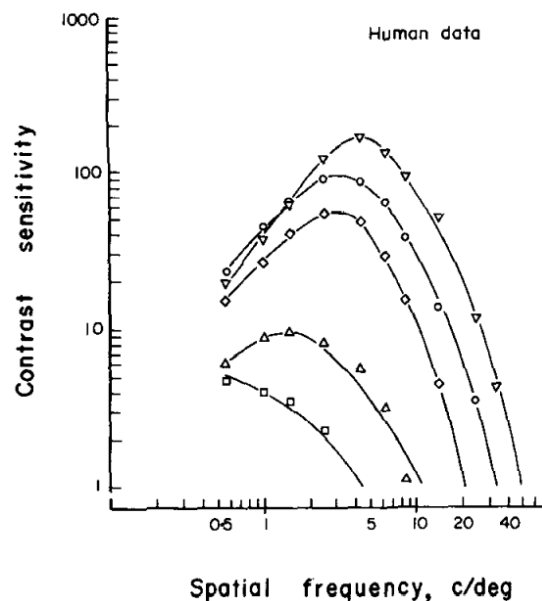


*C*
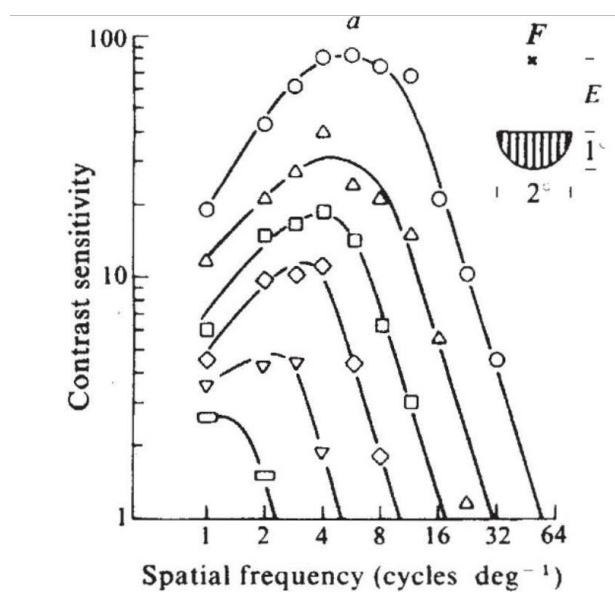


*D*
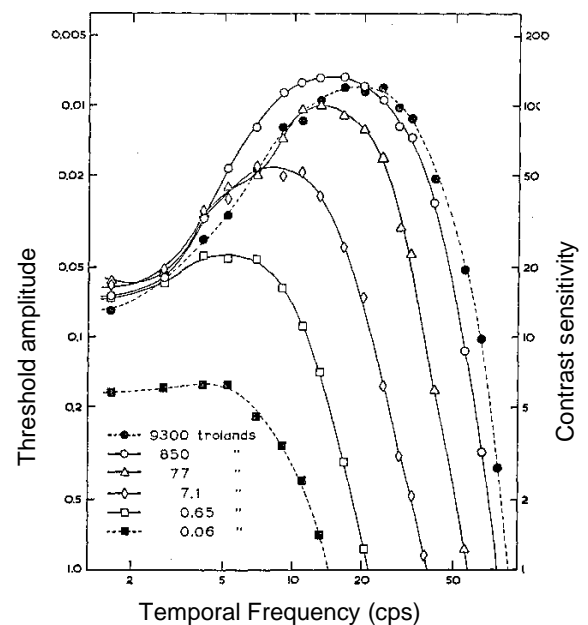
*Figure 1. (A) Simple CSF function for human foveal vision (Reproduced from Devalois et al., 1974). (B) CSF as a function of adaptation for luminance values of 0.0005 - 5 foot-Lamberts in decade steps (Reproduced from Devalois et al., 1974). (C) CSF as a function of eccentricity in inferior visual field at eccentricities of 0°, 1.5°, 4.0°, 7.5°, 14° and 30° (circle to rectangle) (Reproduced from Rovamo et al., 1978). (D) Temporal CSF, as a function of adaptation for luminance values 0.06 to 9300 trolands (Reproduced from Kelly, 1961).*

Figure 1(A) shows an example of CSF, with the contrast sensitivity (the inverse of the contrast threshold) plotted against the spatial frequency of the stimulus (Devalois et al., 1974). The peak of the curve shows the maximum contrast sensitivity, and the shape of the low and high frequency roll-offs provide information about the spatial structure of the system under test. The system can be a population of retinal ganglion cells in a human retina, as shown here, or a single retinal ganglion cell (RGC), for example. Figure 1(B) shows the CSF as a function of adaptation to different luminance levels, which shows how the adaptation of the retina as luminance reduces moves the peak sensitivity to lower spatial frequencies and a lower absolute value (Devalois et al., 1974). Figure 1(C) shows the CSF as function of eccentricity, with the peak moving to lower frequency and lower absolute values as eccentricity increases, but in this case due to an increase in the size of the retinal ganglion cells (Rovamo et al., 1978). Lastly, Figure 1(D) shows the temporal CSF (which is the contrast sensitivity plotted as a function of temporal frequency) as a function of adaptation to different luminance levels, showing how temporal CSF shows how the temporal frequency response of shifts from a high sensitivity/bandpass response at high luminance to a low sensitivity/lowpass response at low luminance. As can be seen, the CSF can provide insight into range of characteristics of the early visual system.

The physiological basis of the CSF began to be elucidated with the identification of the differential contrast gain characteristics of the two primary cell types in the Lateral Geniculate Nucleus (LGN), the parvocellular (P) and magnocellular neurons (M) (Kaplan & Shapley, 1982). The M cell contrast gain response is strongly non-linear, with a high gain at low contrast, approaching saturation at high contrast, and with a bandpass spatial sensitivity, peaking at lower spatial frequencies. The temporal response is predominantly phasic. In contrast, the P cell response has a lower contrast gain but remains linear up to high contrast values with no saturation, and a band-pass spatial frequency response extending to higher frequencies. The P cell temporal response is predominantly tonic. Subsequent experiments showed that these characteristics are mirrored in the response characteristics of M and P retinal ganglion cells (Kaplan & Shapley, 1986). Complementary lesion studies suggest that the P pathway is predominantly involved with transmitting high spatial acuity luminance and chromatic information, and the M pathway for low contrast, high temporal frequency information (Edwards, Goodhew, & Badcock, 2021). The demonstration of these differential physiological responses at the cellular level led to the hypothesis that the measured psychophysical achromatic contrast sensitivity function of the primate visual system could be explained by combining the P and M retinal ganglion cell responses (Kaplan et al., 1990; J.J. Kulikowski, 1987) (see Figure 2).
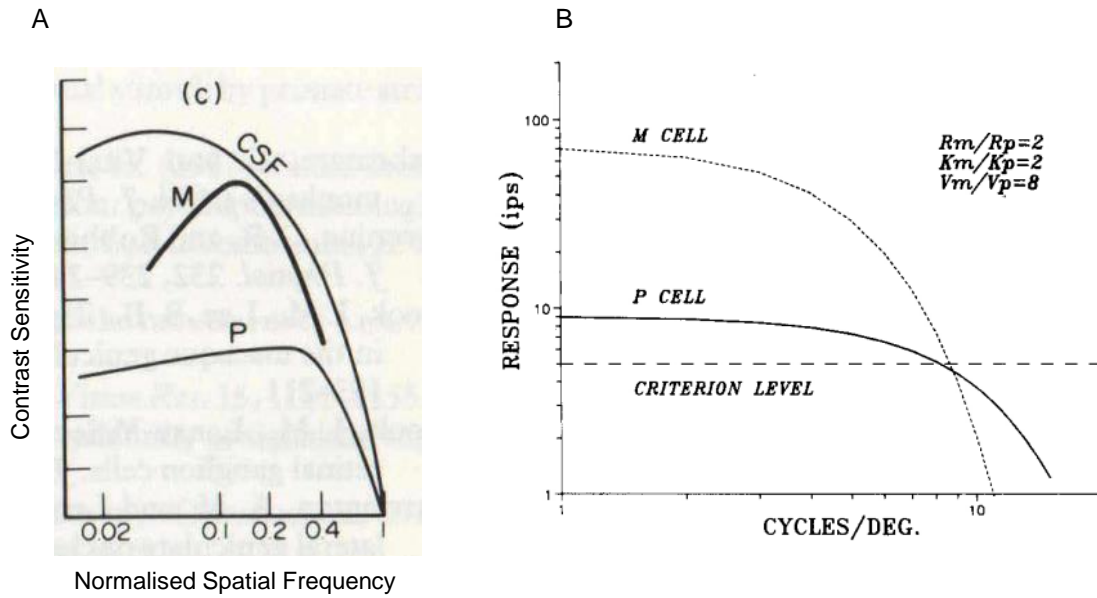
A

B

Contrast Sensitivity

Normalised Spatial Frequency

*Figure 2. (A) Model of the achromatic contrast sensitivity function from Kulikowski (Reproduced from J.J. Kulikowski, 1987). (B) Model of combined response of an array of P and M RGCs from Kaplan (Reproduced from Kaplan et al., 1990).*

Figures 2(A) and 2(B) illustrate the models proposed by Kulikowski and Kaplan, showing the contributions of the high sensitivity/low spatial frequency response of the M RGC and the lower sensitivity/high spatial frequency response of the P RGC. The primary difference is that Kulikowski's figure implies that the combined response is the sum of the two pathway sensitivities, whereas Kaplan's model implies that the combined response is that the more sensitive of the two pathways dominates (i.e., a "winner-takes-all" model). If the latter is the case, then in principle it should be possible to discriminate between the two pathways by detecting the kink in the combined signal. However, it can be seen that the CSFs shown in Figure 1 do not exhibit the kink.

Numerous studies have attempted to discriminate the role of the M and P pathways in the contrast sensitivity function psychophysically, using simple spatially and temporally varying grating stimuli (Evans, Drasdo, & Richards, 1994; J. J. Kulikowski & Tolhurst, 1973; Legge, 1978; Livingstone & Hubel, 1987; F. Martin & Lovegrove, 1984). In principle, the use of these simple stimuli would allow the measured psychophysical characteristics to be related to the spatial dimensions of the underlying physiological structure of the RGCs. However, despite significant effort, reliable differentiation has been elusive and as a result there continues to be debate as to whether the spatial and temporal differences between M and P pathway activity are sufficient for them to be discriminated psychophysically with grating stimuli (Edwards, Goodhew, & Badcock; Edwards et al., 2021; Skottun, 2015).

This has led to a search for alternate but more indirect methods of discrimination between M and P pathway-determined psychophysical responses. These techniques included the development of

temporally varying stimuli that rely on differentially stimulating the saturating, phasic M pathway to discriminate between M and P pathways.

A good example of such techniques is the Steady Pedestal /Pulsed Pedestal (SP/PP) paradigm (Pokorny & Smith, 1997) which uses common stimuli (squares on background) but differential pre-and post-adaptation to discriminate between the M and P pathways. The technique was subsequently developed to include a Pedestal $\Delta$ Pedestal (P$\Delta$P) stimulus (Pokorny, 2011). This combination of paradigms enabled the P pathway contrast gain, the M pathway sensitivity and contrast gain to be inferred. The data also supported the "winner-takes-all" model (Pokorny, 2011). The technique was further developed to include a spatial frequency component in the SP/PP temporally-varying stimuli, which enabled partial characterisation of spatial frequency processing in the of M and P pathways for short-duration stimuli (26ms) (Leonova, Pokorny, & Smith, 2003)  However, neither paradigm allows independent control of the temporal as well as the spatial frequency of the stimuli, preventing the full characterisation of the M and P responses in terms of both spatial and temporal frequency.

Experiments in which response time is the primary measure have demonstrated a characteristic behaviour which has been interpreted as differentiating between the P and M channels (Tolhurst, 1975). Typically, response time measurements show a linear dependence on contrast, but under certain conditions there is a transition in slope sensitivity giving a bi-linear function (Murray & Plainis, 2003; Plainis & Murray, 2005). The low and high contrast segments of this bi-linear function was attributed to the M and P channels respectively, with an overall conclusion that the results supported the contention that the M channel predominantly determines the Contrast Sensitivity Function. It was also noted that the overall system response is to the most sensitive of the two channels, rather than summing the two channel responses (Murray & Plainis, 2003).

Investigation of contrast-dependent Visually Evoked Potentials (VEPs) has elicited differential responses for low and high contrast spatial stimuli, which have been interpreted as representing the M and P channels (Lalor & Foxe, 2009). Temporal frequency differentiation was not investigated in the study, with the differentiation being determined solely by contrast level

Partly as a result of this reliance on indirect measurements, the debate about the roles of the M and P pathways continues; recent reviews have highlighted the continuing lack of clarity about the relative contribution of the two channels to achromatic and chromatic perception (Lee, 2019) and the challenges of constructing psychophysical stimuli in order to achieve optimal differentiation (Edwards et al., 2021).

This dissertation describes a new methodology to psychophysically identify distinct M and P pathway responses, together with a simple explanatory model that links the spatial frequency responses to the spatial dimensions of the RGCs. In so doing I explore whether it is possible to discriminate between the P and M pathways psychophysically in terms of both spatial and temporal frequency responses,

and to determine their respective contributions. I also present a new image analysis technique to determine local contrast variations across luminance images and then model the corresponding contrast response images.

The starting point is a short introduction to the basic functionality of the human eye, identifying the main features that will be relevant for understanding and modelling the peripheral contrast responses, and to design the discrimination experiment.

## 1.2 Structure of the Human Eye

The structure of the human eye is shown schematically in Figure 3.
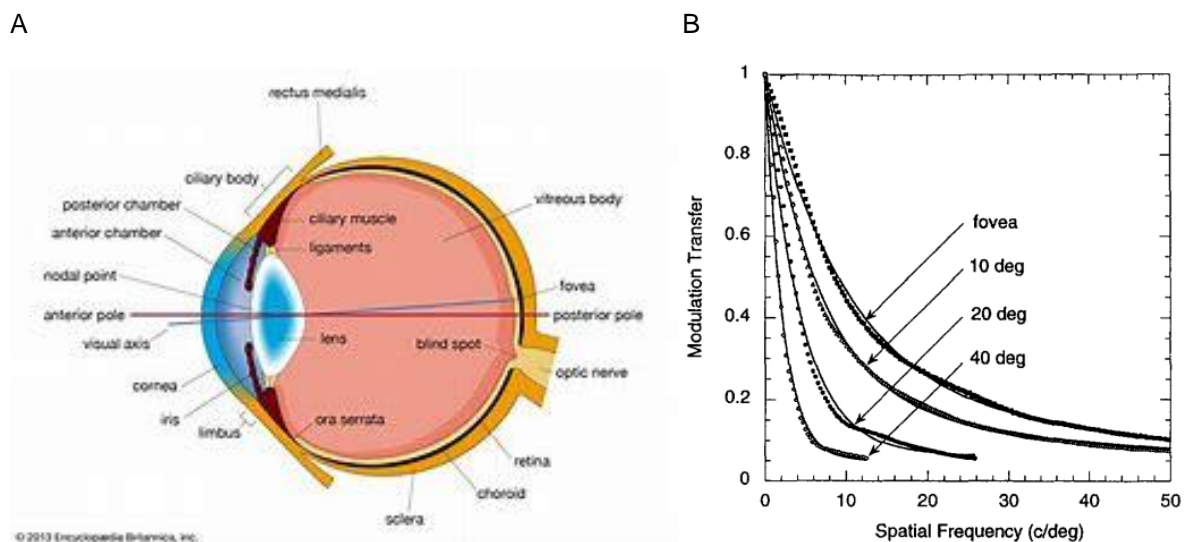
A                                                                    B



*Figure 3. (A) Schematic of the human eye (Reproduced from Sekuler & Blake, 2006).(B) Modulation transfer function (MTF) as a function of eccentricity for horizontal meridian in temporal, determined at circle of east confusion (Reproduced from Navarro et al., 1993).*

Light from the external world is focused onto the retina by the complex lens structure formed by cornea and lens. Control of the focal length is by changing the tension in the cilium muscles around the lens, which in a young adult eye can vary the focus from infinity down to about 0.5m. The amount of light falling on the retina is modulated by the iris, which can change in diameter from 2mm to 8 mm in a young adult (Sekuler & Blake, 2006), varying the light transmitted by a factor of 16.

The optical performance of the lens is equivalent to a wide-angle lens (Navarro et al., 1993), with an adequate but non-diffraction limited resolution at the fovea but with a relatively constant modulation transfer function (MTF) in the periphery, as shown in Figure 3(B) (Williams et al., 1996). As such a reasonable image is formed approximately +-90 degrees either side of the visual axis. In short, the lens is an effective general-purpose lens well-adapted to the requirements of human vision where useful information in the periphery needs to be accessed.

For studies of peripheral retinal performance where the stimuli are being imaged off-axis, the spatial frequency response declines significantly from 0-20 degrees (Figure 1(A)). Therefore, interpretation of psychophysical spatial frequency responses in relation to the underlying physiology of the retina in this regime will need to take account of the MTF profile. This is the case for the experiment described in Chapter 2. However, studies of the perceived peripheral response (such as the visualisation model I present in Chapter 3) do not require the MTF compensation.

### 1.3 Anatomy of the Human Retina

The basic structure of the retina is shown in Figure 4.
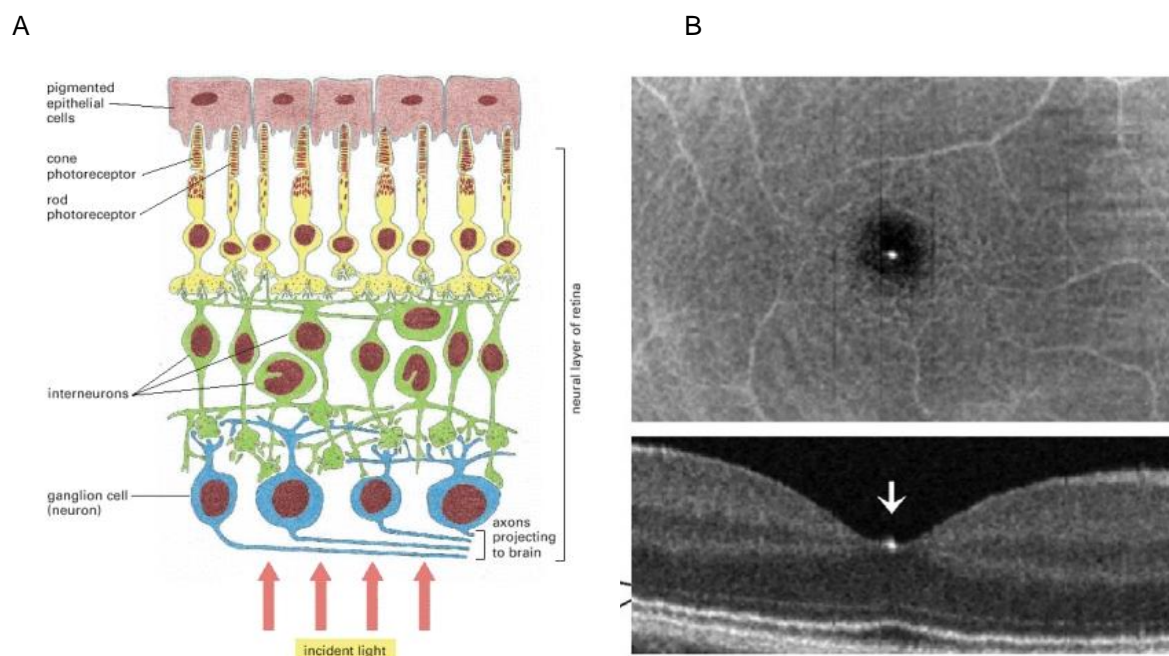
A                                                                B



*Figure 4. (A) Schematic of main neurons in the primate retina (Reproduced from Sekuler & Blake, 2006). (B) Images of horizontal (top) and vertical (bottom) cross-sections of human fovea (Reproduced from Bringmann et al., 2018).*

The primary cell types in retina are (Sekuler & Blake, 2006):

**Photoreceptors** – conversion of the incoming photons into electrical impulses; two primary types namely cones and rods (see Section 1.3.1).

**Horizontal cells** – laterally connecting cells that assist in the determining the spatial extent of the visual response

**Bipolar cells** – intermediate cells which contribute to the ON and OFF functionality

**Amacrine cells** – thought to mediate the temporal responses of the retinal ganglion cells

**Ganglion cells** – gather inputs from the rods and cones (via the amacrine, horizontal and bipolar cells) and transmit (as a bundle called the optic nerve) to the visual cortex (V1, V2 etc) via the Lateral Geniculate Nucleus.

The primary focus of this dissertation will be on the characteristics of the photoreceptors and RGCs.

The photoreceptors are on the rear surface of the retina, such that the incoming light must pass through the semi-transparent upper layers (with the bipolar and amacrine cells) before the light reaches the photoreceptors. This leads to some scattering of the light, which limits the spatial acuity (the ability to resolve high spatial frequencies). The eye has evolved to minimise this problem by having an area on the retina (aligned with the optical axis of the lens) where the bipolar, amacrine and ganglion cells are displaced from the central region (the fovea), such that the incoming light falls directly onto the photoreceptors (Figure 4B). Therefore, in this region the density of photoreceptors is high (predominantly cones), with little scatter from other cells. The fovea therefore provides the highest spatial resolution.

### 1.3.1    Types of Photoreceptors

The rods have a very high sensitivity, able to detect only a few photons when fully dark adapted (Burns & Pugh, 2014). However, the rod response saturates at moderate luminance. In contrast, the cones are less sensitive, but do not saturate, such that they can differentially respond up to high luminance levels. There are three types of cones (L, M and S) with differing chromatic response curves which support the perception of colour (chrominance or chromatic vision), as well as achromatic vision. The chromatic sensitivity curves of the cones are shown in Figure 5:
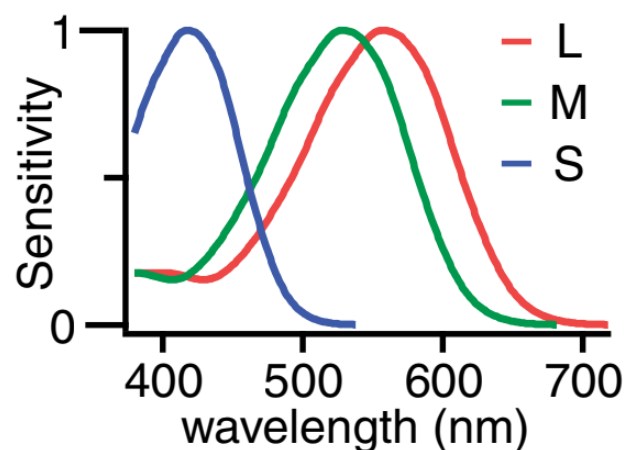


*Figure 5. Relative sensitivity of the L, M and S cones as a function of wavelength (Reproduced from Solomon & Lennie, 2007).*

The rods have a purely achromatic response, whereas the outputs of the cones can be summed in different ways to provide both achromatic (luminance) and chrominance signals:

$$\text{Luminance} = L + M \tag{1a}$$

$$\text{Red} - \text{green (R-G) chrominance} = L - M \tag{1b}$$

$$\text{Blue (B) chrominance} = S - (L+ M) \tag{1c}$$

The spatial distribution of the rods and cones in the retina is shown in Figure 6:
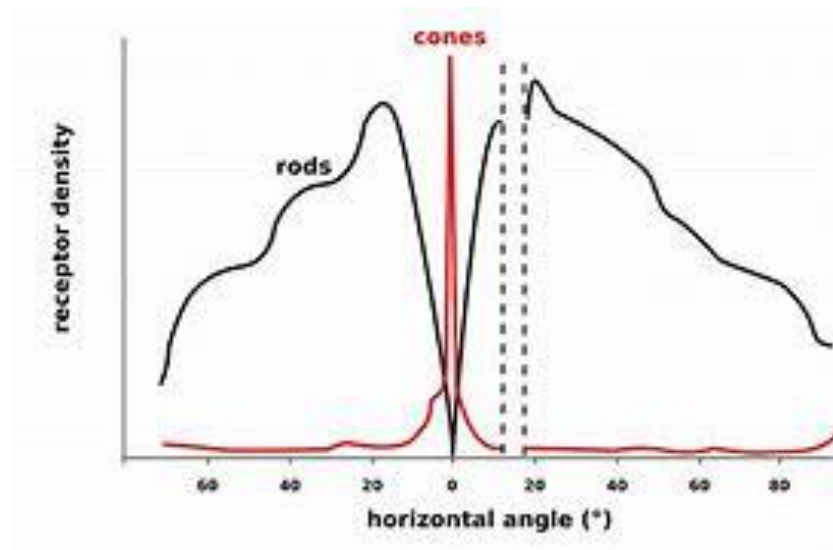


*Figure 6. Distribution of the cones and rods as a function of eccentricity (along the horizontal meridian) (Reproduced from Sekuler & Blake, 2006).*

The cone density is highest in the central (foveal) region, declining rapidly with eccentricity. The rod density is effectively zero at the fovea, peaks at around 20° eccentricity, and then declining slowly with eccentricity. There are approximately 100 million rods and 5 million cones in each retina. The relative contribution of the two receptor types to achromatic vision in the periphery depends on their sensitivity and saturation characteristics, and so varies with luminance levels.

### 1.3.1.1 Luminance Sensitivity and Adaptation

The photoreceptors jointly have a luminance dynamic range of about $10^{12}$, ranging from low-level starlight at $10^{-6}$cd/m$^2$ to bright sunlight at $10^6$ cd/m$^2$ as shown in Figure 7:
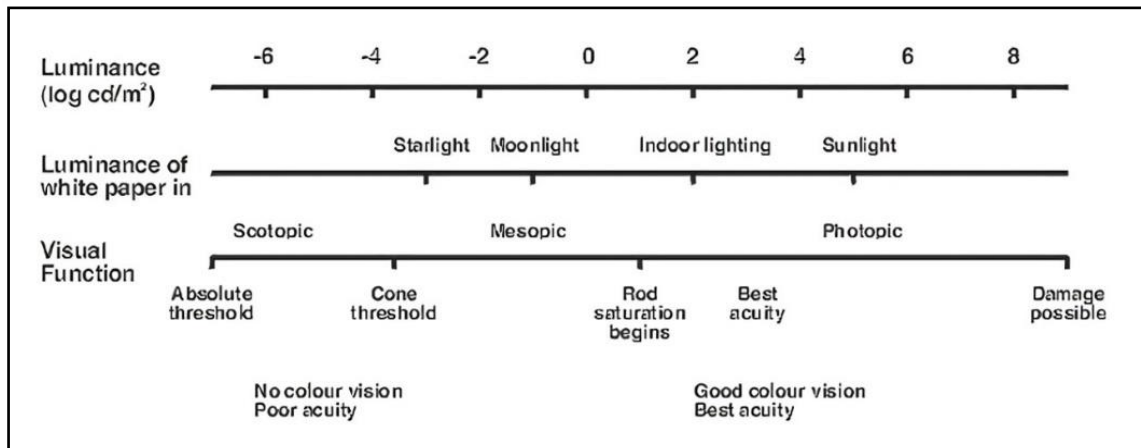
*Figure 7. Luminance sensitivity of the human visual system (Reproduced from D. Cao, 2013).*

At high luminance levels ($10^1$-$10^8$ cd/m$^2$) vision is mediated predominantly by cones as the rods begin to saturate at around 10 cd/m$^2$. This range is referred to as photopic vision. At very low luminance levels, vision is predominantly mediated by rods, and is referred to as scotopic vision. The intermediate range where both rods and cones are functional is mesopic vision.

At any point within the total dynamic range of $10^{12}$, the active dynamic range is approximately $10^2$, determined by the contrast gain characteristics of the RGCs (see Section 1.3.2.1). As such, several adaptation mechanisms are present that move the active dynamic range window across the full luminance range. The three primary adaptation mechanisms are:

Physical adaptation by aperturing by the iris of the amount of light reaching the retina. The diameter of the iris can typically change from 2mm to 8mm, giving a ratio (in terms of area) of ~$1.6$x$10^1$.

Physiological adaptation of photosensitivity within the chemical pathways of the photoreceptors and subordinate cells (Burns & Pugh, 2014)

Channel adaptation (switching) between the rods (high luminance sensitivity, saturating) and cones (lower luminance sensitivity, non-saturating)

In the experiments described in this dissertation (Chapter 2), the mean luminance of the display was $1.05$ x $10^2$ cd/m$^2$, which is in the photopic range. At this luminance level, the rods are approaching saturation such that the dominant response is that of the cones. In addition, the stimuli used were achromatic. As such, that visual response being investigated was achromatic, coned-based, photopic vision.

### 1.3.2    Retinal Ganglion Cells

There are at least 20 types of retinal ganglion cell (RGC) (Kaplan, 2013), of which the three main types are the parvocellular (P, midget), magnocellular (M, parasol) and the koniocellular (K). The total number of RGCs is approximately 1million per eye, with 80% being P RGCs, 10% being M and the balance being K and other types. The parvocellular and magnocellular RGCs are so named because they terminate in the respectively named layers in the Lateral Geniculate Nucleus (LGN). The P and M RGCs receive inputs from both the L and M cones, whereas the K RGCs only receive inputs from the S cones. Achromatic stimuli therefore predominantly stimulate the P and M pathways and not the K pathway.

The retinal ganglion cells (RGCs) are the sole link between the retina and the visual cortex, with the axons of these neurons forming the optic nerve linking to the lateral geniculate nucleus (LGN) (Solomon & Lennie, 2007). Therefore, it is the characteristics of RGCs that determines what visual information is passed from the retina to the higher visual cortex. The primary differentiating characteristics of the M and P RGCs are:

    Contrast sensitivity
    Temporal frequency response
    Spatial frequency response
    Spatial resolution
    Chromatic sensitivity

These are reviewed briefly in the following sections.

### 1.3.2.1 Contrast Sensitivity of RGCs

Both M and P RGCs are primarily sensitive to contrast as opposed to luminance, with the two types having very different contrast sensitivities as shown in Figure 6 (Kaplan & Shapley, 1986).
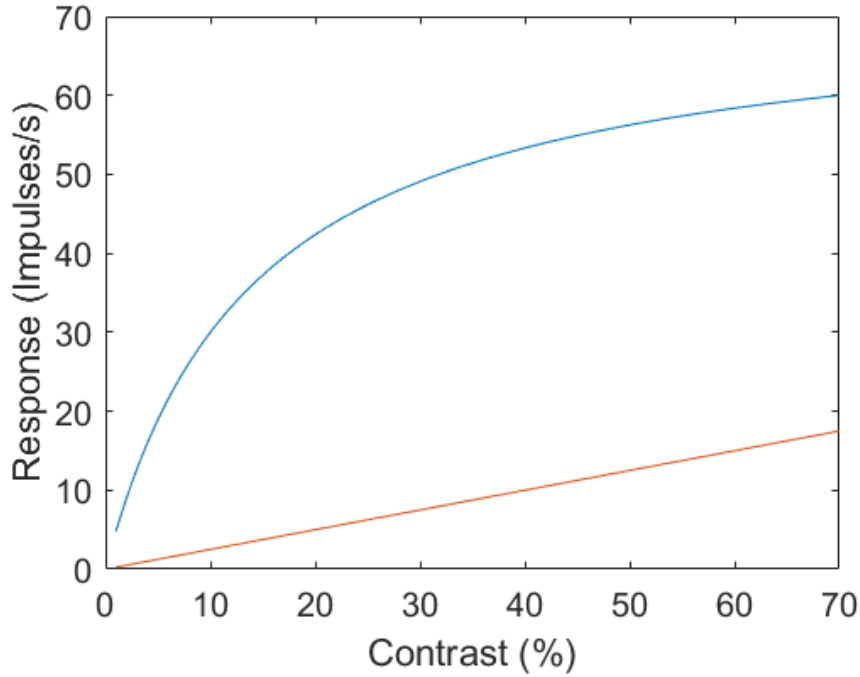
*Figure 8. Contrast gain functions of the magnocellular and parvocellular retinal ganglion cells (based on data from (Kaplan & Shapley, 1986))*

The contrast gain characteristic of the M RGCs is described by the Michelis-Menten function:

(2)

$$R(C) = \frac{R_{max}}{\left(1+\frac{C_{50}}{C}\right)}$$

Where R(C) is the response (in impulses/sec), C is the contrast, Rmax is the maximum response and $C_{50}$ is the contrast at 50% of the maximum response. The M RGCs have a non-linear response, with high sensitivity at low contrast and approaching saturation at high contrast. The P RGCs have a linear response that does not saturate, with a lower peak sensitivity at 100% contrast.  This differential contrast sensitivity is key to understanding the behaviour of the two pathways, as will be seen in Chapter 2.

Given that the threshold value of the RGC is typically 2-5 i.p.s (Pokorny & Smith, 1997), the dynamic range is approximately $10^2$. As such, the RGCs are a significant bottleneck in transmitting information from the retina to the visual cortex. In addition, given the very different slope sensitivities of the M and P contrast gain functions, the equivalent contrast thresholds corresponding to the impulse rate threshold are significantly different, around 1% for the M pathway and 10% for the P pathway. Therefore, the M pathway has a significantly higher contrast sensitivity than the P pathway. However, given the higher density of P RGCs (approximately eight times that of the M RGCs averaged across

the retina (Kaplan, 2013)), summing of the P RGC outputs may partially compensate for their lower intrinsic contrast sensitivity in contrast sensitivity measurements.

### 1.3.2.2 Temporal Response

The M RGC has a transient temporal response to an edge stimulus, compared to the sustained temporal response of the P RGC (Kaplan, 2013). In addition, the latency of the M pathway is lower, and the axon conduction velocity is higher (Edwards et al., 2021). As such, varying the temporal frequency of spatial stimuli should contribute to discrimination between the two pathways.

### 1.3.2.3 Spatial Structure and Spatial Frequency Response of RGCs

The spatial structure of the RGCs have been shown to be well-described by a Difference of Gaussian model (DoG), where the output of a narrow centre Gaussian function is opposed to the output of a broader, lower-sensitivity surround Gaussian (Enroth-Cugell & Robson, 1966; Rodieck, 1965). The structure is shown schematically in Figure 9.
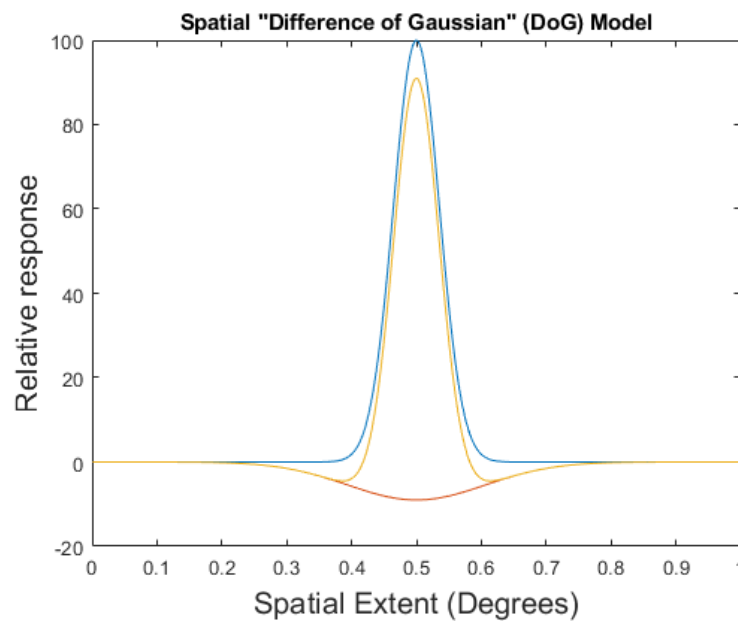


*Figure 9. (A) Spatial centre/surround structure for "Difference of Gaussian" RGC sensitivity model, with the blue, red and yellow lines being the centre, surround and DoG responses respectively.*

The centre-surround opponency gives rise to both the opponent achromatic spatial frequency response for both M and P pathways and the opponent red-green chromatic response for the P pathway (when the centre is primarily fed by L cones and the surround by M cones (equation1(b)), or vice versa). However, for this dissertation I am only concerned with the achromatic spatial frequency response.

The spatial frequency response is the Fourier transform of the spatial structure, so the spatial and frequency responses of the DoG filter are defined as (Enroth-Cugell & Robson, 1966):

(3a)

$$W(r) = k_c \exp\left(-\left(\frac{r}{r_c}\right)^2\right) - k_s \exp\left(-\left(\frac{r}{r_s}\right)^2\right)$$

(3b)

$$S(f) = k_c \pi r_c^2 \exp\left(-(\pi r_c f)^2\right) - k_s \pi r_s^2 \exp\left(-(\pi r_s f)^2\right)$$

Where $r$ is the spatial dimension, $f$ is the spatial frequency, $W(r)$ and $S(f)$ are the spatial and frequency DoG functions respectively, $k_c$ and $k_s$ are the peak sensitivities of the spatial centre and surround functions (dependent on the contrast gain characteristics of each pathway), and $r_c$ and $r_s$ define the radii of the spatial centre and surround functions.

The spatial frequency response from equation 3b is plotted in Figure 10, which shows the bandpass structure of the DoG response for balanced centre and surround responses, changing to a low pass structure as the centre dominates.
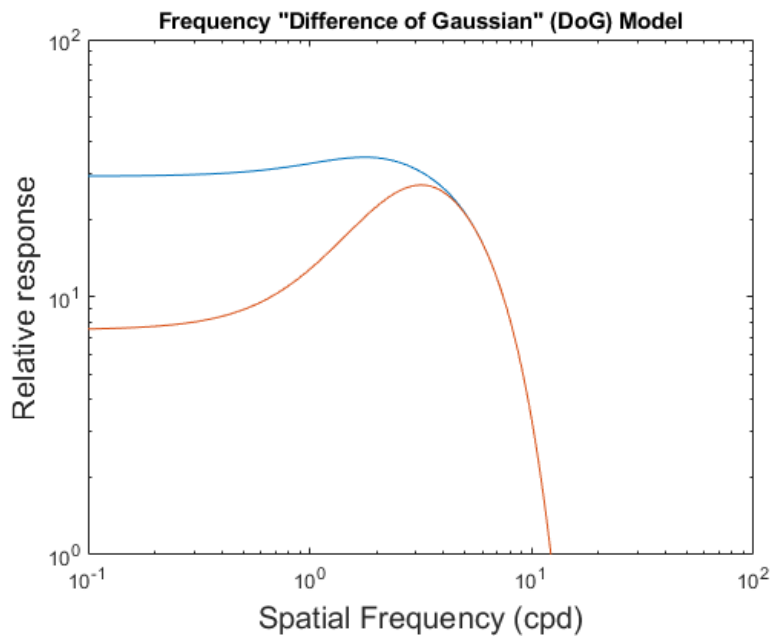


*Figure 10. Frequency response as a function of spatial frequency for different centre-surround structures. The orange line corresponds to a centre/surround weighting of 10:1, showing a strong bandpass response. The blue line corresponds to a centre/surround weighting of 100:1, showing a low-pass response.*

The bandpass response (orange line) in Figure 10 corresponds to the spatial DoG structure in Figure 7. It can be seen that the response is similar to that of Figure 1(A). As the relative weighting of centre to surround increases, the response becomes more band pass. Note that the high-frequency cut-off

behaviour is largely independent of the surround response i.e., it is determined primarily by the centre response.

The link between spatial structure (Figure 9) and spatial frequency response (Figure 10) via the DoG model is key to differentiating between the M and P RGCs. The original labels for the M and P RGCs (parasol and midget) arose from their different relative sizes. Figure 11 shows an example of dendritic field diameter data for human RGCs as a function of eccentricity (Dacey & Petersen, 1992).
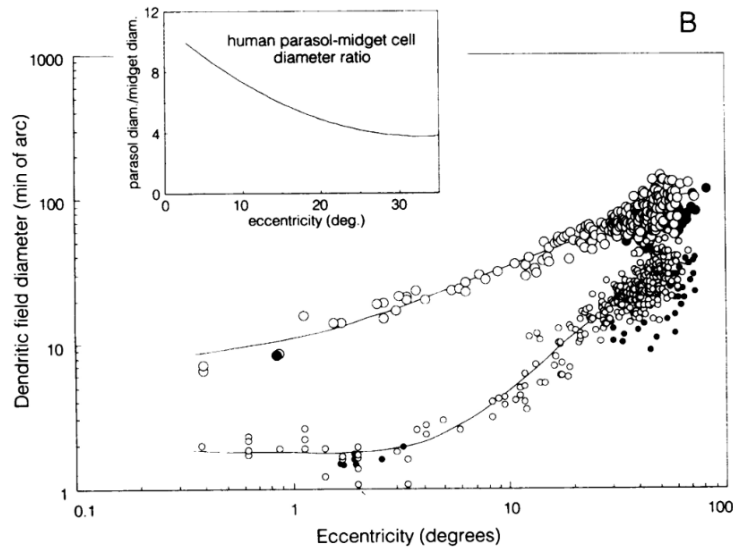


*Figure 11. Dendritic field diameters as a function of eccentricity for midget (P, parvocellular) signified by the small circles and parasol (M, magnocellular) retinal ganglion cells signified by the large circles. The filled circles are for the nasal quadrant and the unfilled circles for the other quadrants. (Reproduced from Figure 2(b) from (Dacey & Petersen, 1992))*

The fitted P (midget) RGC dendritic field diameter is 5 times smaller than the M RGCs at 20° eccentricity (albeit with a wide range of values). As such, the DoG spatial frequency response of the P RGC would be 5 times lower than the equivalent M RGC, for a given eccentricity.

For in vivo experiments (including psychophysics), the dendritic field diameter cannot be measured directly. Instead, the receptive field (RF) is determined by a spatially varying stimulus, such as shown in Figure 12 (Croner & Kaplan, 1995).,
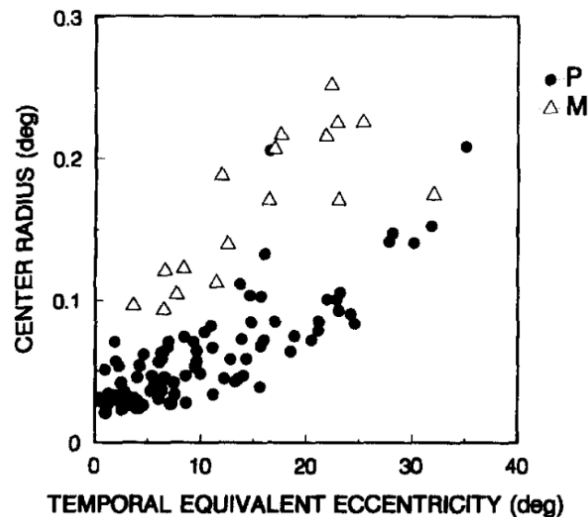
*Figure 12. Centre radius of receptive fields of primate parvocellular and magnocellular retinal ganglion cells (Reproduced from Croner & Kaplan, 1995)*

In contrast to the dendritic field data, the ratio of P and M RF size is only a factor of 2 at 20° eccentricity. As such, the interpretation of the relationship between dendritic field diameter and RF size requires caution.

Overall, the DoG model is a useful tool for characterising RGC RFs. If the spatial frequency response can be determined, then the spatial characteristics of the RGC RFs that we are sampling with our stimuli can be inferred. This is the primary tool that I use in Chapter 2 for characterising the M and P pathways in peripheral vision.

However, the analysis so far has related to the structure of the individual RGCs. Another key consideration is the geometry of the arrays of the RGCs, which determines the visual acuity.

### 1.4 Visual Acuity

In practice, the measured visual acuity depends on the task that is being undertaken. If the task is to simply detect the presence or absence of a stimulus (detection), then the spatial frequency response is that defined by the DoG function arising from the physical dimensions of the RGC (in the periphery) or the cones (in the fovea). However, the detection task has limited relevance for interacting with the outside world as it simply indicates the presence or absence of a stimulus, with no indication of size, direction, movement, or orientation. A more relevant task is resolution, which is both detecting the presence of a stimulus plus determining something about its form, such as the orientation of gratings, or the position of the gap in a Landholt C. In the resolution task, the limiting physical factor is not the physical dimensions of individual RGCs as it is for detection but is instead the spacing between adjacent elements in an array of photoreceptors or RGCs.

26

The determination of the resolution spatial acuity is governed by sampling theory, originally described by Shannon (Shannon, 1949). In this theory, the highest unambiguous spatial frequency that can be measured is given by the Nyquist frequency $f_N$ where:

<div align="right">(4)</div>

$$f_N = {}^1\!/_{2d}$$

where d is the spacing in the array. For spatial frequencies below the Nyquist frequency, the sampled signal can be accurately recovered from the input signal. For frequencies higher than $f_N$, the input signal is aliased (or reflected back below $f_N$), such that the input signal can no longer be unambiguously recovered. Therefore, in order to understand the variation of resolution with eccentricity, we need to understand what the limiting spacings are of the various sampling arrays in the retina.

### 1.4.1    Sampling Arrays in the Retina

In principle, the sampling spacing of the retina is that of the RGC array, given that the RGCs are the sole link between the retina and the visual cortex (Sekuler & Blake, 2006). However, due to the displacement of the RGCs (and the other retinal neurones around the fovea) described in Section 1.3, the effective sampling spacing at any point in the retina is determined by either the cone spacing or the RGC spacing, whichever is the smaller.

The density of cones as a function of eccentricity is shown in Figure 13(A) (Curcio & Allen, 1990; Watson, 2014) for the four meridians, with the RGC distribution shown in Figure 13(B).

*A*
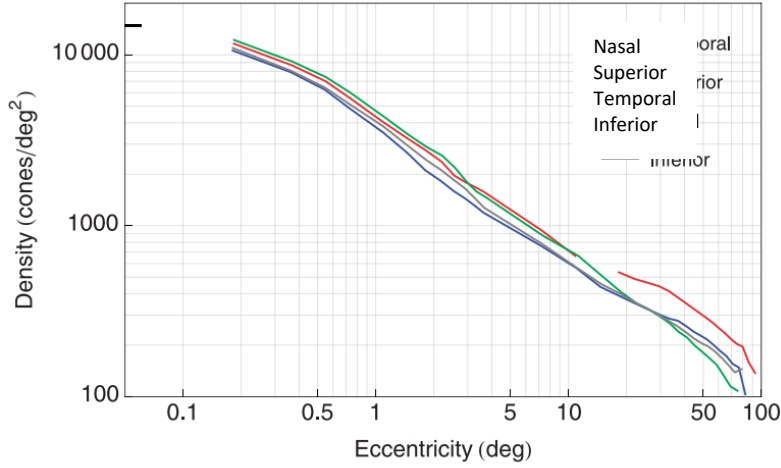


*B*
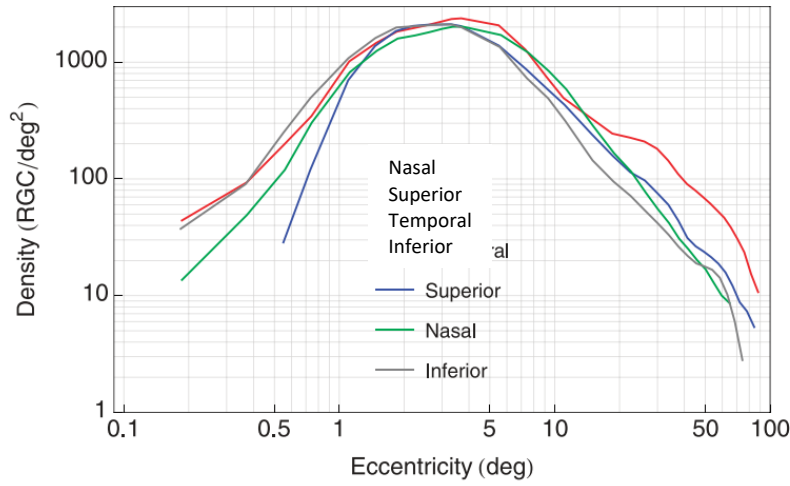


*Figure 13. (A) Cone density as a function of eccentricity for the four meridians (Reproduced fromWatson, 2014, after Curcio et al, 1990)). (B) P RGC density as a function of eccentricity for the four meridians (Reproduced from Watson, 2014, after Curcio et al, 1990).*

The density of cones (Figure 13(A)) is highest at the fovea, declining rapidly with eccentricity. The density of P RGCs (Figure 13(B)) is essentially zero at the fovea (due to displacement of the RGCs at the fovea as discussed in Section 1.3), with a peak at 5°, and then declining with eccentricity. Note that the blind spot where the axons of the RGCs pass through the retina to form the optic nerve can be observed in the nasal meridian for both the cone and RGC data.

The sampling spacing (d), assuming hexagonal close packing, is given by (Watson, 2014):

(5)

$$d = \sqrt{\frac{2}{D\sqrt{3}}}$$

where D is the density. Using the density data from Figure 13 and Equation 5, Watson derived the equivalent spacing of the P RGCs spacing for each meridian, as shown in Figure 14 (Watson, 2014).
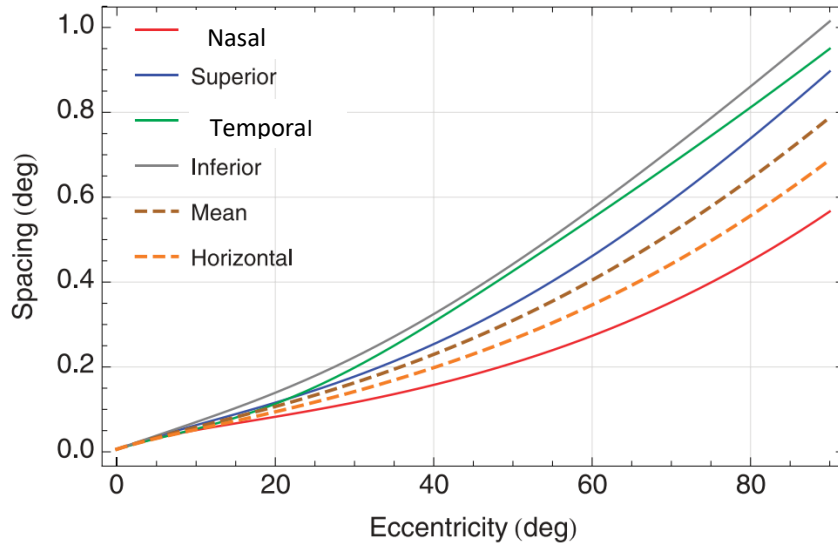


*Figure 14. Array spacing as a function of eccentricity for the four meridians, including the overall mean and the mean for the horizontal meridian (Reproduced from Watson, 2014).*

The nasal meridian array spacing increases approximately linearly up to about 50° eccentricity. For the mean of all the meridians, the array spacing can be approximated by the following linear equation (Watson, 2014):

(6)

$$A = A_0 + S \times \varepsilon$$

Where $A_0$ is the value at the fovea, $S$ is the characteristic scale factor and $\varepsilon$ is the eccentricity. For the data shown, the scale factor is $S = 0.0075$ and $A_0 = 0.0088°$.

A reasonable assumption is that the array spacing in the retina would approximately match the receptive field diameter of the RGCs, to maximise the efficiency of photon capture (i.e., no gaps) whilst minimising crosstalk (minimising overlaps). Comparison of the RGC spacing with dendritic field diameter data confirms that this is a reasonable assumption, as shown in Figure 15.
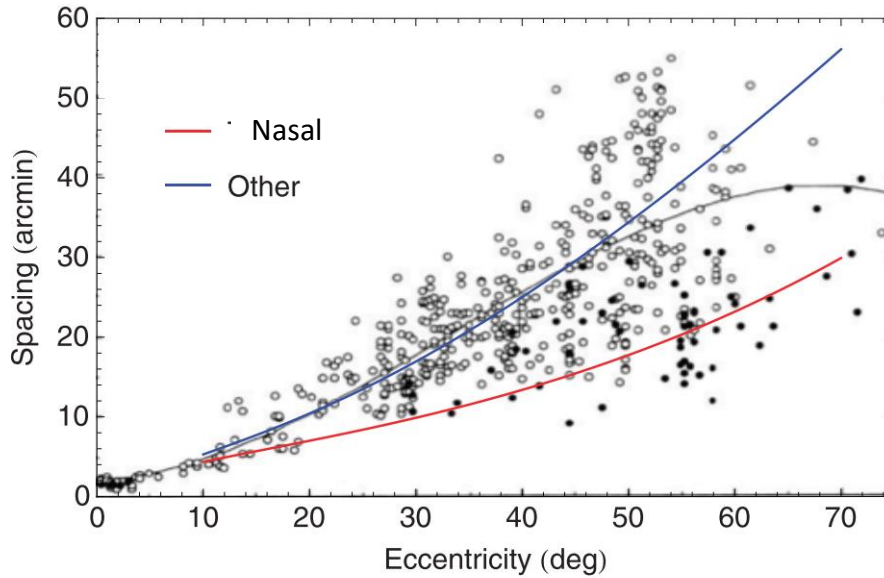
*Figure 15. Comparison of dendritic field diameter vs eccentricity to the P RGC spacing. The black and white circles are dendritic field sizes for individual nasal and non-nasal meridians respectively and the red and blue lines are the RGC array spacing fits for nasal and non-nasal meridians, respectively (Reproduced from Watson, 2014, with dendritic field size data after Dacey, 1993).*

Figure 15 shows reasonable agreement between calculated array spacing and measured dendritic field size for the P RGCs, albeit with a large spread on the field diameter data (Watson, 2014). A key point to note is the significant difference in receptive field size (and array spacing) of the nasal meridian relative to the other meridians. Therefore, to maximise the sensitivity to cut-off frequency, the stimuli should be viewed monocularly to isolate a single meridian (which is the nasal meridian for the experiment described in Chapter 2).

The observation that receptive field size increases approximately linearly with eccentricity is a general property of the visual system. For example, Figure 16 shows population receptive field (pRF) size versus eccentricity determined using fMRI for different layers of the visual cortex (Wandell & Winawer, 2015).
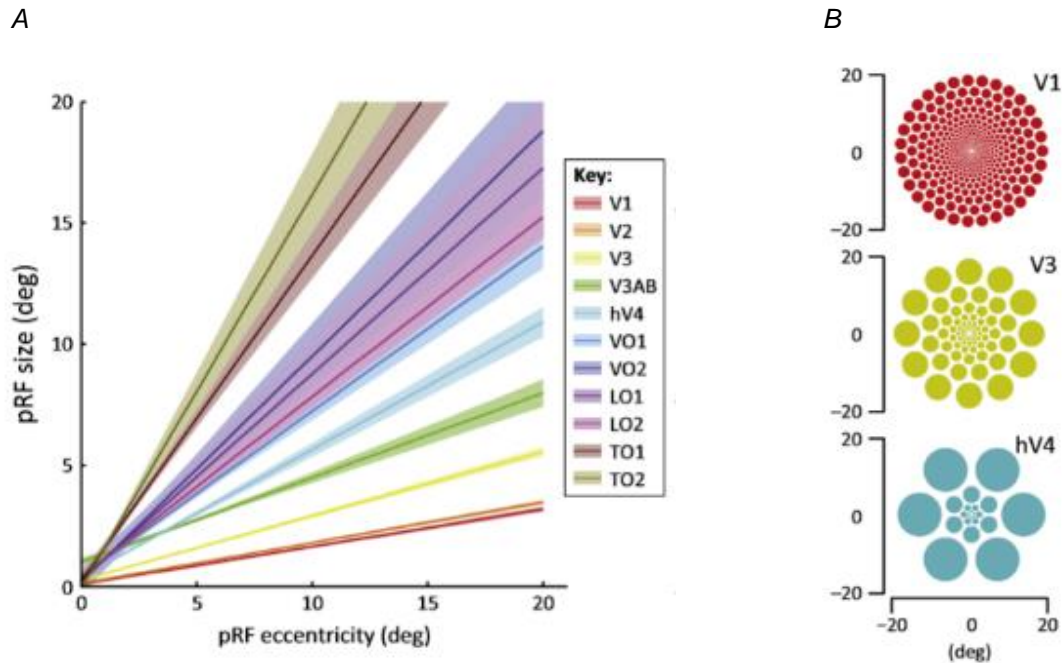
*Figure 16 (A) Population receptive field (pRF) as a function of eccentricity for the primary areas in the visual cortex determined using fMRI (V1-V3AB are in the primary visual cortex and V01-2, LO1-2 and TO1-2 are the ventral occipital, lateral occipital and temporal occipital regions (Reproduced from Wandell & Winawer, 2015). (B) Visualisation of the variation of the RF diameter as a function of eccentricity for V1, V2 and hV4 (Reproduced from Wandell and Winawer, 2015).*

The scale factors increase from approximately 0.15 for V1 to 1.7 for T02, and the pRF (for a given eccentricity) increases for each layer, referred to as spatial pooling.  The importance of spatial pooling is that it has been hypothesised that if each layer of the visual cortex has a defined scale factor, then if the scale factor for a given process can be determined then that process can be localised to a specific layer in the visual cortex. This localisation technique been reported using metameric images to determine characteristic scale factors for specific models of V1 and V2 and V4 (Freeman & Simoncelli, 2011; Freeman, Ziemba, Heeger, Simoncelli, & Movshon, 2013), although the structure of the stimuli can limit the validity of the model (Wallis, Bethge, & Wichmann, 2016).

Although I don't specifically use metameric images in this dissertation, the concept of the scale factor is key for the design of the stimuli discussed in Chapter 2.In particular, for a finite stimulus window size, the receptive field diameter will increase linearly across the window as a function of eccentricity and therefore the stimulus fringe spacing should match this, in order to reach contrast threshold simultaneously for all the RFs in the window.

### 1.5 Experimental Design Considerations

Based on the characteristics of the eye discussed above, the main elements of the experimental design for the discrimination of the peripheral M and P pathways described in the following chapter are:

a) Detection task to discriminate between the M and P receptive field sizes
b) Tangential pseudo-sinusoidal gratings with linearly increasing spacing to match the underlying scale factor geometry of the RGC RFs
c) Stimuli presented in the periphery to ensure spatial response defined solely by RGCs, in the left nasal visual field only (monocular presentation).
d) Photopic illumination (mean luminance of 105 cd/m$^2$), so cone inputs only to the RGCs.
e) Achromatic stimuli to allow comparison between both M and P RGC responses.

The detail of the experimental methods, data analysis, results and discussion are described in Chapter 2.

### 1.6 The Current Thesis

The first part of Chapter 1 described the contrast sensitivity function and its hypothesised physiological basis in the differential spatial and contrast gain characteristics of the P and M pathways. In particular, it identified a kink in the high-frequency side of the CSF that would arise at the transition between the P and M pathways if the visual system has a "winner takes all" characteristic. The kink has not been detected using simple spatially- and temporally varying stimuli but has been observed using more indirect techniques. The challenge is therefore to design an experiment with stimuli tailored to the underlying physiology to maximise the sensitivity to the predicted kink. The second part of Chapter 1 was a brief review the main features of the human eye, and to explore those aspects that are relevant for developing the tailored stimuli.

Chapter 2 describes the experimental design, methodology, results, and data analysis techniques for the psychophysics experiment with tailored stimuli carried out by three participants. The data analysis makes extensive use of Maximum Likelihood Estimation and the application of Akaike Information Criteria for the determination of the most parsimonious model. Results are presented for models for the participants individually and also for a combined data set of all the participants data. The evidence for supporting the hypothesis is discussed.

Chapter 3 builds on the differentiated pathway model by describing a simple algorithm developed to map the distribution of local contrast in images as a function of scale, to enable a visualisation of how the two pathways differentially transfer information to the LGN and the higher visual system. The algorithm is initially evaluated against sinusoidal images and is then applied to a sample of calibrated achromatic natural images in order to compare with known statistics. Having confirmed the validity of the algorithm, it is then used to generate contrast response images corresponding to the level of

activity (impulses per second) generated in each pathway dependent on the spatial and contrast gain characteristics.

Chapter 4 Discusses the results of the experiment and image analysis and explores the limitations of the current work and potential for future research.

# Chapter 2. Experiment - Psychophysical Discrimination of Parvocellular and Magnocellular Responses in Peripheral Vision

## 2.1 Introduction

*Declaration: This chapter forms the basis of a draft paper to be submitted to the Journal of Vision, co-authored with Iain Gilchrist and Casimir Ludwig. I declare that the experimental study and modelling is my work, and that I am the primary author.*

In Chapter 1, I discussed the hypothesis that the contrast sensitivity function can be modelled in terms of the individual P and M pathway responses, and the potential for psychophysically discriminating between the two contributions. I also reviewed the literature regarding a range of techniques that have been used to test the hypothesis, and showed that despite significant effort, reliable discrimination using simple spatially and temporally varying stimuli has been elusive.

In this chapter, I describe a new methodology for psychophysical discriminating the two pathways, with the experimental parameters optimised for the discrimination task, based on the key features of the peripheral retinal system that I reviewed in Chapter 1.

The psychophysical experiments reported here measure detection thresholds for grating stimuli presented in the periphery. The stimuli were systematically varied in both temporal and spatial frequencies to explore the effect of both parameters on sensitivity. They were presented at a large eccentricity (23.5°) to ensure that the spatial resolution was determined solely by the retinal ganglion cell array spacing. Using model selection, I provide evidence for the contribution of two unique signals in determining changes in sensitivity across spatial frequency. I will argue that these signals correspond to the M and P pathways.

## 2.2 Methods

### 2.2.1 Participants

There were three participants in the experiment (JW, NM, and TH), two were male and one female. Their ages ranged from 22 to 64 years. JW is the primary investigator and NM and TH were naïve to the purpose of the experiment. The participants had normal or corrected to normal vision. Ethical approval for this study was obtained from the School of Psychological Science Research Ethics Committee (2020-6798-6745, 21/10/2020).

### 2.2.2 Apparatus

The stimuli were presented on a gamma-corrected VPixx 3D monitor (VPixx Technologies Ltd, Saint-Bruno, Canada). The display was 1920 x 1080 resolution with a pixel pitch of 0.272mm and a 610mm diagonal. Each of the RGB channels was 10-bit resolution. The scanning backlight functionality was

disabled to allow temporal modulation of the stimuli at up to 60 Hz (based on the 120Hz frame rate). The display was positioned 800mm from the participants eye line, with the head held in a chin/forehead rest. The mean luminance at 50% contrast was 105 cd/m$^2$.

The display was situated in a windowless laboratory with no ambient light. Each participant wore an opaque eye-patch over their right eye and the task was performed using the left nasal visual field. The experiment was controlled by a Windows Personal Computer running Psychtoolbox-3 (Kleiner, Brainard, & Pelli, 2007) in Matlab 2019a (Mathworks Inc., Natick, MA, USA).

### 2.2.3 Stimulus Design

As discussed in Section 1.4.1, the linear increase of RGC receptive field diameter with eccentricity suggests that the maximum sensitivity for discrimination (i.e., lowest threshold) would be achieved with a stimulus that matches the linear RF dependence. For example, if we consider a grating stimulus with a fixed spatial wavelength but an extended spatial extent, the threshold wavelength will vary across the patch. This will give rise to a psychometric function with a shallow slope, and hence a lower signal to noise ratio for the measurement. Therefore, to better match the threshold of the grating across the whole patch as far as possible, the stimuli used in this experiment had a continuously increasing spatial wavelength (swept wavelength) across the patch determined by a linear scale factor. By using a linear swept wavelength sinusoidal grating which approximately matched the scale factor of the RGC spacing (Curcio & Allen, 1990; Dacey, 1993; Drasdo, Millican, Katholl, & Curcio, 2007; Watson, 2014), in principle all the cells whose receptive fields fell within the patch would simultaneously reach threshold. This should maximise the sensitivity for the threshold measurement, with improved contrast resolution.

The equation used to calculate the swept wavelength sinusoidal grating included a quadratic phase term to approximate a linear wavelength ramp (Equation 7), where A(n,m) is a luminance image array of n x m pixels ,$B_1$ is a scaling constant, C is the Michelson contrast, r(n,m) is radial distance from the foveal point, $\lambda_{max}$ and $\lambda_{base}$ define the range of spatial wavelengths, $r_{max}$ is the maximum radial distance and $B_2$ is a scaling constant for the quadratic term.

(7)

$$A(n,m) = B_1\left(1 + C cos\left(\frac{2\pi r(n,m)}{\lambda_{max} - \lambda_{base}(1 - r(n,m)/r_{max}) - B_2 r(n,m)^2}\right)\right)$$

The constants $\lambda_{max}$, $r_{max}$ and $B_2$ were selected empirically to give a linear increase in wavelength within a tolerance of 3% linearity for each stimulus. The scale factor of the swept wavelength gratings ranged from a nominal 0 to 0.024 in steps of 0.001, with 12 bits amplitude resolution. The intercept value was 0.058°, giving a maximum cut-off frequency of 17.2 cpd at the viewing distance of 800mm.

The gratings were oriented tangentially to the horizontal median, with Michelson contrast values from 1.5% -75%. The gratings were presented in the periphery in a broad crescent-shaped patch centred on 23.5 degrees from the fixation point, with a fixation point offset by 420 pixels (6.6 degrees) from the RHS of the screen (Figure 17). The outer edge of the patch was defined by an ellipse with one locus positioned on the fixation point, with the inner edge defined by a circle centred on the fixation point. This specific shape of the patch was derived from a segmented elliptical mask used for early pilot studies of full images, and was used in this study for convenience, rather than being motivated by a specific theoretical justification. The horizontal width of the window was 5.5°, with the overall area of the patch being approximately 55° squared. A linear transition band of 0.9° width was applied around the around the edge of the patch to give a smooth transition from the grey background to the full contrast value of the gratings.



*Figure 17. Example of a test stimulus with a scale factor of 0.016 and 50% Michelson contrast, at a nominal 23.5° eccentricity. The white dot on the right-hand side is the fixation point.*

The specific position of the stimuli in the periphery was a trade-off between working in a region where the spatial acuity is determined by the RGC spacing rather than cone spacing, and also being able to generate spatial sine waves on the display where the cut-off frequency determined by the pixel size was above the expected cut-off frequency of the RGC response.

The test stimuli had variable scale factors in the range 0 – 0.024. Incrementing the scale factors had the effect of incrementing the mean spatial wavelength of the swept wavelength sinusoidal gratings within the patch, such that as the scale factor decreased, the swept wavelengths also decreased (ie the spatial frequency increased).

The reference stimulus had a fixed scale factor of 0.0008. I used a very low scale factor value (with the same mask function as the test stimuli) for the reference rather than a 50% luminance grey screen to avoid potential inadvertent cuing from any mask artefacts. In practice, the reference stimulus was effectively zero contrast for the peripheral presentation. An obliquity correction factor of 0.84 (equal to $\cos^2\varepsilon$, at the eccentricity of $\varepsilon = 23.5°$) was applied to the spatial wavelength values to correct for the use of a flat rather than a curved display.

In addition to variable contrast, the stimuli could also have a sine wave temporal modulation applied at frequencies of 2Hz, 10Hz, 30Hz and 60Hz within the presentation window, corresponding to undistorted sampled sine waves for the 120Hz frame rate of the display. This allowed the effect of temporal modulation on the discrimination thresholds to be measured. It should be noted that in the display mode used (with the scanning backlight disabled), the frequency response at 60 Hz was limited by the rise time of the LCD pixels. This meant that the peak contrast value reached at 60Hz was only 90% of the contrast value at lower frequencies. Therefore, a correction factor of 1.11 was applied to the contrast values at 60Hz.

## 2.3 Procedure

The experimental paradigm was a serial Two Alternative Forced Choice (2AFC) task with the primary dependent variable being the Michelson contrast of he swept wavelength sinusoidal gratings, and the secondary dependent variable being the temporal modulation frequency.

For each trial, the participants were presented with a grey screen (50% luminance) for 1000ms, followed by the first stimulus of 500ms duration, a grey screen for 500ms, and then the second stimulus of 500ms duration. The two stimuli were a test stimulus and a reference stimulus, with the order randomised between each trial.

For each run of trials, the participants were required to fixate on a white fixation mark to the right of the screen throughout the experiment (see Figure 17). The task for the participant was to determine which of the two stimuli intervals had the more visible grating pattern, and then press the appropriate key. When the participant correctly detected the test stimulus the scale factor was decremented by a nominal -0.001 change in scale factor for the next trial. For an incorrect response, the scale factor was incremented by +0.001. It should be noted that this task is discrimination (presence or absence of a stimulus) rather than resolution (determination of form or shape of a stimulus).

Each run consisted of 18 trials, with the initial test stimuli scale factor selected such that the first four or five trials were well above threshold. At the beginning of each run, the participants were therefore easily able to discriminate between the test and reference stimuli (100% accuracy), with the task

becoming more difficult as the test stimulus scale factor decreased, such that for the later trials the participants were performing at chance (50% accuracy).

For each threshold estimate, there were seven runs, equivalent to 126 trails per estimate. Threshold estimates were carried out at 16 different Michelson contrast values in the range 1.5%-75%. The threshold estimates at each contrast value were repeated with temporal modulation frequencies of 2Hz, 10Hz, 30Hz and 60Hz,

The participants conducted several practice runs at the beginning of the experiment to familiarise themselves with the experimental arrangement. The participants could rest at the end of each run, , as required.

JW and NM collected data at all four temporal modulation frequencies; TH collected data at 2Hz, 10Hz and 30Hz. The complete data set for each participant was therefore approximately 8000 trials, with each participant recording data on different days over several weeks.

## 2.4 Data Analysis

The role of the staircase data was to generate the sampling of scale factors to be shown to the participants in each trial. For each threshold estimate, a plot of percentage correct versus scale factor generated a sigmoidal psychometric function, with the percentage correct being near 100% at high scale factors and near chance (50% at low scale factors). The psychometric functions were fitted to a cumulative Gaussian sigmoidal function using the Psignifit code v4 for the 2AFC paradigm (Schutt, Harmeling, Macke, & Wichmann, 2016). The threshold scale factor was defined as the "75% correct" point on the fitted sigmoid function. Threshold scale factors (and 95% credible interval values) were determined accordingly for the threshold estimate at each value of contrast and temporal frequency.

The threshold scale factors were subsequently converted to threshold spatial wavelength values by multiplying the threshold scale factor by the nominal eccentricity of the stimuli (23.5°) and then adding the intercept value (0.058° (see Section 2.2.3)).

Model fitting for the contrast sensitivity function models was performed using Maximum Likelihood Estimation (MLE). The MLE code was written in MATLAB, using the "fminsearchbnd" function which performed a bounded Nelder-Mead simplex algorithm (Lagarias, Reeds, Wright, & Wright, 1998). Starting values for each parameter were generated randomly.

Selection of the most parsimonious model was based on the corrected Akaike Information Criterion $AIC_C$, which penalises more complex models based on their parameter count. Corrected Akaike Information Coefficients ($AIC_C$) are recommended for smaller datasets when there are fewer than 40 data points per parameter (Wagenmakers & Farrell, 2004). The AICc values were converted into Akaike weights, which may be interpreted as the probability of a model being the best model (given

the data and total set of candidate models) in terms of its Kullback-Leibler distance (Wagenmakers & Farrell, 2004). The Akaike weights were also used to determine the evidence ratios for each model (i.e., how much more/less likely one model is compared to another).

## 2.5 Results

### 2.5.1 Threshold Spatial Wavelength as a Function of Contrast

Figure 18 shows an example of the measured threshold spatial wavelength versus contrast for all three participants at a 10Hz temporal modulation frequency.
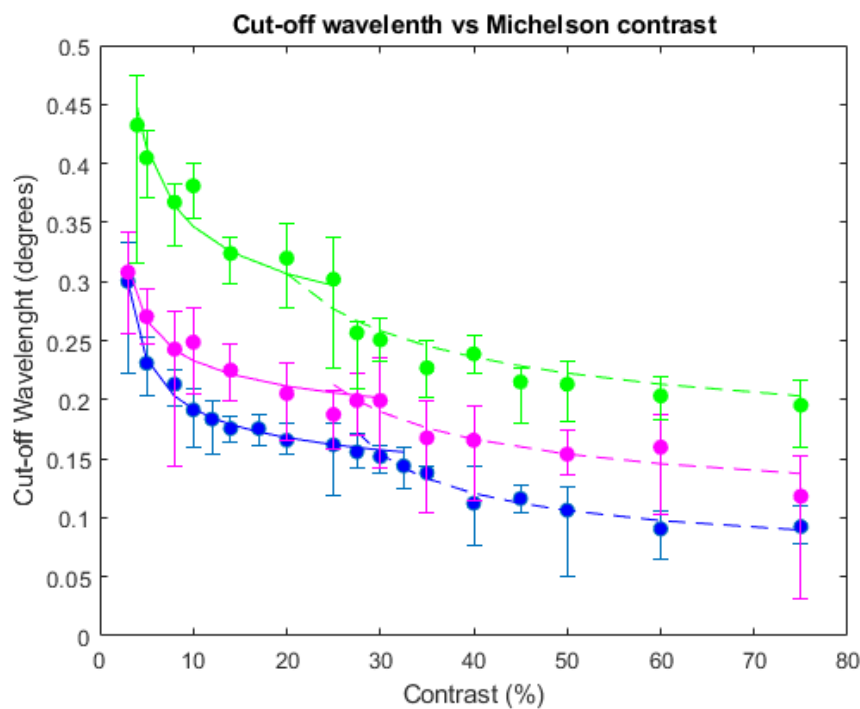


*Figure 18. Example threshold spatial wavelength data for JW (blue), NM (magenta) and TH (green) for 10Hz temporal modulation. The solid and dotted curves are dual-segment model fits discussed in the "Model Fitting" section. The error bars are the 95% credible interval limits.*

The key observation is that there appears to be a kink in the contrast threshold curve at approximately 25% contrast for all three participants. This kink separating two curved segments is a feature of these data sets at all temporal frequencies. This functional shape is subsequently referred to as a *dual-segment curve*. A formal, statistical assessment of the extent to which these data are better described with a single curve, or two curves is reported below.

### 2.5.2 Contrast sensitivity functions

The threshold spatial wavelength versus contrast data was re-plotted as a CSF function, by plotting the inverse of the contrast (i.e., contrast sensitivity) on the y axis and the inverse of the threshold spatial wavelength (i.e. the threshold spatial frequency) on the x axis, as shown in Figure 19. The CSF presentation shows the kink more clearly in many (but not all) of the plots. Note that the figure shows only the high frequency side of the CSF where I collected the data.
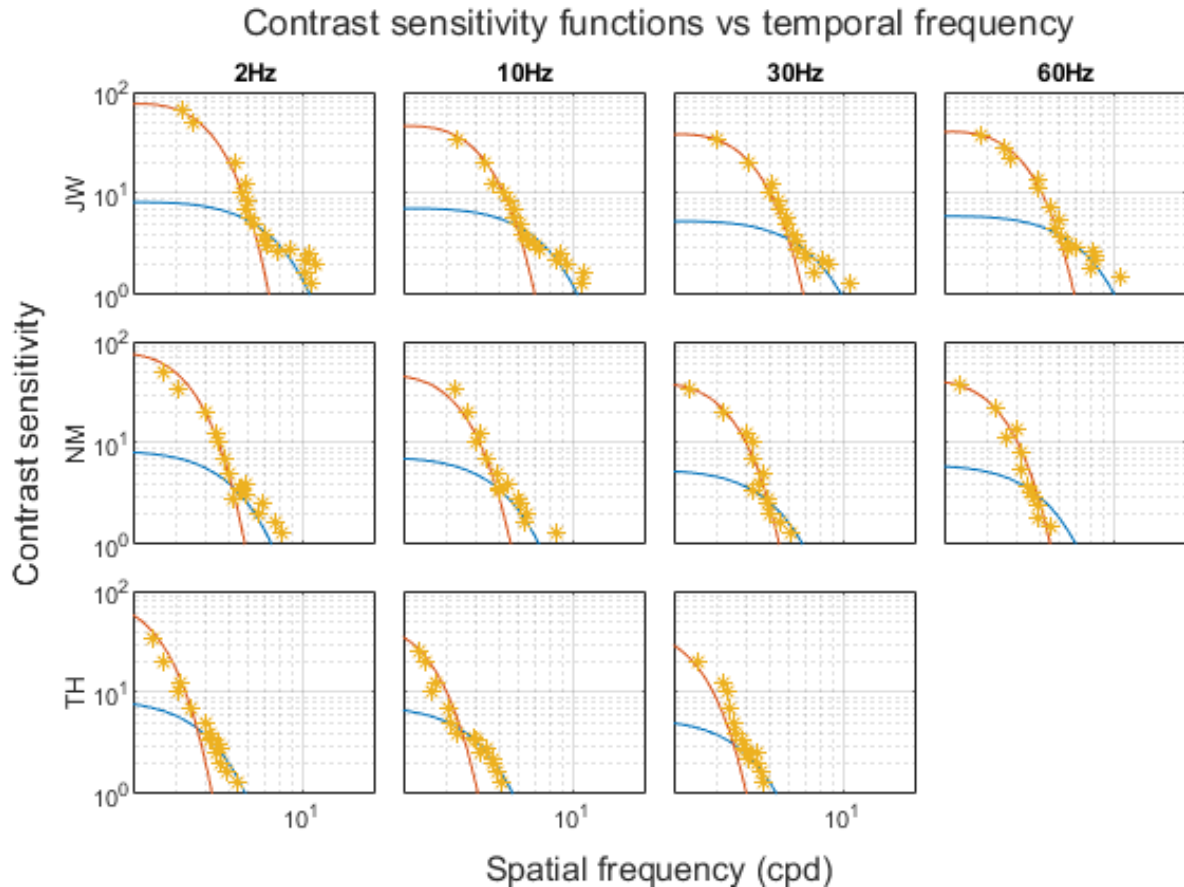


*Figure 19. Contrast sensitivity functions for JW (top row), NM (middle row) and TH (bottom row), at 2Hz, 10Hz, 30Hz and 60Hz temporal modulation. The red and blue curves are the model fit for a 16-parameter frequency Gaussian model discussed in the Results section.*

Figure 19 illustrates three characteristics of the data. First, the dual segment curve function is evident for all participants at most temporal frequencies. Second, the most experienced observer (JW) has the highest threshold spatial frequencies (lowest threshold wavelength values). And third, the 2Hz data for all participants has the highest contrast sensitivity values, for both segments.

The two components of the dual-segment curves correspond to a high contrast sensitivity/low spatial frequency segment, and a low contrast sensitivity/high spatial frequency segment.

## 2.6 Model Fitting

The aim of the modelling was to address the following questions. First, is a single or dual segment model more parsimonious? Second, can a single underlying model be applied to all participant's data? Third, can the model give some insight into the physiology of the underlying processes, aside from simply being a parsimonious description of the data?

The initial model I analysed used a simple power law, which has been used to successfully describe previous studies of dual-segment type responses such as contrast-dependent reaction times (Murray & Plainis, 2003). I also evaluated a Gaussian function in the spatial frequency domain, as an approximation to the standard Difference of Gaussian (DoG) function which is typically used to characterise the centre-surround spatial sensitivity of RGCs (Cope, Blakeslee, & McCourt, 2013). Ideally, I would have modelled the DoG directly, but I lacked data on the low frequency side of the peak, such that the model for the DoG would not converge.

### 2.6.1  Individual data set model fitting

Individual participant modelling was initially carried out in the spatial wavelength domain and based on a power law function of contrast C.

(8)

$$\lambda = k(C - C_{min})^{-a} \quad for \; C > C_{min}$$

where $\lambda$ is the cut-off wavelength, $k$ is a constant related to the limiting cut-off wavelength at 100% contrast, $C_{min}$ is the asymptotic value of the contrast and $a$ is the exponent.

We also evaluated a Gaussian function in the spatial frequency domain. To allow comparison with the power law model, the Gaussian model was transformed from the frequency domain into the wavelength domain, resulting in the following equation.

(9)

$$\lambda = \frac{1}{\left(k_2 + \sqrt{2}\sigma\left(-log\left(\left(\frac{1}{CC_{min}}\right)^{0.5}\right)\right)\right)} \quad for \; {^C/_{C_{min}}} > 1$$

where $\lambda$ is the cut-off wavelength, $k_2$ is the centre frequency for the Gaussian in the spatial frequency, $C_{min}$ is the asymptotic value of the contrast and $\sigma$ is the standard deviation of the Gaussian in the spatial frequency domain.

For both models we included parameters for the dual segment structure and for the different temporal frequencies. For the models reported here, there were approximately 5-20 data points per parameter, respectively.

For each model, the same functional form was used for the two segments, but with different parameters. Of the two solutions for each segment, the most sensitive one (i.e., the lowest cut-off wavelength) was used for each data point in the MLE optimisation algorithm, on the assumption that the visual system responds to the most sensitive of the available channels channel rather than adding the contributions of the two channels ("winner-takes-all" model) (Murray & Plainis, 2003; Pokorny, 2011).

If each data set had two segments, and given 4 temporal frequencies, then a full description of each individual's dataset would require 25 parameters: 4 (temporal frequencies) x 2 (segments) x 3 (parameters per segment), plus one additional parameter for the Gaussian link function used to compute the likelihood of the data under the model. However, inspection of the data suggested that for each participant, the underlying cut-off wavelengths for each segment were common across the temporal frequencies, whereas the minimum contrast sensitivity values were dependent on the temporal frequencies. Accordingly, models with fewer, common, parameters were investigated, on the assumption that the full-blown model is over-specified.

The models investigated included a set of nested factors: Power law vs frequency Gaussian functions (labelled P1-P6 and G1-G6, respectively); single vs dual segment functions; and temporal frequency dependence vs independence. Given the large number of parameters, and that the MLE fitting process is non-deterministic, to ensure that the model was finding the minimum value I ran each model 64,000 times in blocks of 8000 so that I could check that the minimum values of the function were consistent for each model. The results of the model fitting are shown in Table A1 in Appendix A.

For each model I calculated the corrected AIC values, together with the Akaike weights. To determine strength of evidence in favour of a particular model, I calculated the evidence ratios and normalised probabilities for the different models. The evidence ratios were calculated by summing the Akaike weights for one model class e.g., frequency Gaussian and dividing by the sum of the Akaike weights for the complementary model class e.g., Power Law.

From this analysis, I was able to identify the Best and Next Best model fits for each participant, with the 12-parameter frequency Gaussian model with dual segment and frequency dependence (labelled G4) being the Best fit in each case and two other models being identified as the next best model depending on the participant:  G5 (13 parameter frequency Gaussian) for NM and P5 (12 parameter Power Law) for TH and JW. The results for the best and next best models are shown in Table 1 below.

| Participants | Best Model | Best AW | Next Best Model | Next Best AW | Evid ratio Best/Next | Norm prob Best/Next | Evid ratio Gauss/Power | Evid ratio Dual/Single | Evid ratio Freq dep/ind |
|---|---|---|---|---|---|---|---|---|---|
| JW | G4 | 0.83 | G5 | 0.17 | 4.8 | 0.83 | 84243 | 3.7E+14 | 5.1E+20 |
| NM | G4 | 0.66 | P5 | 0.18 | 3.8 | 0.79 | 4.6 | 2.9E+09 | 6.0E+15 |
| TH | G4 | 0.65 | G5 | 0.27 | 2.4 | 0.71 | 12.1 | 5.8E+02 | 1.6E+04 |

*Table 1. Comparison of the evidence ratios and normalised probabilities for the Best and Next Best models, and the evidence ratios for Gauss vs Power law, dual versus single curve, and frequency dependent vs frequency independent, for each participant.*

There are three key observations from this model fitting exercise. First, across all three participants the frequency Gaussian function (model G4) is the preferred model. Second, as this model includes dual segments this suggest that the data is best modelled with this feature. And third, the evidence ratio for the model that includes temporal frequency dependence strongly supports the inclusion of this factor in the models. Overall, the most parsimonious fit is the 12-parameter dual-curve frequency Gaussian model.

At this point, given the strong evidence for the 12-parameter frequency Gaussian model with dual segment and temporal frequency dependency (G4) for all three participants, I decided to determine if there was a simple systematic relationship between the visual responses of all three participants. I therefore combined the datasets of all three participants (for all temporal frequencies) into a single dataset and applied the same MLE model fitting process.

### 2.6.2 Combined data set model fitting

The starting model for this analysis was a 34-parameter frequency Gaussian which treated each participants' data sets as an independent 12-parameter models as determined in the previous section (with 10 for TH's data), albeit within the same MLE fitting function. Simplified models with reduced parameter sets were then investigated, based on the observation that the individual data sets could be approximately overlaid either by applying a scaling (multiplicative) factor to the cut-off wavelength values (movement along the cut-off wavelength x-axis), or by adding an offset (movement along the contrast y-axis), as can be seen by inspection of Figure 2. For these models I used the JW dataset as the base model with the minimum number of additional parameters for each of the other participants data sets (plus the standard deviation of the Gaussian link function). I also included three Power Law models (labelled P6-P8) for comparison to check whether the evidence ratio for the Gaussian models (labelled G6-G10) remained high.

The results of the combined model fitting are shown in Table B1 in Appendix B.

To determine strength of evidence in favour of a particular model, I calculated the evidence ratios and normalised probabilities for the different models summarised in Table 2. I determined that the Best Fit model was the 16-parameter frequency Gaussian, dual segment, frequency dependent model with multiplicative factors, labelled G7. This is the same model that was selected for the individual participants with two additional parameters per participant to account for inter-participant differences.

| Best Model | AW | Next Model | AW | Evid ratio Best/next | Norm prob Best/next | Evid ratio Gauss/Power | Evid ratio Dual/single |
|---|---|---|---|---|---|---|---|
| G7 | 0.71 | G10 | 0.23 | 3.1 | 0.76 | 42.6 | 9.2E+09 |

*Table 2. Comparison for Best and Next Best models for full dataset, with evidence ratios for Gauss vs Power Law and Dual vs Single curve*

There are three key observations from the modelling of the combined data sets. First, the preferred model (with an evidence ratio of 3.1 compared to the next best model) is the 16-parameter frequency Gaussian, with scale factors favoured for the additional participants (rather than additive terms). Second, the evidence ratio for Gaussian vs Power Law is 42.6, which is very strong evidence in favour of that model. And third, as with the individual data, the evidence ratio for dual vs single segment curves strongly favours the dual curve model.

At this point, I have identified a strong underlying functional model (16 parameter dual curve frequency Gaussian) that fits the combined data set of all three participants. The parameter set for the model is given in Table 3. This is the model and parameter set that is plotted in Figure 19.

| | Units | JW | NM | TH |
|---|---|---|---|---|
| Centre frequency of Gaussian, $k_2$ | cpd | 2.54 | | |
| Standard deviation of M pathway Gaussian, $\sigma_M$ | cpd | 1.56 | | |
| Standard deviation of P pathway Gaussian, $\sigma_P$ | cpd | 3.89 | | |
| Peak contrast sensitivity of M pathway at 2Hz, $1/C_{minM2}$ | | 69.0 | | |
| Peak contrast sensitivity of M pathway at 10Hz, $1/C_{minM10}$ | | 42.8 | | |
| Peak contrast sensitivity of M pathway at 30Hz, $1/C_{minM30}$ | | 34.4 | | |
| Peak contrast sensitivity M pathway at 60Hz, $1/C_{minM60}$ | | 37.8 | | |
| Peak contrast sensitivity P pathway at 2Hz, $1/C_{minP2}$ | | 9.29 | | |
| Peak contrast sensitivity P pathway at 10Hz, $1/C_{minP10}$ | | 7.13 | | |
| Peak contrast sensitivity P pathway at 30Hz, $1/C_{minP30}$ | | 5.87 | | |
| Peak contrast sensitivity P pathway 60Hz, $1/C_{minP60}$ | | 5.08 | | |
| Multiplicative factor M NM | | | 1.26 | |
| Multiplicative factor P NM | | | 1.44 | |
| Multiplicative factor M TH | | | | 1.73 |
| Multiplicative factor P TH | | | | 1.87 |

*Table 3. Parameter set for the best-fit 16 parameter scale frequency Gaussian model for the combined data set, based on Equation 9.*

Three important observations can be made regarding this model. First, only two multiplicative factors (one for each segment) are required to fit each additional participant to the base frequency Gaussian functions (corresponding to the dual curves). Second, the peak contrast sensitivity for each temporal frequency and segment are common for all three participants. And third, these results strongly suggest a common underlying process determining the cut-off threshold measurements for all three participants.

It should be noted that the 16-parameter model only has a single, common, parameter value for the centre frequencies of the two Gaussian functions (M and P). In practice, we would expect to have independent centre frequencies, and as such the 16-parameter model might be regarded as less realistic. Nevertheless, it appears that the current data did not warrant inclusion of separate centre frequencies, so we proceed with the 16-parameter model for the following analysis and discussion.

Having established the most parsimonious fit, I can use the values of the peak contrast sensitivity as a function of temporal frequency (from Table 3) to plot the inferred temporal contrast sensitivity for both segments of the fitted function (Figure 20) at the peak frequency of 2.54 cpd.
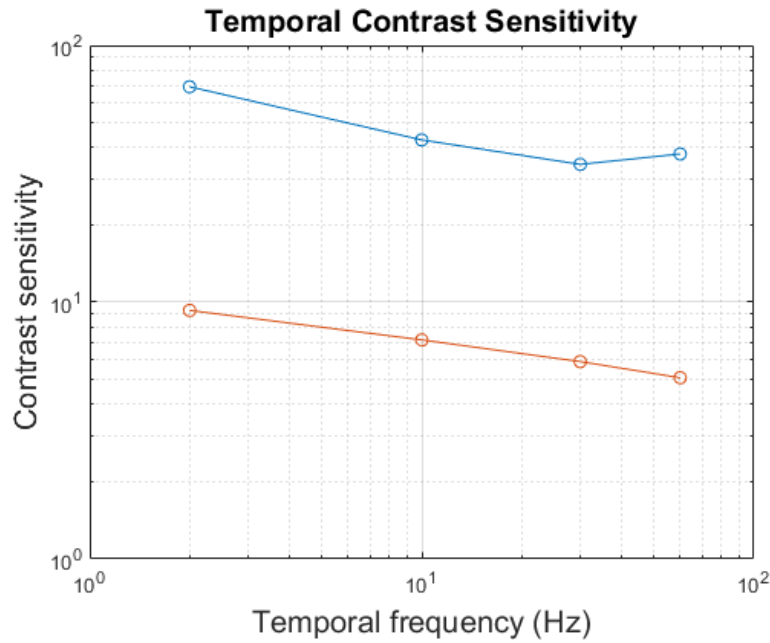
*Figure 20. Inferred peak temporal contrast sensitivity functions at 2.5 cpd based on the 16-parameter frequency Gaussian model for JW, NM, and TH combined dataset (Table 3). The blue curve is for the low-contrast segment, and the red curve is for the high-contrast segment.*

For both segments that the highest contrast sensitivity is observed for 2Hz temporal modulation, with the sensitivity dropping at higher temporal frequencies. The peak contrast sensitivity for the high-sensitivity curve is approximately 8 times that of the low contrast sensitivity curve.

In summary, I have demonstrated using these stimuli and methods that we can differentiate between two segments of the contrast sensitivity function. In addition, the inter-participant variation is described simply by two multiplicative parameters per participant, one for each segment, suggesting a common underlying functionality across all participants. In the next section I argue that two segments represent the M and P pathway contrast response, respectively.

## 2.7  Discussion

Having derived a parsimonious model that describes the dual segment contrast sensitivity data in the spatial frequency domain, we wanted to test the evidence that the two segments correspond to the M and P pathways.

### 2.7.1   Does The Spatial CSF Data Support The Claimed Discrimination of the M and P Pathways?

Previous psychophysical studies of discrimination acuity in the periphery (c. 25° eccentricity) have found cut-off frequencies ranging from 6 cpd (Anderson, Zlatkova, & Demirel, 2002; Koenderink, Bouman, Buenodemesquita, & Slappendel, 1978) for presentation of grating stimuli on displays to cut-

off frequencies of up to 30 cpd in experiments using visometers to directly project gratings onto the retina (Thibos, Cheney, & Walsh, 1987; Zhu, Zele, Suheimat, Lambert, & Atchison, 2016). The data reported here is consistent with the values for the studies presenting grating stimuli on displays.

However, where my results differ from the conventional contrast sensitivity function measurement is that I focused our data collection on the high-frequency side of the function. This was done in order to facilitate discrimination between the M and P pathways where the respective contributions would be most separable in a winner-takes-all model. Other differences in methodology include using:

a) Tangential gratings rather than straight, parallel gratings.
b) Linearly ramped fringe spacing in the stimuli to maximise sensitivity of the PSE function.
c) Narrowly spaced increments in spatial wavelength (c. 0.02° per increment) to maximise sensitivity to any kink in response.
d) A relatively large-area stimulus (c. 55° squared)
e) Presentation of the stimuli in periphery (23.5°) where the visual acuity is dependent only on RGC spacing and not cone density.
f) Stimuli presentation in single visual field (monocular, left nasal) to maximise sensitivity to the PSE function.

It is proposed that these methodological differences are what has enabled the detection of the dual segment structure, which we can relate to the known spatial dimensions of RGC receptive fields.

As discussed in the Introduction, Kaplan and colleagues hypothesised that the shape of the primate contrast sensitivity function could be explained by combining the known physiological contrast gain functions of P and M cells (Kaplan 2013) with the Difference of Gaussian (DoG) frequency response function arising from the centre-surround opponency (Rodieck 1965, Enroth-Cugell 1966). The relevant equations defining the relationship between the spatial frequency and spatial DoG functions are given in Section 1.2.3.2 (Equations 3a and 3b).

Although the parsimonious model was a frequency Gaussian model, I was able to fit it to the DoG in the spatial frequency domain using equation 3b, as the functional shapes are similar in the spatial frequency range of interest. As the experimental set-up was optically uncorrected for off-axis imaging, in order to estimate the DoG for the underlying retinal ganglion cell geometry a representative modulation transfer function (MTF) first needed to be applied to the data. The MTF function used was a double-exponential function (Williams et al., 1996):

(10)

$$M(s) = (1 - c)e^{-af} + ce^{-bf}$$

Where f is the spatial frequency and the coefficients a, b and c were taken from Table 1 of (Williams et al., 1996) corresponding to the circle of least confusion at 20° eccentricity.

Using the frequency DoG fit to the data, I was able to determine the corresponding full width half maximum (FWHM) values of the corresponding spatial DoG structures for the M and P pathways. The fit is shown in Figure 19.
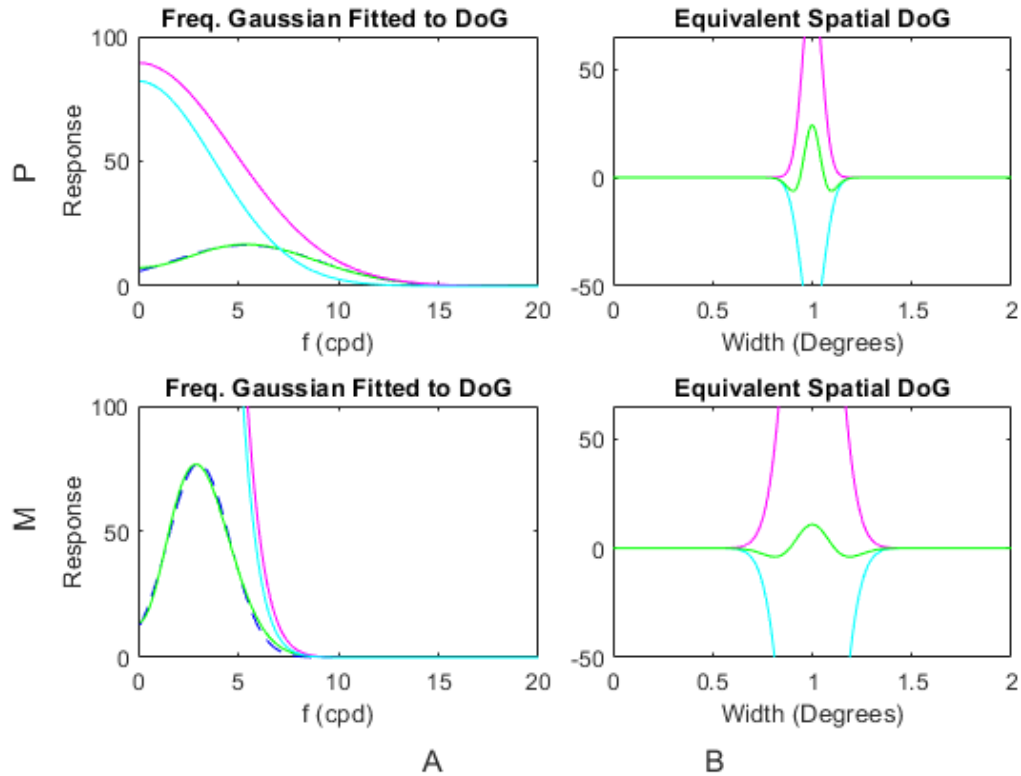


*Figure 21. Top row is based on the MTF-corrected P pathway data. (A) is the frequency Gaussian model (black dashed line) fitted to the frequency DoG (green line), with estimated centre and surround functions shown in mauve and blue, respectively. (B) is the equivalent spatial DoG structure. The bottom row is the same for the MTF-corrected M pathway data (C) and (D).*

The frequency DoG (green line) is a reasonable fit to the frequency Gaussian function (black dashed line) for both the P and the M pathways. However, in running the model fit it was clear that the centre and surround amplitudes and radii are poorly determined, as the lack of low frequency data means that the surround function is poorly constrained. That said, the DoG function is well-determined, such that the FWHM of both the frequency and the spatial DoGs can be calculated, and then compared to published data for RGC dendritic and receptive fields, as shown in Table 4.

| Measurement | Dimensions | Parameter | References | Eccentricity | |
|---|---|---|---|---|---|
| Psychophysical contrast sensitivity – population receptive field | P = 0.07°- 0.13° M = 0.14°- 0.24° | Spatial DoG FWHM | This dissertation | 23.5° | Values for JW, Nm and TH based on data in Table 3, corrected for MTF |
| Dendritic field size in human retinas – single cell | P = 0.12° - 21° M = 0.61° - 82° | Diameter | (Dacey & Petersen, 1992) | 23° | Values estimated from Figure 2 of ref. |
| Receptive field sizes in primates (macaques) -single cell | P = 0.14°-0.30° M = 0.30° - 0.55° | Spatial DoG FWHM | (Croner & Kaplan, 1995) | Averaged over the range 20°--30° | Derived from values from Table 1 of ref. |
| Dendritic field size in macaque retinas (nasal) – single cell | P = 0.06° – 0.22° M = 0.30° – 0.70° | Diameter | (P. Martin & Grunert, 2003) | 23° | Values estimated from Figure 26.4 (modified from Watanabe 1989) |

*Table 4. Comparison of the psychophysical FWHM spatial DOG estimates with physiological estimates of primate and human receptive field and dendritic field diameters.*

Note that the physiological data in Table 4 includes both human and macaque studies. Dacey reported that for eccentricities near 25 degrees the ratios of human to macaque dendritic field diameters were approximately 1.0 and 1.3 for P and M RGCs, respectively (Dacey & Petersen, 1992), I therefore consider both data types to be valid comparators.

It can be seen from Table 4 that the psychophysical FWHM values are within a factor of two of the physiological data for the P pathway, and slightly higher for the M pathway. Given the significant differences in methodology, in particular the comparison of population RF estimate to single cell measurements, and that FWHM measurements are likely to underestimate visual estimates of dendritic field diameter, I consider that the comparative receptive field/dendritic field diameter data supports the identification of the dual segments as corresponding to the M and P pathways.

### 2.7.2 Does the Temporal CSF Data Support the Claimed Discrimination of the M and P Pathways?

Kelly (1984) studied the retinal spatiotemporal CSF across a range of eccentricities (using circular radial gratings with mean eccentricities of 0°, 3°, 6° and 12°). For all eccentricity values, when measured using the spatial frequency corresponding to the peak of each spatial CSF at 0.5Hz, the temporal CSF was a low pass response with a knee at approximately 10Hz, and a cut-off frequency of approximately 30-40Hz. For lower spatial

frequencies (i.e., a factor of five below the peak spatial frequencies), the temporal CSF was a bandpass response for all eccentricities, with the peak responses in the range 3-7Hz, dependent on eccentricity. A low-pass response at high spatial frequencies is consistent with other authors (Li, Gi and Wang, 2012; Robson, 1966; Virsu, Rovamo, Laurinen & Nasanen, 1982).

Kelly also noted for the lower spatial frequencies that there was an enhanced response (ie higher cut-off frequency) at higher eccentricities. Measurements using uniform, patternless, stimuli confirmed this enhanced flicker response at increasing eccentricity, which Kelly interpreted as being a purely temporal phenomenon, at zero spatial frequency. The extrapolated cut-off frequency was more than 50Hz.

Kelly's study did not specifically differentiate between potentially different pathways (magnocellular and parvocellular) but treated the measured CSFs as a single pathway. In contrast, Merigan et al (1993) used lesion studies to differentiate between the spatiotemporal characteristics of the M and P pathways in macaques. These studies demonstrated that the M pathway primarily transmits high temporal/low spatial frequency luminance information, and the P pathway transmits primarily low temporal/high spatial frequency luminance information. Therefore, within the overall temporal CSF envelope, and for a given spatial frequency, the M pathway contributes the high temporal frequency response, and the P pathway contributes the low temporal frequency response.

Therefore, based on the Kelly and Merigan studies, the predictions for the temporal CSFs reported in this chapter would be that:

a) Given that the value of the contrast sensitivity at each temporal frequency was determined at the spatial frequency of the peak of the spatial CSF response (i.e., 2.5 cpd), the temporal CSF function of the M pathway in Figure 20 should be a low pass response with a knee at approximately 10 Hz, with a peak contrast sensitivity of approximately 100.

b) The P pathway CSF should also be a low pass response but with a knee below 10 Hz, with a peak contrast sensitivity of approximately 10.

c) There should not be an enhanced flicker response for the M pathway, as the luminance values of sinusoidal grating stimuli were symmetric around the 50% level,

such that there should be no average luminance signal over the whole patch which might trigger the flicker response.

Comparison of these predictions with the results shown in Figure 20 is limited given the poor temporal resolution (i.e., data points only at 2Hz, 10 Hz, 30Hz and 60Hz). However, we observe in Figure 20 that:

i) The M pathway temporal CSF does have a low pass response down to 30Hz, the peak sensitivity is approximately 100, but an enhanced response is visible at 60 Hz which obscures any knee which might be present at 10Hz. This could be due to a flicker response arising from a residual luminance signal i.e., if the grating stimuli peaks and troughs were not in practice perfectly balanced around 50% luminance.

ii) The P pathway temporal CSF also has a low pass response, the peak sensitivity is approximately 10 but the knee is significantly higher than 10 Hz, which is inconsistent with the Merigan data. This could be due to aliasing from the RGCs sampling array, although no evidence of aliasing was observed by participant JW at threshold, although it was observed well above threshold.

Therefore, the M and P pathway temporal CSF functions plotted in Figure 20 do not conclusively support the claimed discrimination of the M and P pathways but may include contributions from enhanced flicker detection and aliasing, respectively. Further research would need to be carried out to resolve this uncertainty.

### 2.7.3 Other Questions
The results raise some additional questions.

First, what underlies the differences in multiplicative factors determined for the participants in the experiment? The simplest argument is that the relative multiplicative factors arise from differences in the individual RF sizes (and hence implied RGC spacing). The variation of data reported here is consistent with reported variation of inter-participant RGC spacings (McKendrick & Johnson, 2000; Wilkinson, Anderson, Bradley, & Thibos, 2016) and of inter-participant V1 cortical magnification values (Himmelberg, Winawer, & Carrasco, 2020).

Secondly, there is the question of why the M and P pathway physiological parameters have the values that they do? One way to think about this question is to consider what the limiting physical factors are that arise from the geometry of the lens of the eye, combined with the sampling density of the retinal ganglion array. It was hypothesised by Williams (Williams et al., 1996) that aliasing of fringe stimuli arising from the Nyquist sampling limit of the P RGC array at high eccentricities would largely, but not completely, be suppressed by the effect of the MTF for off-axis measurements. As such, this combination of physical effects might be the limiting envelope for peripheral visual acuity. I therefore compared the combination of MTF/aliasing with the frequency Gaussian model (Figure 22).
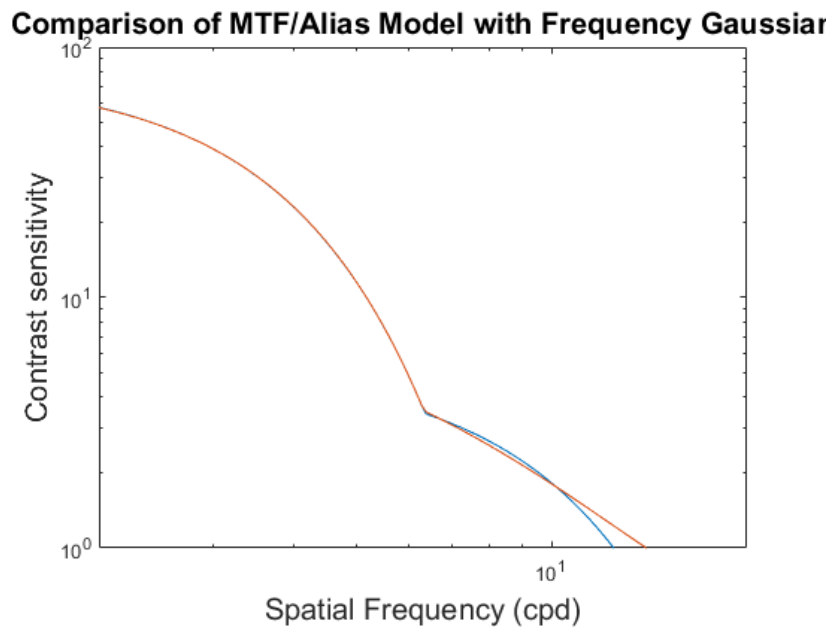


*Figure 22. Comparison of MTF/aliasing model (red) (assuming a simple Gaussian function for the low-frequency curve and a 6.3 cpd Nyquist frequency for the pathway (Williams et al., 1996)) to the frequency Gaussian model (blue).*

The two models are similar across the range of spatial frequencies, except close to cut-off. As such, the measured M and P physiological response is a close match to the limits arising from the physics of the lens and RGC array spacing. One might therefore argue that the M and P pathway detection sensitivities are evolved to be well-matched to both the optics of the eye and the limits imposed by the sensor array.

## 2.8 Conclusions

In the introduction, I described the challenge of psychophysical differentiation of the spatial and temporal frequency characteristics of the M and P channels, and the consequent development of more indirect methods. However, the results reported here suggest that it is possible to

psychophysically discriminate the hypothesised dual-segment characteristic of the contrast sensitivity function using independently spatially and temporally varying stimuli. Using a discrimination paradigm, I have shown that this behaviour is both reproducible across multiple participants and consistent with the known contrast gain and spatial physiological characteristics of the P and M pathways in the primate visual system. The results support the hypothesis that the measured psychophysical achromatic contrast sensitivity function of the primate visual system can be explained by combining the P and M retinal ganglion cell responses (Kulikowski, 1989; Kaplan, 1990). The results are also consistent with previous observations that the overall system response is that of the most sensitive of the two channels, rather than summing the two channel responses

**Chapter 3 Image Analysis and Visualisation of the Contribution of the M and P Pathways**

**3.1 Introduction**

In the previous chapter, I reported on the direct psychophysical discrimination of the M and P pathways at an eccentricity of 23.5 degrees in the left nasal visual field. I determined both the spatial frequency response and the contrast sensitivity of each pathway. Using this data and the known contrast gain functions, I was able to infer the spatial scale of the receptive fields of the M and P retinal ganglion cells, described in terms of difference of Gaussian functions.

In principle, this information can be used to understand how these channels differentially respond to natural images projected onto the periphery of the retina. The differential responses will depend on the characteristic scale for each channel, and the contrast gain function. Therefore, the first step is to understand how natural images are characterised in terms of the local contrast as a function of scale. Using that local contrast information, we can then model the impact of the pathway contrast gain characteristics on the images to determine the differential response.

This chapter is split into two sections. In the first section, I present a novel technique for determining local contrast as function of scale. I use this technique to analyse both sinusoidal fringe images and natural images in terms of contrast and mean luminance, and then relate those results to the known characteristics of the images and published studies. Having demonstrated that the technique is valid, in the second section I use the model to apply the relevant contrast gain functions at the characteristic scale for each channel, and then map the localised contrast response images (which are the contrast response function of the model mechanism) onto the original images. This generates a visualisation of the characteristic responses in the periphery of the two pathways.

**3.2 The Statistics of Natural Images**

The statistics of natural images has been extensively studied, exploring general statistics (Peli, 1990; Ruderman, 1994), the relationship between image statistics and cellular responses (X. W. Cao, Merwine, & Grzywacz, 2011; Field, 1987), correlation between local luminance and contrast (Frazor & Geisler, 2006; Geisler, 2008; Lindgren, Hurri, & Hyvarinen, 2008; Peli, 1990), image statistics and higher level responses (Ghodrati, Ghodousi, & Yoonessi, 2016; Scholte, Ghebreab, Waldorp, Smeulders, & Lamme, 2009) and more recently high-level characterisation of images in large databases based on contrast and luminance statistics (Harrison, 2022). In general, these studies have analysed the population statistics of complete images or image sets, with limited analysis of contrast and luminance within the images as a function of local scale and position.

For this study, I wanted to be able to visualise how the M and P pathways in the periphery differentially respond to local contrast on actual images, rather than simply establishing the overall statistics for a set of images. To do this, I needed to be able to quantify contrast as a function of local scale, for a fixed array of cells (or patches) across each image. This enabled me to both analyse how

contrast varies with local scale, and to then model how the differential contrast gain characteristics of the two pathways modulate the perceived image as a function of position.

I therefore decided to develop a simple algorithm to first determine the local contrast variation across images, and then use these contrast maps with the known contrast gain characteristics of the two pathways to transform the images into contrast response images, effectively modelling the spatial distribution of retinal ganglion cell (RGC) outputs for both M and P peripheral pathways.

The starting point of the image analysis process is determination of the local contrast.

### 3.3 Determination of Local Contrast

Local contrast can be defined in three ways, namely:

$$(11)$$

Michelson contrast: $C_m = (L_{max} - L_{min})/(L_{max}+L_{min})$

$$(12)$$

Weber contrast: $C_w = (L_{max} - L_{min})/L_{background}$

$$(13)$$

RMS contrast: $C_{RMS} = L_{RMS}/L_{mean}$

Where $L_{max}$ and $L_{min}$ are the maximum and minimum luminance in a specified array of luminance values $L_{background}$ is the background luminance, $L_{RMS}$ is the standard deviation of the luminance and $L_{mean}$ is the mean luminance.

Michelson contrast is most relevant where the images area well-defined sine waves (such as Gabor patches), Weber contrast for letter stimuli and RMS contrast for natural images (Pelli 2013). Therefore, for this study I have used RMS contrast.

The image processing was carried out using MATLAB (Mathworks Inc., Natick, MA, USA). For determination of the standard deviation I utilised:

> **stdfilt(A, nhood)** which applies standard deviation filtering of an image array A. Each pixel of the output array is the standard deviation of a *nhood x nhood* array. So, for example if I set *nhood =3*, "stdfilt" will determine the standard deviation of a 3x3 set of elements around each pixel. The parameter nhood effectively sets the scale over which the standard deviation function is evaluated. The output is an array the same size as the input array, with each element of the array being the local standard deviation.

For the evaluation of the mean, I utilised:

**imgaussfilt(A, sigma)** which calculates the Gaussian weighted mean of a range of cells defined by a standard deviation of sigma.

Using the MATLAB matrix functionality, for an luminance image array defined a $A(i,j)$, I can define local RMS contrast $L(i,j)$ as

$$J = stdfilt(A, m) \tag{14}$$

$$K = imgaussfilt(A, m/C_1) \tag{15}$$

$$L = C_2 .* J./L \tag{16}$$

Where $J$ defines the local standard deviation of the luminance for an m x m array, $K$ defines the Gaussian weighted mean of the luminance and $L$ is the local RMS contrast. The constant $C_1$ is necessary to approximately match the dimensions of the square m x m array used by stdfilt to the Gaussian weighting with a standard deviation of $m/C_1$ used by imgaussfilt. The constant $C_2$ is to calibrate the calculated contrast values defined by equation (6) to accurate Michelson values of contrast when evaluating simple sinusoidal fringe images.

In practice, the contrast value $L(i,j)$ defined using equation 6 determines the contrast for every pixel in an array. However, I want to determine the contrast values for non-overlapping cells of differing scale. I do this by extracting the centre value for a given cell size.

### 3.3.1 Extraction of Central Values

For example, consider the following image:

A                                                                    B



*Figure 23 (A) Example RGB image. (B) Luminance image based on (A) cropped to remove the reference ball in the lower left-hand corner.*

Evaluation of the local RMS contrast values $L(I,j)$ in Figure 23(B) using Equation 6 at a scale of m = 3 for the top left-hand corner gives:

ans = 7×7

| | | | | | | |
|---|---|---|---|---|---|---|
| 0.6423 | 0.6437 | 0.6441 | 0.6453 | 0.6468 | 0.6480 | 0.6491 |
| 0.6509 | **0.6522** | 0.6525 | 0.6537 | **0.6551** | 0.6563 | 0.6573 |
| 0.6606 | 0.6619 | 0.6622 | 0.6633 | 0.6647 | 0.6658 | 0.6669 |
| 0.6671 | 0.6684 | 0.6687 | 0.6696 | 0.6705 | 0.6713 | 0.6722 |
| 0.6693 | **0.6705** | 0.6706 | 0.6706 | **0.6710** | 0.6715 | 0.6724 |
| 0.6695 | 0.6706 | 0.6702 | 0.6702 | 0.6705 | 0.6710 | 0.6719 |
| 0.6684 | 0.6696 | 0.6693 | 0.6691 | 0.6693 | 0.6698 | 0.6706 |

*Table 5 Contrast values determined for the top left-hand corner of the luminance image in Figure 23(B).*

Each value shown is the local contrast for each pixel *(i,j)* in the array. In order to determine the central values of an array of cells of scale 3 x 3, I need to extract the values at (2,2), (2,5,) (2,8) etc, as highlighted in yellow. As such, starting with a pixel-based array $L(i,j)$ of overlapping contrast values we can determine a smaller cell-based array $B(p,q)$ of non-overlapping contrast values for each cell of width 3 x 3.

Having defined the local contrast for a scale of 3x3 pixels, we can then use a "for" loop to determine local contrast over a range of scale values set by m to generate a contrast heat map.

### 3.4 Algorithm for Calculating the Contrast Heat Map

Using a for loop, for each value of m,

- Start with the luminance image array $A(i,j)$
- Calculate the pixel-based local contrast array $L(I,j)$ using equation (6).
- Calculate the cell-based local contrast array $B(p,q)$ by extracting the values at the centre of each cell
- Calculate a histogram of the cell-based contrast values in the range 0-1
- Save the bin count values from the histogram as one row in a contrast map array. These bin count values describe the frequency distribution of the cell contrast values in the range 0-100%, for this value of scale set by m
- Iterate the process with for incremented values of m, in order to define an array or map of how the local contrast varies across the range of scale values.

The scale of the map is calibrated in degrees, based on the experimental set-up described in Chapter 2. For that experiment I used a display with a pixel spacing of 0.25 mm at a viewing distance of 800 mm, such that the subtended angle of each pixel was 0.016 degrees (allowing for the cosine error). I

therefore use the value of 0.016 degrees per pixel to set the scale in degrees for the images analysed here e.g., a 3x3 pixel array is equivalent to a subtended angle of 0.05 degrees, assuming that the test image was projected on a screen at 800mm and viewed at a peripheral angle of 23.5°.

This algorithm was used to calculate the contrast heat maps of images as viewed in peripheral vision. The scale range I used is 3-121 pixels, equivalent to 0.05°-2.0°, which is the range of interest for the M and P pathways evaluated in Chapter 2 and similar to relevant papers (Frazor & Geisler, 2006)

The first step was to test the algorithm with luminance images of sine waves of fixed contrast and spatial wavelength, to determine if the algorithm correctly modelled these known parameters.

### 3.5 Evaluation of the Contrast Heat Map Methodology

The reference image used for the initial evaluation of the is shown in Figure 24. It consists of a single sine wave (full image) with a wavelength of 0.34° and a Michelson contrast of 20%.
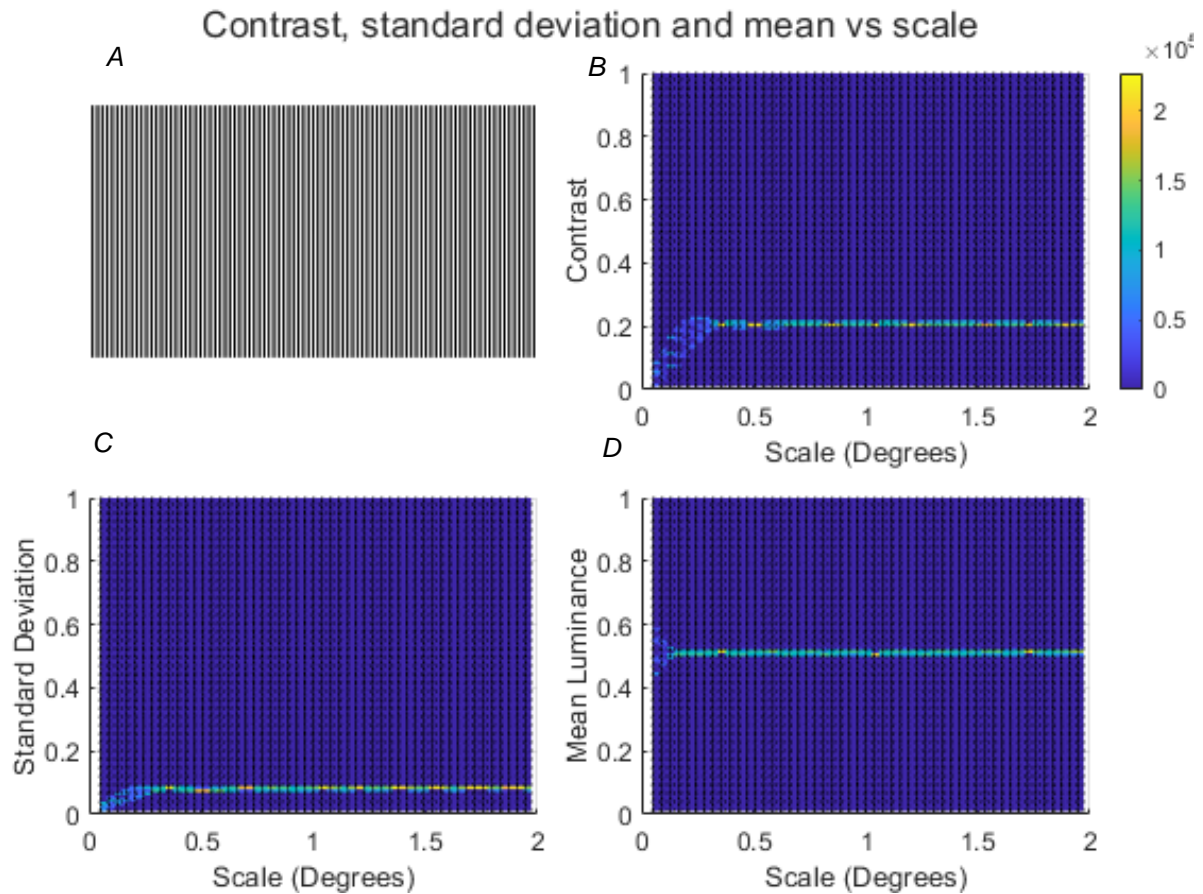


*Figure 24 (A) Full-image sine wave (wavelength = 21 pixels/0.34°) and 20% Michelson contrast. (B) Contrast versus scale, with the Z axis showing the bin count. (C) Standard deviation vs scale. (D) Mean luminance vs scale.*

Figure 24(B) shows the contrast map derived using Equation 6. There are several observations to be made:

a)  The known contrast of the sine wave (Michelson contrast = 20%) has been used to determine the constant $C_2$ in Equation 16. This value is used for $C_2 = 1,412$ in all subsequent modelling.

b)  The contrast value is constant at 20% from large scale (2°) down to a scale of 0.34° (the wavelength of the sine wave). Below this scale, the calculated contrast declines to zero at zero scale. This is not a defect in the algorithm but is a result of determining the standard deviation of a sine wave over a distance shorter than the wavelength. The standard deviation (and hence RMS contrast) tends to zero for zero sampling distance. Interestingly, this looks like a 1/f function if plotted as spatial frequency (1/scale) rather than scale. However, this is not a feature of the image statistics (as the image is a simple sine wave) but a feature of the algorithm (which is modelling the function of the RGC).

As such, for any image analysed for local contrast and presented as a contrast map in this form, there will always be a peak in low apparent contrast at low scale. However, as will be seen later, this low contrast/low scale signal is outside the sensitivity bands of the M and P pathways, and thus is not perceived.

c)  The contrast value is not precisely constant at 20% as al values of scale. There is a small variation which blurs the contrast value (approximately +-0.5%) periodically. This arises because the calculated value for the contrast is only independent of the phase of the sine wave when the sampling scale is a multiple of the wavelength. Intermediate values of scale have a small error in the contrast arising from the variable phase. This phase error can be minimised by, for example, dividing the sine wave image into four quadrature-shifted sine waves. However, for simplicity I have not done this, as natural images do not typically have fixed phase relationships across the image, so this effect should not be significant.

Figure 24(C) shows the standard deviation (Equation 14) as a function of scale. The structure in the contrast value is predominantly due the standard deviation term. Figure 24(D) shows the luminance as a function of scale. As with the standard deviation and contrast maps, there is a small periodic level of variation on the luminance value due to the same phase effect. One noticeable difference is that the mean luminance is constant down to a scale of 0.17° (half the sine wave wavelength), as only half a cycle of a sine wave is required to determine the mean value accurately.

At this point, the algorithm has generated a plausible contrast map for a single sine wave. The next figure shows the contrast map for a test image with four sine waves.
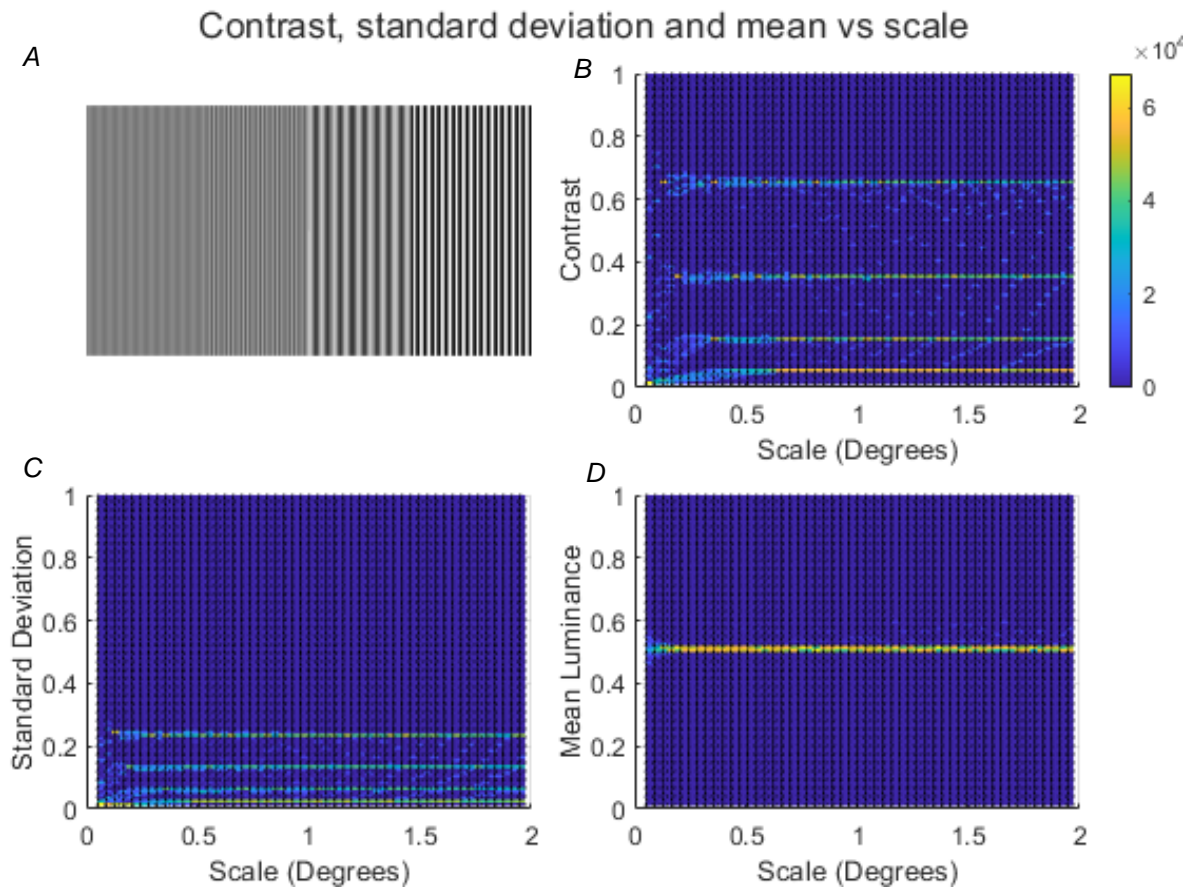
*Figure 25. (A) Four sine waves (wavelengths/contrast: 0.74/4.5%, 0.34/14.5%, 0.18/34.5%, 0.11/64.5%) (B) Contrast versus scale, with the z axis showing bin count. (C) Standard deviation vs scale. (D) Mean luminance vs scale.*

The four sine waves have the following wavelengths and contrast values:

      A. 45 pixels = 0.74° at 4.5% contrast

      B. 21 pixels = 0.39° at 14.5% contrast

      C. 11 pixels = 0.18° at 34.5% contrast

      D. 7 pixels = 0.11° at 64.5% contrast

For Figure 25(B) (contrast) the following observations can be made

   a) For each of the sine waves, the measured contrast values are close to the known value (with the addition of the phase effect discussed above).

   b) The point of inflection at low scale where the constant contrast value transitions to the low scale/low contrast function equates to the known wavelength of each sinewave, except for the longest wavelength sinewave (nominally 0.74°) which is low by about 10%.

   c) There are some faint diagonal lines between the lines of constant contrast. These arise from the boundaries between the four sine wave segments, such that cells that overlap a boundary see an intermediate value of the contrast values on either side of the boundary. As such, the

algorithm is correctly capturing the actual contrast variation as a function of local scale and position.

In conclusion, the algorithm is correctly mapping the local contrast for simple images composed of multiple sine waves. The next is to use the algorithm to evaluate natural images in terms of local contrast and scale, which is described in the next section.

**3.6 Analysis of Natural Images**

The images used for this analysis are from the "Barcelona Calibrated Images Database" (Vasquez-Corrall, 2009). The images were collected using a standard process with a grey reference sphere for illuminant recovery and were calibrated to give a set of standardised CIE1931 XYZ pixels, saved as MATLAB data files. The 350 images in the dataset were categorised as Urban Scenery, Forests and Motorways, Snow and Sea and Naturalistic. This meant that I was able to analyse both individual images and averages over multiple images, for several categories (Urban, Naturalistic (based on the Natural04 set), Beach and Forest).

For each image, the Y component was extracted as the luminance image array. The XYZ file was also converted to an RGB file for visualisation, although the RGB files were not used for any analysis. The next section shows some examples of the images and their contrast maps.

The first example is a beach scene with widely varying contrast profiles (Figure (24).



Fig 26. The top row shows the RGB (A) and luminance image (B). The middle row shows the cell-based contrast maps, with (C) showing the raw data and (D) having a small amount of Gaussian filtering applied to reduce the noise. The bottom row shows (E) the raw standard deviation data and (F) the mean luminance data.

Figures 26(A) and 26(B) are the RGB and luminance images, respectively, with the latter normalised to use the full gray scale. Figure 26(C) is the raw contrast data. For improved visualisation, I have a applied a low level of Gaussian filtering (σ = 0.1), to give the contrast map shown in Figure 26(D). There are two strong contrast features at 35% and 50% contrast, with a third, weaker feature at 20%. The inflection points at the critical wavelengths of around 0.3 and 0.4 degrees for the two higher contrast features. The higher contrast feature corresponds to the footprints in the sand in the centre of the image, with the mid contrast feature being the sea and lowest contrast the smooth area of the beach. The low contrast/low scale feature arising from the under-sampling peak is clearly visible.

Figure 26(E) shows the standard deviation map, mirroring the contrast map. Figure 26(F) shows the mean luminance map, with a strong low value structure which corresponds to the sea, with a more diffuse structure at a higher mean luminance value that corresponds to the middle strip of sand. Overall, the mean luminance is essentially primarily independent of scale down to 0.1°.

As another example, Figure 27 shows the contrast maps for an image of a forest scene.
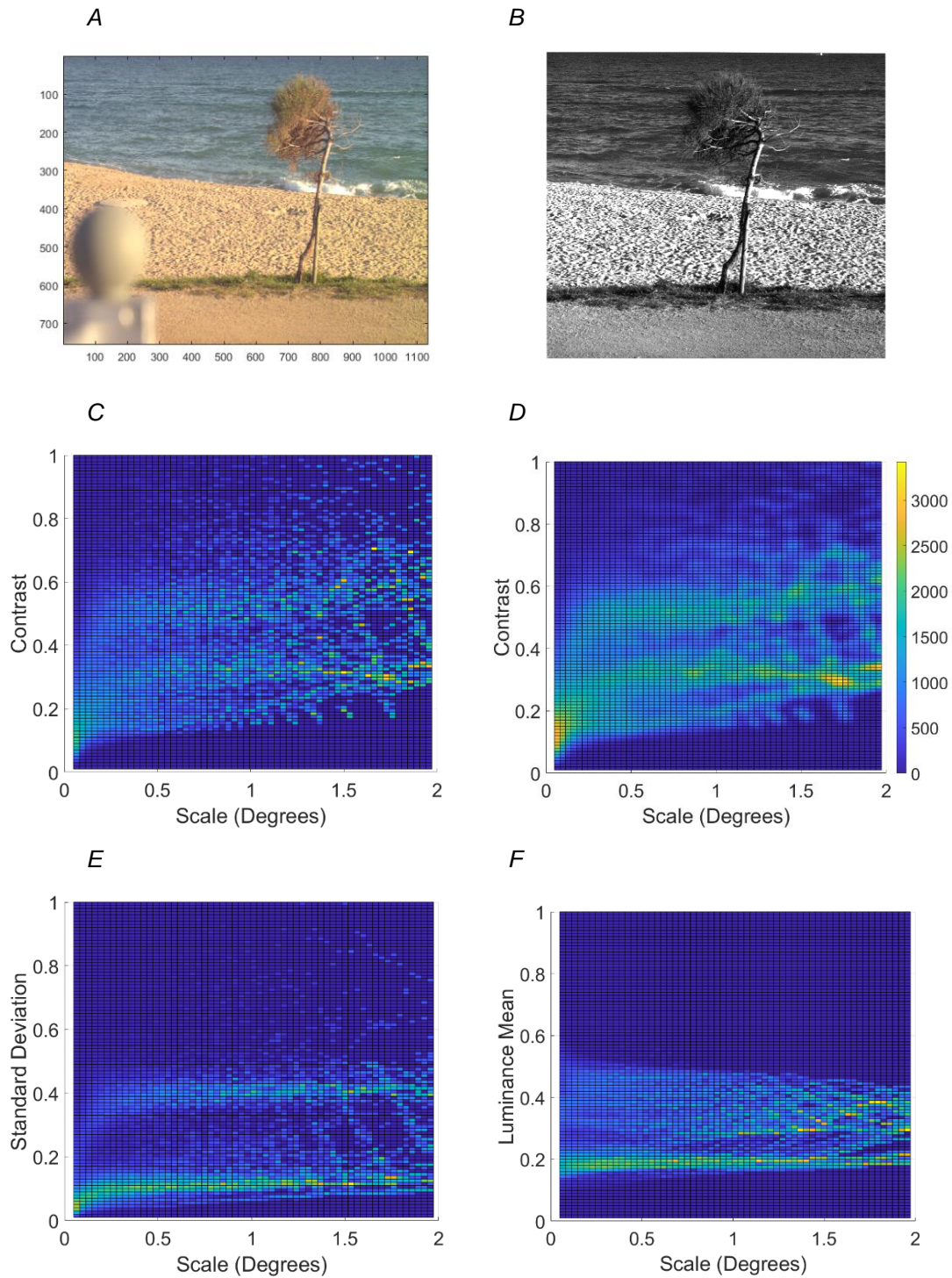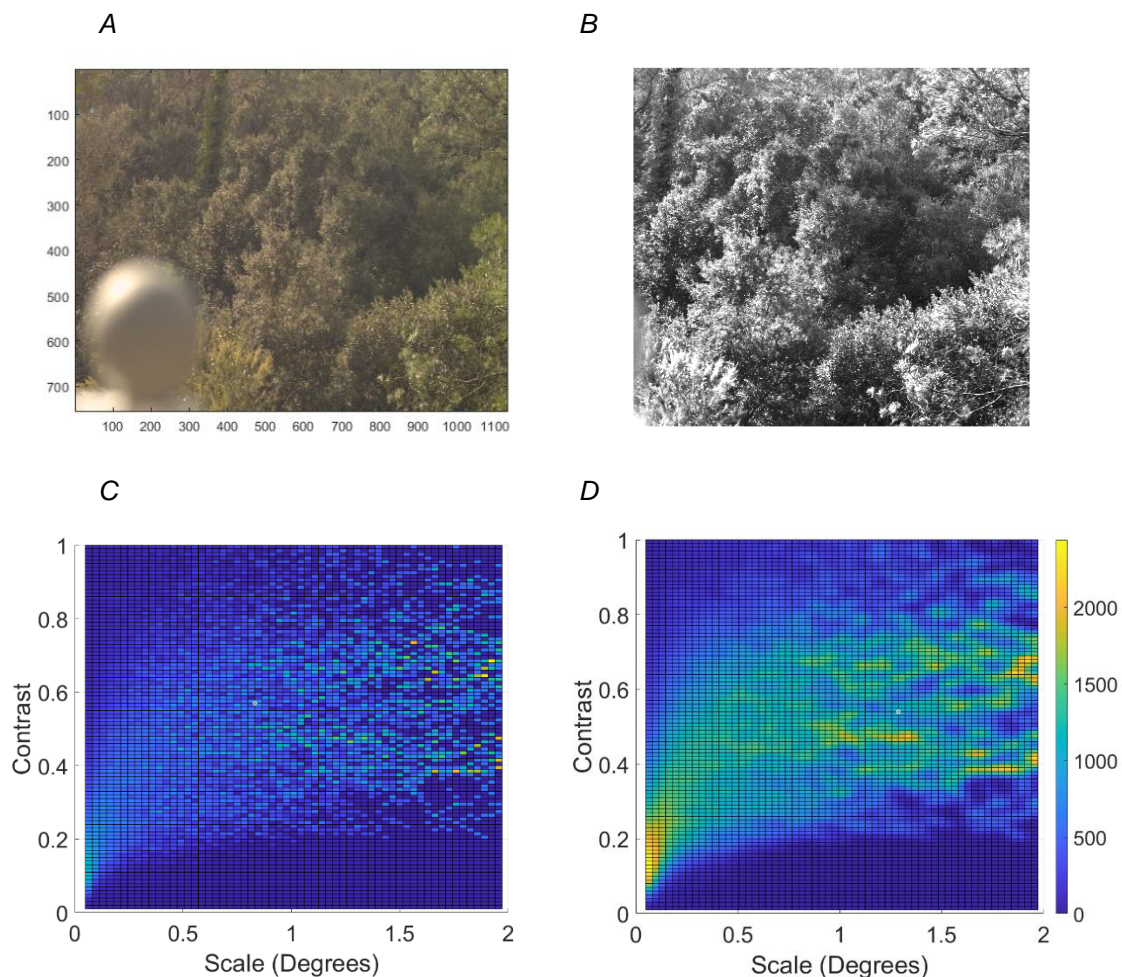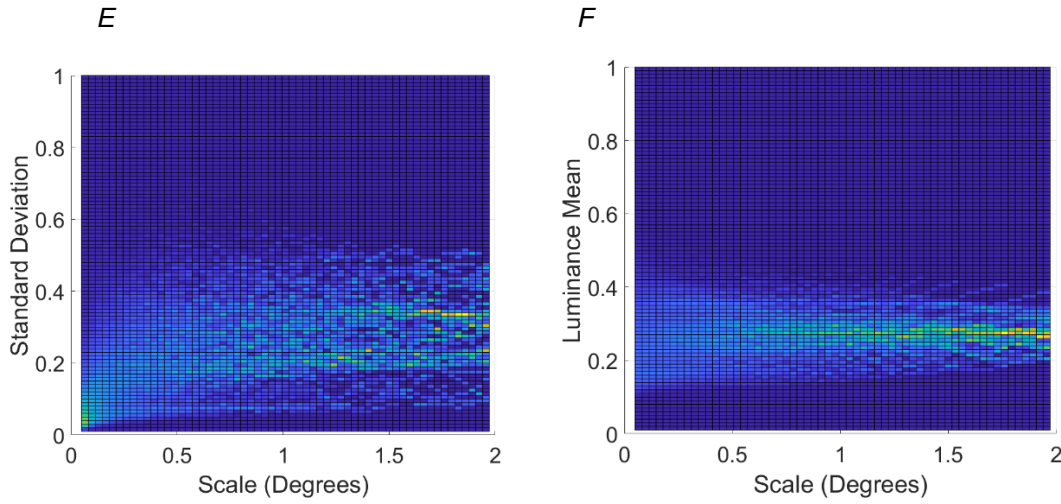
*Fig 27. The top row shows the RGB (A) and luminance image (B). The middle row shows the cell-based contrast maps, with (C) showing the raw data and (D) having a small amount of Gaussian filtering applied to reduce the noise. The bottom row shows (E) the raw standard deviation data and (F) the mean luminance data.*

The contrast map (Figure 27(D)) shows a broader, more diffuse variation of contrast, with some structure above 1°. The mean luminance has low structure and is essentially scale invariant down to 0.1°.

Considering the maps for both images, there are two main observations:

a) The mean luminance is essentially scale-invariant down to 0.1°.
b) The variation in the contrast map structure is therefore determined primarily by the standard deviation distribution, which in the two images discussed have features at large scale but which tend to the origin (low contrast/low scale) at low scale.

These two observations are consistent with the findings of Frazor and Geisler (Frazor & Geisler, 2006), who analysed local scale dependence of luminance and contrast in natural images, for a number of image segment categories, summarised in Figure 28.
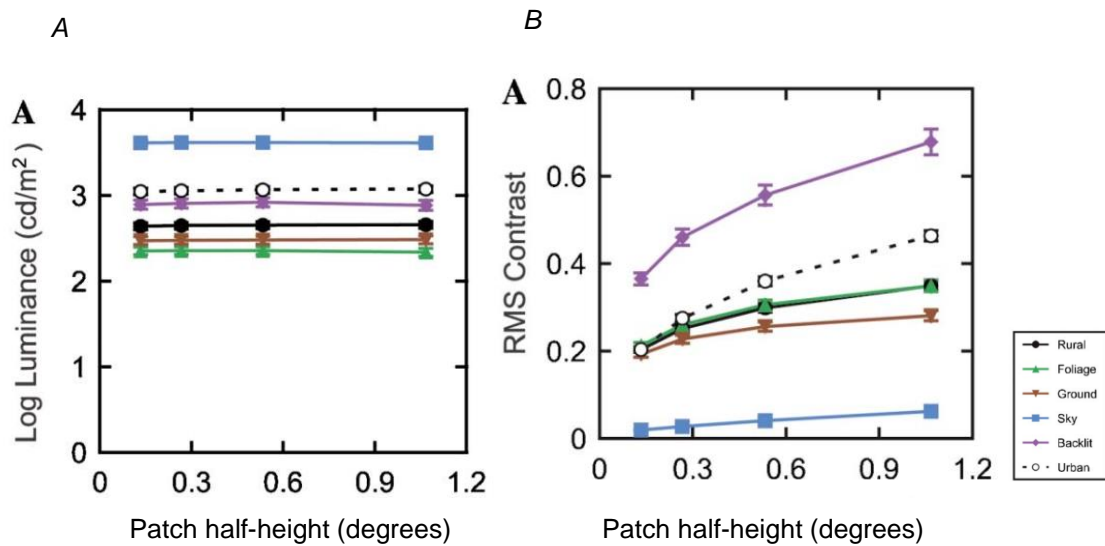
*Figure 28 (A) Luminance as a function of scale for segments of images categorised as Rural, Foliage, Ground, Sky, Backlit and Urban. (B) RMS variation as a function of scale for the same segments. Note that the x axis scale is patch radius in degrees. (Reproduced from Frazor & Geisler, 2006)*

The scale range is 0.3-2.0° (diameter), which is consistent with my model. The mean luminance values are essentially scale invariant over this range, with differing absolute values for each segment type. The RMS contrast values have the characteristic of having a small positive slope at large scale, with a point of inflexion in the diameter range of 0.5-1.0°. At low scale values, the contrast tends to zero. As such, the contrast maps generated by the algorithm are consistent with Frazor's results, albeit Frazor does not ascribe the shape of the contrast function to any underlying statistics, but refers to it a "monotonically increasing" (Frazor & Geisler, 2006)

Typically, the statistics of an image are characterised in the spatial frequency domain. Therefore, the data from Figure 27D (contrast versus scale) was re-plotted as contrast versus spatial frequency (defined as 1/scale) as shown in Figure 29 (in $\log_{10}$-$\log_{10}$ format).
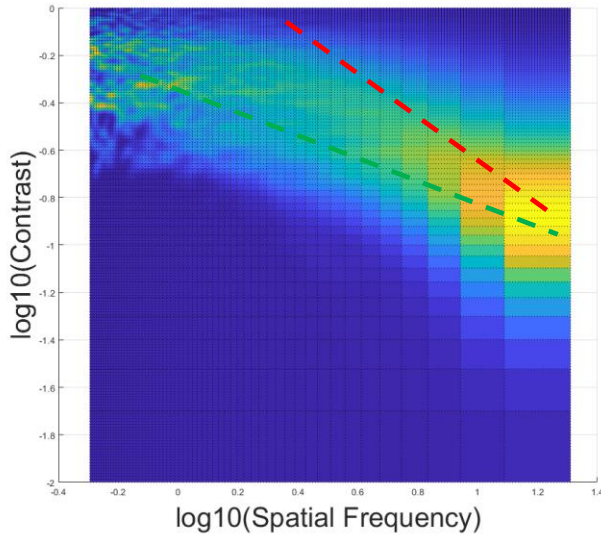
*Figure 29. Plot of Figure 27(D) as log10(Contrast) vs log10(spatial frequency). The red dashed line is a 1/f slope, and the green dashed line is a 1/f$^\alpha$ slope where α = 0.5.*

The red dashed line has a slope of 1/f, which is consistent with the slope determined for the sine wave images, and is what would be expected if the image contrast values were uncorrelated i.e. noise. However, as can be seen the data looks to be better estimated by a slope of 1/f$^\alpha$ where α = 0.5. Ruderman reports a value of α = 0.2 (Ruderman, 1994) for his specific image set, and Balboa reported values of α = 0.5 to 0.7 (estimated from (Balboa & Grzywacz, 2003). As such, the α values determined using the contrast algorithm model are consistent with these papers.

For completeness, Figure 30 shows average contrast maps for five random images from each of the four groups, together with an example image and contrast map for each group.
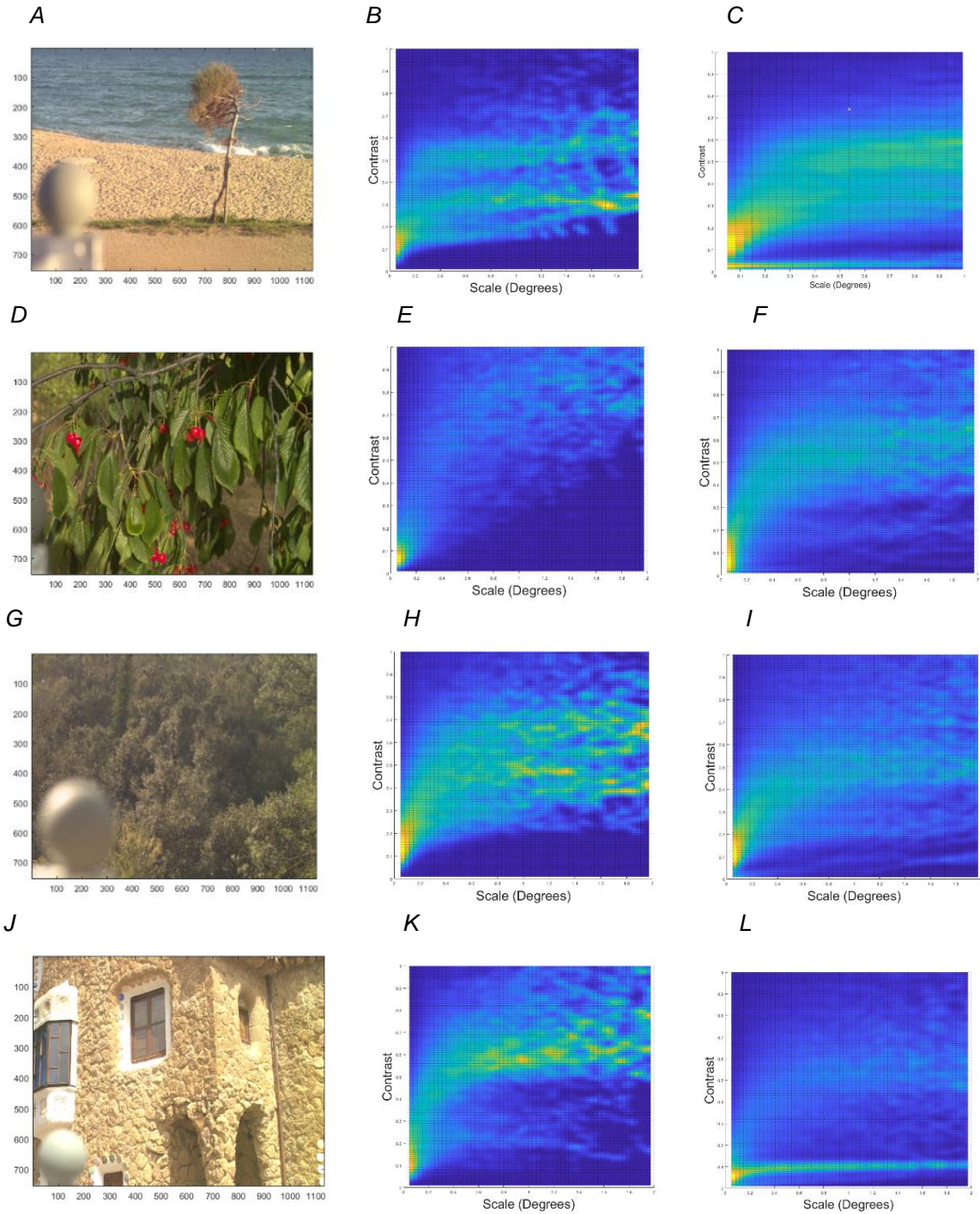
*Figure 30. Contrast maps for example images from each category, with each row showing an example RGB image from the group (Sand, Natural, Forest and Urban), the corresponding contrast vs scale plot, and the contrast vs scale plot averaged over 5 images from the group.*

Each of the contrast maps for the individual images are quite different, which is expected given their different object and texture distributions. However, overall, it can be seen can be seen that the average contrast maps have three dominant features:

a) A diffuse structure with a $1/f^{\alpha}$ scale dependence, arising from the underlying image statistics and the under-sampling characteristic of the contrast measurement.

b) Low-contrast (<10%) scale-invariant structures (<0.1degrees) e.g., sea, sky, concrete plazas

c) Medium contrast structures with scale dependence greater than 1.0°

Typically, each image is composed of a combination of these three components.


### 3.6.1 Conclusions from the Natural Image Analysis

At this point, I have demonstrated that the contrast map algorithm generates accurate maps for sine wave test images with defined parameters. Tests of the algorithm on a range of natural images have also shown it to be consistent with other studies. I therefore used the same algorithm to visualise the characteristic responses of the M and P pathways differentially respond to the local contrast variations in natural images.


### 3.7 Visualising the Differential Responses of the M and P Pathways

Application of the contrast map algorithm for visualisation of the M and P pathways uses the following steps:

a) Determine for each pathway what the cell-based contrast image looks like at the characteristic scale of that channel (calculated from the spatial frequency response).

b) Use the known contrast sensitivity (in terms of impulses/% contrast) of each pathway to determine the output for each cell (based on its local contrast).

c) Plot an image of the contrast response image ((which is the contrast response function of the model mechanism).

Note that these contrast response images are not representative of what would be perceived over the full eccentricity range corresponding to width of the image, which that would require a linearly increasing cell size across the window, with the relevant scale factor for each pathway. Instead, for simplicity I have used a fixed characteristic scale for the whole image. As such, these images represent is what the contrast response images would look like at the eccentricity of 23.5 degrees. However, the images still have value in showing us the differential response of the two pathways to natural images.


### 3.7.1 Determining the contrast images at the characteristic scale for each pathway

The starting points for the contrast images are the characteristic spatial frequency responses of the two pathways from the 16-parameter frequency Gaussian model (summarised in Table 3). Superimposing the frequency responses of the two pathways on to a contrast sensitivity map (plotting contrast sensitivity (defined as 1/contrast) versus spatial frequency (defined as 1/scale) shows the relative contribution of the two channels (Figure 31).
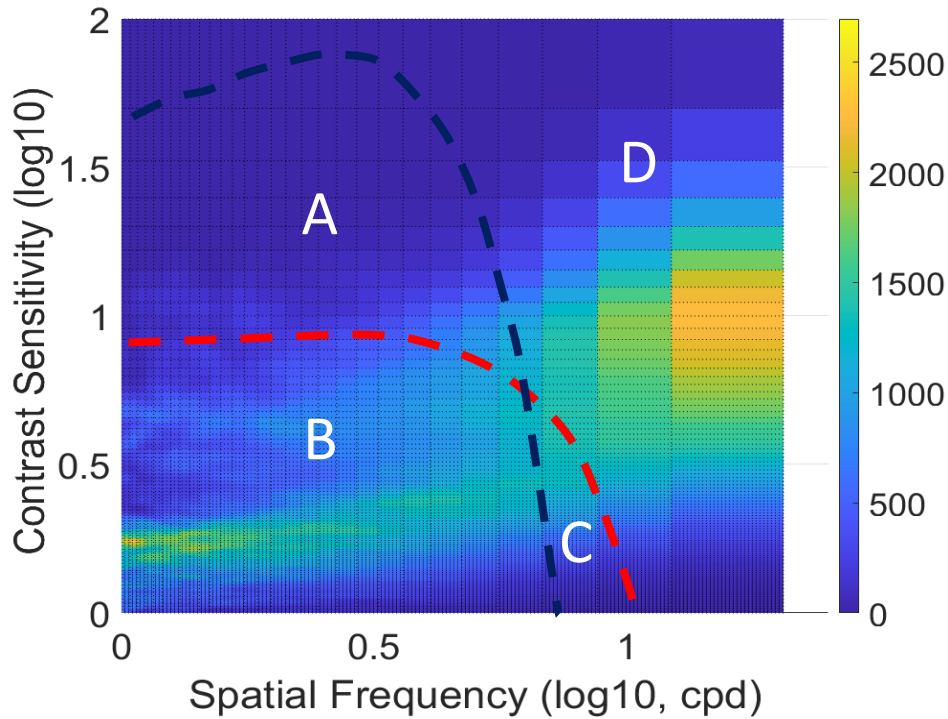


*Figure 31. Plot of Figure 30(K) as log10(1/contrast) vs log10(1/scale) overlaid with the contrast sensitivity functions for the M pathway (black dotted line) and P pathway (red dotted line) at 2Hz temporal modulation frequency.*

Figure 31 is the standard format for plotting the contrast sensitivity function. We can make a number of observations:

a) Both pathways see most of the contrast signal at low contrast/ low frequency. (Area B)
b) The differential M response is high contrast sensitivity/low spatial frequency (area A) and the differential P response is low contrast sensitivity high frequency (area C)
c) Neither pathway sees the low contrast/high frequency (low scale) signal that arises from the sub-sampling of the luminance (area D)

We can infer that the actual pathway responses are an efficient match to the available contrast information in the images, whilst minimising any response to the low contrast/high frequency signal arising from the under-sampling of low spatial frequency signals.

The next step is to build the contrast image based on the characteristic scale for each pathway.

### 3.7.2 Contrast images at the characteristic scale for each pathway

Using the same equation for local contrast (Equation 13) as used for the contrast maps (Section 3.4), I determined the contrast images for each pathway by setting the scale to the characteristic scale for each pathway (equal to the spatial DoG FWHM diameters derived from the characteristic frequency responses without MTF correction):

> M pathway: 0.16° equivalent to 10.0 pixels, rounded up to the nearest odd integer (11 pixels)
> P pathway: 0.10° equivalent to 6.1 pixels, rounded up to the nearest odd integer (7 pixels).

Note that the contrast data is held as the central value for each cell. In order to plot full sized images, the cell-based data needs to be padded such that, for a cell of size m x m, each pixel is assigned the central contrast value of that cell.

Figures 32(C) and 32(D) show the P pathway and M pathway contrast images, respectively, for an example image.

A
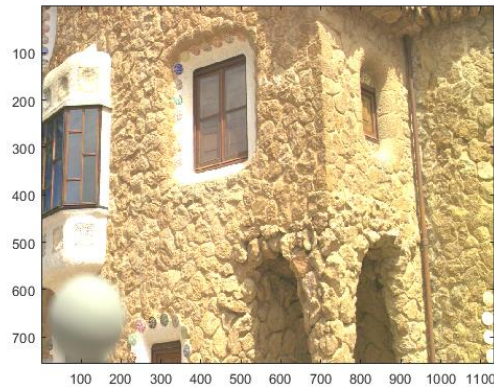


B



C



D



*Figure 32. (A) RGB image. (B) Luminance image. (C) P contrast image (0.10 °characteristic scale). (D) M pathway contrast image (0.16° characteristic scale).*

The following can be observed:

    a) The underlying structure of the square, non-overlapping cells.

    b) Both images show a level of edge enhancement, as we would expect for contrast images (Johnson (1994).

However, these images are based only on the spatial characteristics of the RGCs in the pathways. The next step is to determine the differential effect of the respective contrast gain responses of the two pathways.

**3.7.3 Modelling the Contrast Response Image for Each Pathway**

The contrast gain function for the M and P pathways were specified in Section 1.3.2.1 (Equation 2). Using the relevant equation for each pathway, the nominal output (impulses per second) for each cell in the contrast image is calculated based on its contrast value and the relevant threshold value. The resultant contrast response images are shown as greyscale images in Figure 31 for four example of luminance images from the Sand, Natural, Forest and Urban image sets.

| | A – Luminance Images | B – P pathway contrast image | C – M pathway contrast image | D – P pathway contrast response | E – M pathway contrast response |

72
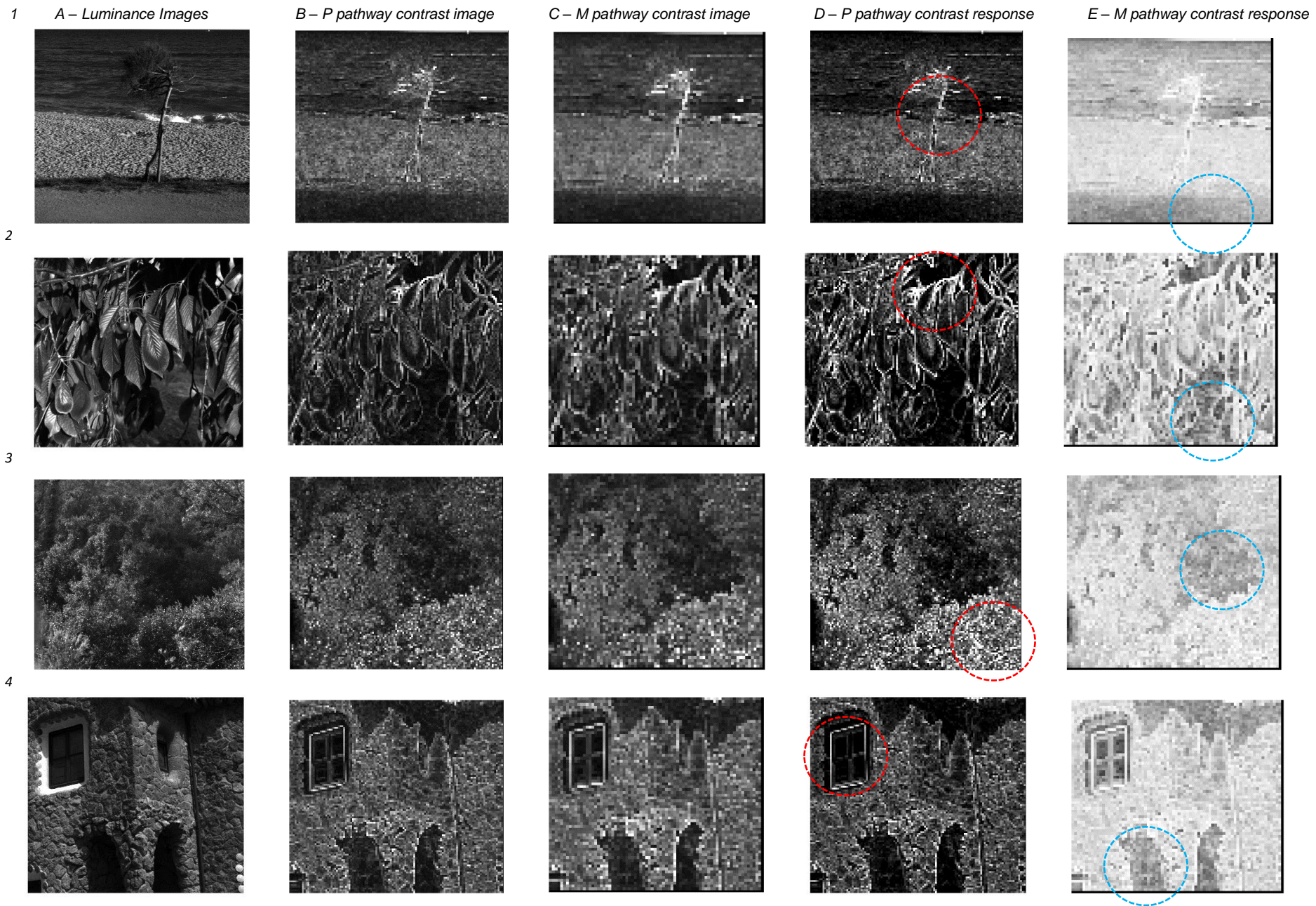
*Figure 33. Luminance, contrast image, and contrast response image for five different images. Column (A) are luminance images. Column (B) are P pathway contrast images. Column (C) are M pathway contrast images. Column (D) are P pathway contrast response images. Column (E) are M pathway contrast response images. The red dashed circles highlight regions of edge enhancement.*

Visual inspection of the contrast response images in column (D) suggests that a key characteristic of the P pathway is edge enhancement, determined by the linear contrast response function, and by the relatively high contrast threshold (11%). It appears to be an efficient edge enhancement process, as it extracts the edges of the window in Figure 31 (row 4 column A) despite the strong shadow. Note that the "break" in the edge on the RHS of the window and the stripes on the top and bottom are artefacts from using non-overlapping square cells, combined with the window edges not being parallel to the cell axes. Allowing some overlap of the cells and an irregular array would minimise these artefacts. This edge enhancement can be seen in all the P pathway images, with examples highlighted by red dashed circles, albeit less dramatically due to the lack of sharp edges in these natural images.

The M pathway has a key characteristic of contrast enhancement at low contrasts (determined by the non-linear contrast response and low threshold), enhancing the detail in the shadows inside the room and the archways of Figure 33 (row 4 column D)). Similar examples in the other images are highlighted with blue dashed circles.

.

Overall, the visualisation can be interpreted as indicating that the P and M pathways perform different filter functions of edge enhancement and contrast enhancement, respectively.

### 3.7.4 How efficient is the P pathway for Edge Enhancement?

We can visually compare the edge enhancement of the P pathway contrast response image with the standard Sobel and Canny edge detection algorithms in MATLAB. Figures 34(A) and 34(B) show the Sobel and Canny edge enhancement detection algorithms, respectively, applied to the luminance image of Figure 33(D). Figure 34(C) shows the equivalent P pathway contrast response function, with a two-level quantisation of the cell values (with a 50% threshold).
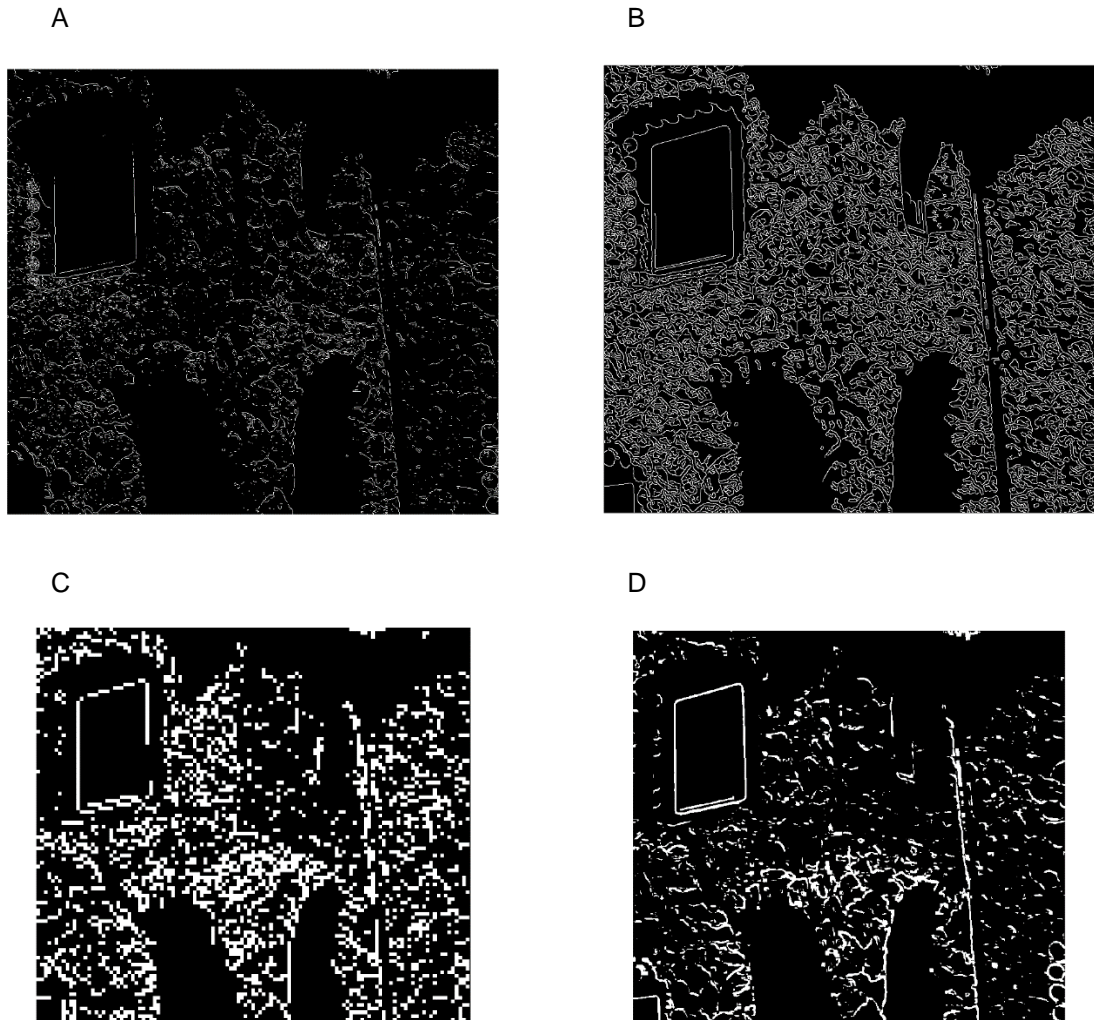
A                                        B



C                                        D



*Figure 34. (A) Application of Sobel filter (pixel based).  (B) Application of Canny filter (pixel based). (C) Cell-based P pathway based on Figure 33(4 D) with a 50% threshold applied. (D) Pixel-based P pathway (also with 50% thresholds applied).*

Visual inspection suggests that the cell-based P pathway edge enhancement process is more efficient than the Sobel in enhancing the edge in deep shadow, given that al the edges of the window in the top left had corner are recovered. However, further analysis would be required to formally quantify the relative efficiency of the two algorithms.  For completeness I have also shown a pixel-based version of the P pathway filter, which does not have the "square array" artefacts of the basic cell-based model..

Overall, both the cell-based and pixel-based P pathway responses are efficient edge-enhancement filters relative to the standard Sobel filter.

### 3.8 Conclusions

A simple algorithm for has been demonstrated for determining local contrast as a function of scale in natural images, allowing the derivation of contrast maps. The algorithm was validated using simple sine wave images and the results on natural images were consistent with previous studies, confirming scale invariance for the mean luminance values (<0.1 degrees) and a $1/f^{\alpha}$ type contrast variation arising from both the underlying image statistics and a $1/f$ dependence from the under sampling of the contrast measurement process.

Having confirmed that the algorithm correctly maps local contrast, I then used the same algorithm to plot contrast images at the characteristic scales of the M and P pathways, which allowed visualisation of the spatial contrast responses of two pathways at an eccentricity of 23.5 degrees. Visual inspection suggested that both pathways have an edge-enhancement characteristic arising from the contrast measurement (Johnson, 1990).

I subsequently compared the contrast images of the two pathways by applying the known contrast gain functions (impulses/second as a function of contrast) to determine a contrast response image, which effectively visualised the RGC activity level across the image. The visualisation can be interpreted as indicating that the two pathways perform different filter functions:

> P pathway: Edge enhancement
> M pathway: Contrast enhancement at low contrast levels

These results are similar to previous analysis of M and P filters ((Lourens, 1995) but that study considered foveal images and physiological rather than psychophysics data.

From a perceptual perspective, given the known edge-detection functions present in V1 and higher (), it could be argued that the peripheral P pathway is effectively pre-processing for these later stages. The M pathway contrast enhancement could be argued to aid peripheral detection of potential targets for attention, such as predators in shadows.

Finally, I compared the P pathway edge enhancement performance (with two level quantisation) to standard Sobel and Canny edge filters. The results suggested that the P pathway performed better than the Sobel filter for edge detection, especially in the pixel-based implementation of the P pathway filter.

**Chapter 4 Discussion and Conclusions**

**4.1 Discussion**

The primary aim of the project was to demonstrate direct psychophysical discrimination of the spatial and temporal characteristics of the retinal magnocellular and parvocellular pathways using stimuli tailored to the underlying physiology of the retinal ganglion cells (Kaplan et al., 1990; J.J. Kulikowski, 1987).

The secondary aim of the project was to use the measured characteristics of the two pathways to visualise the differential visual signals transmitted from the retina via the RGCs to the LGN, and higher visual levels. The visualisation required developing a contrast mapping algorithm that determines local image contrast of natural images as a function of scale and position in the image.

The measured peripheral contrast sensitivity functions for all participants at most temporal frequencies exhibited a dual-segment structure that was indicative of two individual pathways and was consistent with the "winner takes all" model (Kaplan et al., 1990). Initial model fitting showed that a common model based on a frequency Gaussian function (non-zero peak frequency) was the most parsimonious description for each individual data set. This finding suggested that there was a single underlying model that could describe the combined data set of all the participants, which proved to be the case. The most parsimonious model for the combined data set was also a frequency Gaussian function. The combined model required 11 parameters to fit the data of the first participant, with only two more parameters required for each additional participant. The model showed that the peak contrast sensitivity values were common for each participant, and that the spatial frequency cut-offs were also related, scaled by a simple multiplicative constant for each pathway.

Having determined the best fit for the spatial frequency responses of the M and P pathways, the equivalent spatial structures for each of the pathways could be derived. Comparison with published data for RGC dendritic field and receptive field data showed that the experimental values were consistent with those data. However, evaluation of the temporal CSF derived from the peak contrast sensitivity values at each temporal frequency did not conclusively support the discrimination of the two pathways.

As such, based on the contrast sensitivity, spatial and temporal characteristics derived from the parameters of the combined model, I concluded that the dual segment structure of the measured contrast sensitivity function could be attributed to the individual P and M pathways as hypothesised by Kaplan and Kulikowski (Kaplan et al., 1990; J.J. Kulikowski, 1987). The experimental evidence is also consistent with the hypothesis that the visual system uses a "winner-takes all" model when combining the input of the two pathways (Kaplan et al., 1990). This is a novel result for a psychophysical experiment using simple spatially and temporally varying stimuli.

Having shown that the peripheral contrast sensitivity function can be interpreted as deriving from the two discrete M and P pathways, I was curious to understand how those two pathways differentially transmit information from the retina to the LGN, SC and the higher visual cortex. In particular, I was interested in representing this differential behaviour using natural images, in order to visualise it.

While there is a large body of research on the statistic of natural images (Ghodrati et al., 2016; Peli, 1990; Ruderman, 1994; Scholte et al., 2009), most of the studies are concerned with population statistics for whole images or groups of images, rather than within images as a function of local scale. In addition, the majority of published data is for luminance statistics rather than contrast (e.g. (To, Lovell, Troscianko, & Tolhurst, 2010)). Therefore, to implement a visualisation methodology, I needed an algorithm for determining contrast as a function of local scale whilst retaining position information. This would enable the creation of contrast-based images of each of the images, from which I could create contrast response images by applying the relevant contrast gain functions of the M and P pathways to plot contrast response images at threshold (assuming that the suprathreshold were equivalent to the threshold characteristics).

I developed a simple model based on RMS contrast to generate contrast maps over a scale range of 0.05°-2°. I evaluated the model using sinusoidal images of fixed wavelength and contrast and showed that the contrast map algorithm recovered the correct values for those two parameters.

Application of the model to calibrated natural images gave results that were consistent with published data, namely the mean luminance being essentially scale invariant over the scale range, and the contrast having a $1/f^\alpha$ type dependence, with an inflexion point at about 1.0° (Frazor & Geisler, 2006).

Having established that the contrast map algorithm gave results consistent with previous studies, I then used the same model to generate contrast response functions at the characteristic scale of the peripheral P and M pathways (at 23.5°). The contrast response functions suggested that the peripheral P pathway characteristic is that of edge-enhancement (which is a feature of contrast measurement (Johnson, 1990)) and that of the M pathway was enhancement of low-contrast information. The edge enhancement of the P pathway was effective, in that it accurately extracted edges in the presence of harsh shadows. Visual comparison with standard Sobel and Canny filters indicated that the P pathway response was at least equivalent to the Sobel filter.

In summary, the results presented in this dissertation suggest that psychophysical discrimination of the M and P pathways in peripheral vision is possible using simple spatially and temporally varying stimuli. I have also demonstrated a visualization methodology that suggests that the function of achromatic P pathway in peripheral vision is edge enhancement, and that of the M pathway is contrast enhancement.

**4.2 Other observations and questions**

One of the key characteristics of the visual system is the dramatic data compression that takes place between the photoreceptors that generate information at approximately 100 MB/s and the higher levels of the visual cortex where the bit rate is only 0.1 MB/s (Zhaoping, 2018). Given the edge and contrast enhancement characteristics of the two pathways, if the P signals were thresholded to give a binary response, and if the M signals were clipped at high output impulse rates, the data compression for peripheral information would be significant for both channels. As such, the contrast images algorithm provides a potential explanation for how data compression naturally arises in the periphery.

I note that the information transmitted by the peripheral RGCs is contrast and not luminance i.e., the LGN and higher visual areas only receive contrast information. The luminance contribution is removed by the various adaptation processes in the eye, and unless the adaptation parameters are transmitted separately, the luminance information loss would seem to be irrecoverable.

The visual system exhibits a number of constancies, including colour, luminance and size (Hatfield & Allred, 2012). A key characteristic of the stimuli used in this study was the linearly varying fringe spacing as a function of eccentricity, which matches the underlying physiology of the RGC arrays. The linear dependence of the spacing means that the resolution of a fixated image on the retina in terms of the number of RGCs sampling it is constant as the object moves further away. This arises because the edges of the image fall nearer the fovea, so although the image gets smaller, the linear density of the RGCs increases, thus keeping the number of RGCs constant. This may contribute to size constancy.

The observed 'winner takes all' response described above relates to the visual system responding to the most sensitive of two achromatic pathways. However, a similar characteristic has been demonstrated for combined achromatic/chromatic images, where the visual system responds most strongly to a high-resolution achromatic signal, such that luminance edges in an image are perceived to enhance the apparent resolution of low-resolution chrominance stimulus (Jennings & Kingdom, 2017). This effect is known as the "watercolour" effect (Pinna, 2005) and is illustrated in Figure 35.
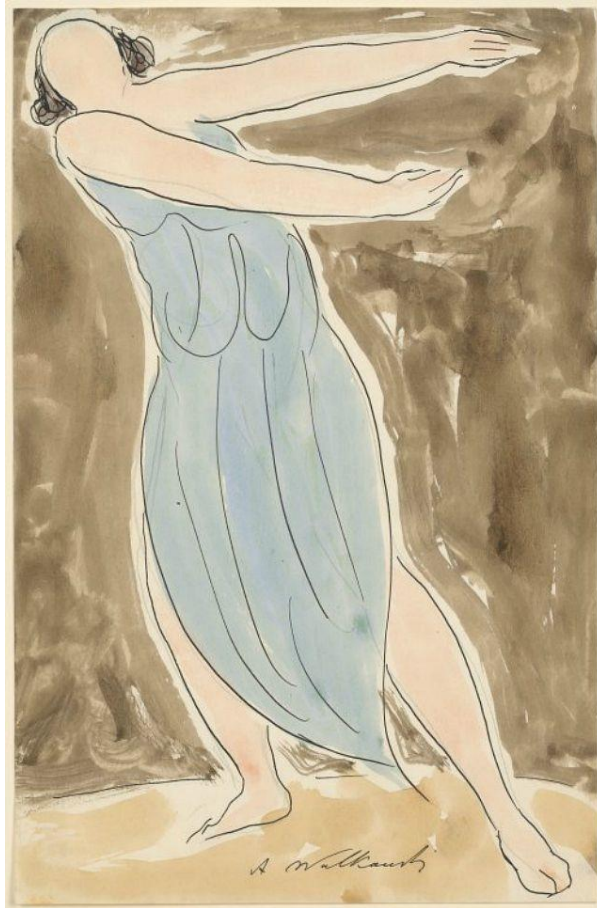
*Figure 35. Image of watercolour painting by Abraham Walkowitz.*

The water colour effect is the perception that the low-resolution chromatic areas appear to follow the high-contrast black lines, even though close inspection shows that the boundaries of the paint are detached from the lines. It could be argued that the "winner takes all" characteristic provides some perceptual enhancement when only low-resolution information is available, and therefore partially compensates for the data compression described above.

Although the results described in this dissertation have been modelled in terms of the low-level characteristics of the RGCs (contrast gain, spatial dimensions), the psychophysics paradigm necessarily involves high-level functions, including use of working memory, decision making and motor control. However, based on the earlier discussion relating critical scale factor of a visual process to identification of the level in the visual cortex where the process is executed, the low scale factor measured ($S = 0.0075$) places the key process in this instance at the level of the RGCs (or LGN). That said, the actions required of the participants are simple and repetitive and are therefore likely to be constant for each stimulus at the higher levels of the visual, cognitive and motor areas. The likeliest higher level visual area to be involved is V1 (scale factor = 0.15), where edge detection would be a key function in the detection task. However, the fact that the measured scale factor is

significantly lower suggests that the detection task has a constant response independent of the detail of the stimuli at V1 as well.

**4.3 Limitations**

The experimental design used stimuli with spatial frequencies in the range of 1-20 cpd, which was a pragmatic choice in order to maximise the resolution on the high frequency side of the CSF. This did however mean that there was no low frequency data for the contrast sensitivity functions, such that a DoG model could not be fitted directly to the experimental data. However, extension of the spatial frequency range below 0.3 cpd (given the 5.5° horizontal stimulus width) would introduce a luminance artefact for this particular setup.

Linearly varying fringe spacing stimuli were used to match to the underlying spatial structure of the RGCs, on the assumption that this would give a more sensitive measure of the PSE threshold, as all the RGCs within the stimulus window would reach threshold at the same time. However, while this was a plausible assumption, I did not directly compare the performance with these stimuli against convention Gabor patch stimuli with fixed wavelengths and this probably merits further investigation.

In determining the spatial dimensions of the M and P RGCs inferred from fitting the model parameters to a DoG, I used representative data for the MTF of the human eye for off-axis imaging. The correction was significant for both M and P 60% ie calculated P spatial DoG with MTF correction vs no MTF correction was 0.10° vs 0.16° respectively. As such, there was potential for a systematic error if the correction applied was not the best fit for the participants individual responses. Best practice would be to measure the off-axis MTF functions of each participant to avoid this potential source of systematic error.

The modelling of the contrast maps used the "stdfilt" function in MATLAB that determined the standard deviation over an m x m array of pixels. As such, the sampled array was square as opposed to a more physically realistic circular sample shape. (Note that this does not apply to the imgauss function as this applies a Gaussian envelope to the sample). It would therefore have been more realistic if a new function had been written which sampled a circular array of pixels, or a similar weighted distribution. However, the image statistics obtained using the algorithm were consistent with published data, supporting this use of "stdfilt".

With regards to the contrast maps and contrast response functions, the model cell array was a regular structure with cubic symmetry. A more realistic approach would have been to use a random array, potentially with a degree of overlap of the cells. A further improvement would be to make contrast maps and contrast response functions with a linearly increasing spacing (scale factor) of the cells, such that the visualisation would be more realistic in covering a range of eccentricities, rather than

being the representation at the single eccentricity (23.5 degrees). However, the choices made were pragmatic to keep the project tractable in the time available.

**4,4 Future Research**

The experiment was conducted using tangential gratings in a detection task. This enabled the identification of the M and P pathways by direct comparison of the measured spatial DoGs with published physiological data. This is a novel result, and it would be valuable to cross-check the result using a different paradigm. A future study could achieve this by switching to a resolution task using both the tangential fringe set and a radial fringe set (which is orthogonal to the tangential gratings). The radial gratings can be designed with an equivalent scale factor (for the angular spacing of the gratings) to match the assumed underlying distribution of the RGC arrays. The use of a resolution task would probe the RGC array spacing rather than the DoG structure of the individual RGCs, as the Nyquist frequency is independent of contrast. This would allow direct determination of the underlying array spacing which could be compared with published visual acuity studies (Wilkinson et al., 2016), and hence support the identification of the two pathways.

An exciting potential clinical application of this work relates to how peripheral vison plays an important role in day-to-day living for patients with macular degeneration and other forms of low vision. In these conditions, the fovea is damaged so that central vision is significantly impaired. In such circumstances, the patients make best use of parafoveal and peripheral vison to manage their daily tasks. A typical practical aid is the use of large fonts for magazines, books etc, attempting to offset reduced resolution with larger objects. However, this can be self-defeating if the individual image elements occupy too large a part of the remaining working retina. A more interesting idea is to utilise the edge-enhancement functionality of peripheral vision together with the "winner takes all" response of the visual system. The latter is relevant to red suits in playing cards (and large areas of chromatic information in images) as the loss of foveal cones particularly impacts colour vision. If we can emphasise the luminance edges of objects, this should preferentially stimulate the P pathway for achromatic information and potentially improve chromatic vision via the 'water colour' effect. The necessary image processing could be simply done using existing smart phone functionality for physical objects such as books or playing cards or built into streaming video services.

## 4.5 Final Conclusions

Direct psychophysical discrimination of the spatial and temporal characteristics of the retinal magnocellular and parvocellular pathways in the primate visual system has proved elusive. However, the results of the experiment reported here suggest that such discrimination is possible using stimuli tailored to the underlying physiology of the M and P retinal ganglion cells.  To maximise the sensitivity, the visual stimuli used were tangential sinusoidal gratings with a linearly varying spacing matched to the retinal ganglion cell spacing.  The results support the hypothesised dual-segment characteristic of the contrast sensitivity function and are consistent with the known contrast gain and spatial physiological characteristics of the P and M pathways in the primate visual system. The results are consistent with previous observations that the overall system response is that of the most sensitive of the two channels at a given contrast, rather than summing the two channel responses.

In order to visualise how the two pathways transmit visual information to the LGN and the higher visual areas, I developed a simple algorithm for determining local contrast as a function of scale in natural images, allowing the derivation of contrast heat maps. The algorithm was validated using simple sine wave images and the results on natural images were consistent with previous studies.  I then used the same algorithm to plot contrast response functions at the characteristic scales of the M and P pathways, which allowed visualisation of the spatial contrast responses of two pathways at an eccentricity of 23.5 degrees. The visualisation can be interpreted as indicating that the P and M pathways perform different filter functions of edge enhancement and contrast enhancement, respectively.

# References

Anderson, R. S., Zlatkova, M. B., & Demirel, S. (2002). What limits detection and resolution of short-wavelength sinusoidal gratings across the retina? *Vision Research, 42*(8), 981-990. doi:10.1016/s0042-6989(02)00013-5

Balboa, R. M., & Grzywacz, N. M. (2003). Power spectra and distribution of contrasts of natural images from different habitats. *Vision Research, 43*(24), 2527-2537. doi:10.1016/s0042-6989(03)00471-1

Bringmann, A., Syrbe, S., Gorner, K., Kacza, J., Francke, M., Wiedemann, P., & Reichenbach, A. (2018). The primate fovea: Structure, function and development. *Progress in Retinal and Eye Research, 66*, 49-84. doi:10.1016/j.preteyeres.2018.03.006

Burns, M., & Pugh, E. (2014). Visual Transduction By Rod and Cone Receptors. In J. Werner & L. Chalupa (Eds.), *The New Visual Neurosciences* (Vol. 1, pp. 7-18). Cambridge, Massachusetts, USA: The MIT Press.

Campbell, F. W., & Green, D. G. (1965). Optical and Retinal Factors Affecting Visual Resolution. *Journal of Physiology-London, 181*(3), 576-+. doi:10.1113/jphysiol.1965.sp007784

Campbell, F. W., Kulikowski, J. J., & Levinson, J. (1966). The effect of orientation on the visual resolution of gratings. *J Physiol, 187*(2), 427-436. doi:10.1113/jphysiol.1966.sp008100

Cao, D. (2013). Chapter 10 - Color Vision and Night Vision. In S. J. Ryan, S. R. Sadda, D. R. Hinton, A. P. Schachat, C. P. Wilkinson, & P. Wiedemann (Eds.), *Retina (Fifth Edition)* (pp. 285-299). London: W.B. Saunders.

Cao, X. W., Merwine, D. K., & Grzywacz, N. M. (2011). Dependence of the retinal Ganglion cell's responses on local textures of natural scenes. *Journal of Vision, 11*(6). doi:10.1167/11.6.11

Cope, D., Blakeslee, B., & McCourt, M. E. (2013). Analysis of multidimensional difference-of-Gaussians filters in terms of directly observable parameters. *Journal of the Optical Society of America a-Optics Image Science and Vision, 30*(5), 1002-1012. doi:10.1364/josaa.30.001002

Croner, L. J., & Kaplan, E. (1995). Receptive Fields of P-Ganglion and M-Ganglion Cells Across the Primate Retina *Vision Research, 35*(1), 7-24. doi:10.1016/0042-6989(94)e0066-t

Curcio, C. A., & Allen, K. A. (1990). Topography of Ganglion Cells in Human Retina. *Journal of Comparative Neurology, 300*(1), 5-25. doi:10.1002/cne.903000103

Dacey, D. M. (1993). The Mosaic of Midget Ganglion Cells in the Human Retina. *Journal of Neuroscience, 13*(12), 5334-5355. doi:10.1523/jneurosci.13-12-05334.1993

Dacey, D. M., & Petersen, M. R. (1992).Dendritic Field Size and Morphology of Midget and Parasol Ganglion cells in the Human Retina. *Proceedings of the National Academy of Sciences of the United States of America, 89*(20), 9666-9670. doi:10.1073/pnas.89.20.9666

De Valois, K. K. (1988). *Spatial vision*. New York ; Oxford: Oxford University Press.

Devalois, R. L., Morgan, H., & Snodderly, D. M. (1974). Psychophysical Studies of Monkey Vision. 3. Spatial Luminance Contrast Sensitivity Tests of Macaque and Human Observers. *Vision Research, 14*(1), 75-81. doi:10.1016/0042-6989(74)90118-7

Drasdo, N., Millican, C. L., Katholl, C. R., & Curcio, C. A. (2007). The length of Henle fibers in the human retina and a model of ganglion receptive field density in the visual field. *Vision Research, 47*(22), 2901-2911. doi:10.1016/j.visres.2007.01.007

Edwards, M., Goodhew, S. C., & Badcock, D. R. Using perceptual tasks to selectively measure magnocellular and parvocellular performance: Rationale and a user's guide. *Psychonomic Bulletin & Review*. doi:10.3758/s13423-020-01874-w

Edwards, M., Goodhew, S. C., & Badcock, D. R. (2021). Using perceptual tasks to selectively measure magnocellular and parvocellular performance: Rationale and a user's guide. *Psychonomic Bulletin & Review, 28*(4), 1029-1050. doi:10.3758/s13423-020-01874-w

Enroth-Cugell, C., & Robson, J. G. (1966). The contrast sensitivity of retinal ganglion cells of the cat. *J Physiol, 187*(3), 517-552. doi:10.1113/jphysiol.1966.sp008107

Evans, B. J. W., Drasdo, N., & Richards, I. L. (1994). An Investigation of Some Sensory and Refractive Visual Factors in Dyslexia. *Vision Research, 34*(14), 1913-1926. doi:10.1016/0042-6989(94)90315-8

Field, D. J. (1987). Relations Between the Statistics of Natural Images and the Response Properties of Cortical Cells. *Journal of the Optical Society of America a-Optics Image Science and Vision, 4*(12), 2379-2394. doi:10.1364/josaa.4.002379

Frazor, R. A., & Geisler, W. S. (2006). Local luminance and contrast in natural images. *Vision Research, 46*(10), 1585-1598. doi:10.1016/j.visres.2005.06.038

Freeman, J., & Simoncelli, E. P. (2011). Metamers of the ventral stream. *Nature Neuroscience, 14*(9), 1195-U1130. doi:10.1038/nn.2889

Freeman, J., Ziemba, C. M., Heeger, D. J., Simoncelli, E. P., & Movshon, A. (2013). A functional and perceptual signature of the second visual area in primates. *Nature Neuroscience, 16*(7), 974-+. doi:10.1038/nn.3402

Geisler, W. S. (2008). Visual perception and the statistical properties of natural scenes. *Annual Review of Psychology, 59*, 167-192. doi:10.1146/annurev.psych.58.110405.085632

Ghodrati, M., Ghodousi, M., & Yoonessi, A. (2016). Low- Level Contrast Statistics of Natural Images Can Modulate the Frequency of Event- Related Potentials (ERP) in Humans. *Frontiers in Human Neuroscience, 10*. doi:10.3389/fnhum.2016.00630

Harrison, W. J. (2022). Luminance and Contrast of Images in the THINGS Database. *Perception, 51*(4), 244-262. doi:10.1177/03010066221083397

Hatfield, G., & Allred, S. (2012). Introduction: Visual Experience. In G. Hatfield & S. Allred (Eds.), *Visual Experience: Sensation, Cognition and Constancy* (pp. 253). Oxford, UK: Oxford University Press.

Himmelberg, M. M., Winawer, J., & Carrasco, M. (2020). Stimulus-dependent contrast sensitivity asymmetries around the visual field. *Journal of Vision, 20*(9). doi:10.1167/jov.20.9.18

Hoekstra, J., van der Goot, D. P. J., van den Brink, G., & Bilsen, F. A. (1974). The influence of the number of cycles upon the visual contrast threshold for sptial sine wave patterns. *Vision Research, 14*(6), 365-368. doi:https://doi.org/10.1016/0042-6989(74)90234-X

Jennings, B. J., & Kingdom, F. A. A. (2017). Chromatic blur perception in the presence of luminance contrast. *Vision Research, 135*, 34-42. doi:10.1016/j.visres.2017.04.006

Johnson, R. P. (1990). Contrast Based Edge Detection. *Pattern Recognition, 23*(3-4), 311-318. doi:10.1016/0031-3203(90)90018-g

Johnston, A. (1987). Spatial Scaling of Central and Peripheral Contrast Sensitivity Functions. *Journal of the Optical Society of America a-Optics Image Science and Vision, 4*(8), 1583-1593. doi:10.1364/josaa.4.001583

Kaplan, E. (2013). The M, P and K pathways of the Primate Visual System revisited. In.

Kaplan, E., Lee, B. B., & Shapley, R. M. (1990). Chapter 7 New views of primate retinal function. *Progress in Retinal Research, 9*, 273-336. doi:https://doi.org/10.1016/0278-4327(90)90009-7

Kaplan, E., & Shapley, R. M. (1982). X-Cell and Y-Cell in the Lateral Geniniculate Nucleus of Macaque Monkeys. *Journal of Physiology-London, 330*(SEP), 125-143. doi:10.1113/jphysiol.1982.sp014333

Kaplan, E., & Shapley, R. M. (1986). The Primate Retina Contains Two Types of Ganglion Cells, With High and Low Contrast Sensitivity. *Proceedings of the National Academy of Sciences of the United States of America, 83*(8), 2755-2757. doi:10.1073/pnas.83.8.2755

Kelly, D. H. (1961). Visual Responses to Tme-Dependent Stimuli. 1. Amplitude Sensitivity Measurements. *Journal of the Optical Society of America, 51*(4), 422-&. doi:10.1364/josa.51.000422

Kelly, D. H. (1984). Retinal Inhomogeneity. 1. Spatiotemporal Contrast Sensitivity. *Journal of the Optical Society of America a-Optics Image Science and Vision, 1*(1), 107-113. doi:10.1364/josaa.1.000107

Kleiner, M., Brainard, D., & Pelli, D. (2007). What's new in Psychtoolbox-3? *Perception, 36*, 14-14.

Koenderink, J. J., Bouman, M. A., Buenodemesquita, A. E., & Slappendel, S. (1978). Perimetry of Contrast Detection Thresholds of Moving Spatial Sine Wave Patterns. 2. Far Peripheral Visual Field (Eccentricity 0 Degrees to 50 Degrees). *Journal of the Optical Society of America, 68*(6), 850-854. doi:10.1364/josa.68.000850

Kulikowski, J. J. (1987). *The Role of the P and M Systems (c) Psychophysical Aspects.* Paper presented at the Third International Symposium of the Northern Eye Institute, Manchester, England.

Kulikowski, J. J., & Tolhurst, D. J. (1973). Psychophysical Evidence for Sustained and Transient Detectors in Human Vision. *Journal of Physiology-London, 232*(1), 149-162. doi:10.1113/jphysiol.1973.sp010261

Lagarias, J. C., Reeds, J. A., Wright, M. H., & Wright, P. E. (1998). Convergence properties of the Nelder-Mead simplex method in low dimensions. *Siam Journal on Optimization, 9*(1), 112-147. doi:10.1137/s1052623496303470

Lalor, E. C., & Foxe, J. J. (2009). Visual evoked spread spectrum analysis (VESPA) responses to stimuli biased towards magnocellular and parvocellular pathways. *Vision Research, 49*(1), 127-133. doi:10.1016/j.visres.2008.09.032

Lee, B. B. (2019). Sensitivity to chromatic and luminance contrast and its neuronal substrates. *Current Opinion in Behavioral Sciences, 30*, 156-162. doi:10.1016/j.cobeha.2019.08.006

Legge, G. E. (1978). Sustained and Transient Mechanisms in Human Vision – Temporal and Spatial Properties. *Vision Research, 18*(1), 69-81. doi:10.1016/0042-6989(78)90079-2

Leonova, A., Pokorny, J., & Smith, V. C. (2003). Spatial frequency processing in inferred PC- and MC-pathways. *Vision Research, 43*(20), 2133-2139. doi:10.1016/s0042-6989(03)00333-x

Li, R., Ge, J. J., & Wang, Z. Q. (2012). The study on neural contrast sensitivity function at temporal frequencies. *Optik, 123*(4), 343-347. doi:10.1016/j.ijleo.2011.03.030

Lindgren, J. T., Hurri, J., & Hyvarinen, A. (2008). Spatial dependencies between local luminance and contrast in natural images. *Journal of Vision, 8*(12). doi:10.1167/8.12.6

Livingstone, M. S., & Hubel, D. H. (1987). Psychophysical Evidence for Separate Channels for the Perecption of Form, Color, Movement and Depth. *Journal of Neuroscience, 7*(11), 3416-3468.

Lourens, T. (1995). Modeling retinal high and low contrast sensitivity filters. *From Natural to Artificial Neural Computation, 930*, 61-68.

Martin, F., & Lovegrove, W. (1984). The Effects of Field Size and Luminance on Contrast Sensitivity Differences Between Specifically Reading Disabled and Normal Children. *Neuropsychologia, 22*(1), 73-77. doi:10.1016/0028-3932(84)90009-5

Martin, P., & Grunert, U. (2003). Ganglion Cells in Mammalian Retinae. In L. Chalupa & J. Werner (Eds.), *The Visual Neurosciences* (Vol. 1, pp. 410-421). Cambridge, Massachusetts, USA: The MIT Press.

McKendrick, A. M., & Johnson, C. A. (2000). Aliasing for rapidly counterphasing stimuli: a failure to demonstrate an M-cell sampling limit to resolution. *Journal of the Optical Society of America a-Optics Image Science and Vision, 17*(10), 1703-1712. doi:10.1364/josaa.17.001703

Merigan, W. H., & Maunsell, J. H. R. (1993). How parallel are the Primate Visual Pathways. *Annual Review of Neuroscience, 16*, 369-402. doi:10.1146/annurev.ne.16.030193.002101

Murray, I. J., & Plainis, S. (2003). Contrast coding and magno/parvo segregation revealed in reaction time studies. *Vision Research, 43*(25), 2707-2719. doi:10.1016/s0042-6989(03)00408-5

Navarro, R., Artal, P., & Williams, D. R. (1993). Modulation Transfer of the Human Eye as a Function of Retinal Eccentricity. *Journal of the Optical Society of America a-Optics Image Science and Vision, 10*(2), 201-212. doi:10.1364/josaa.10.000201

Peli, E. (1990). Contrast in Complex Images. *Journal of the Optical Society of America a-Optics Image Science and Vision, 7*(10), 2032-2040. doi:10.1364/josaa.7.002032

Pinna, B. (2005). The role of the Gestalt principle of similarity in the watercolor illusion. *Spatial Vision, 18*(2), 185-207. doi:10.1163/1568568053320639

Plainis, S., & Murray, I. J. (2005). Magnocellular channel subserves the human contrast-sensitivity function. *Perception, 34*(8), 933-940. doi:10.1068/p5451

Pokorny, J. (2011). Steady and pulsed pedestals, the how and why of post-receptoral pathway separation. *Journal of Vision, 11*(5). doi:10.1167/11.5.7

Pokorny, J., & Smith, V. C. (1997). Psychophysical signatures associated with magnocellular and parvocellular pathway contrast gain. *Journal of the Optical Society of America a-Optics Image Science and Vision, 14*(9), 2477-2486. doi:10.1364/josaa.14.002477

Robson, J. G. (1966). Spatial and Temporal Contrast sensitivity Functions of the Visual System. *Journal of the Optical Society of America, 56*(8), 1141-&. doi:10.1364/josa.56.001141

Rodieck, R. W. (1965). Quantitative analysis of cat retinal ganglion cell response to visual stimuli. *Vision Research, 5*(12), 583-601. doi:https://doi.org/10.1016/0042-6989(65)90033-7

Rovamo, J., Franssila, R., & Nasanen, R. (1992). Contrast Sensitivity as a Function of Spatial frequency, Vieiwing Distance and Eccentricity With and Without Spatial Noise. *Vision Research, 32*(4), 631-637. doi:10.1016/0042-6989(92)90179-m

Rovamo, J., Virsu, V., & Nasanen, R. (1978). Cortical Magnification Factor Predicts Photopic Contrast sensitivity of Peripheral Vision. *Nature, 271*(5640), 54-56. doi:10.1038/271054a0

Ruderman, D. L. (1994). The Statistics of Natural Images. *Network-Computation in Neural Systems, 5*(4), 517-548. doi:10.1088/0954-898x/5/4/006

Scholte, H. S., Ghebreab, S., Waldorp, L., Smeulders, A. W. M., & Lamme, V. A. F. (2009). Brain responses strongly correlate with Weibull image statistics when processing natural images. *Journal of Vision, 9*(4). doi:10.1167/9.4.29

Schutt, H. H., Harmeling, S., Macke, J. H., & Wichmann, F. A. (2016). Painfree and accurate Bayesian estimation of psychometric functions for (potentially) overdispersed data. *Vision Research, 122*, 105-123. doi:10.1016/j.visres.2016.02.002

Sekuler, R., & Blake, R. (2006). *Perception / Randolph Blake, Robert Sekuler* (5th ed.). Boston: McGraw-Hill.

Shannon, C. E. (1949). Communication in the Presence of Noise. *Proceedings of the Institute of Radio Engineers, 37*(1), 10-21. doi:10.1109/jrproc.1949.232969

Skottun, B. C. (2015). On the use of spatial frequency to isolate contributions from the magnocellular and parvocellular systems and the dorsal and ventral cortical streams. *Neuroscience and Biobehavioral Reviews, 56*, 266-275. doi:10.1016/j.neubiorev.2015.07.002

Solomon, S. G., & Lennie, P. (2007). The machinery of colour vision. *Nature Reviews Neuroscience, 8*(4), 276-286. doi:10.1038/nrn2094

Thibos, L. N., Cheney, F. E., & Walsh, D. J. (1987). Retinal Limits to the Detection and Resolution of Gratings. *Journal of the Optical Society of America a-Optics Image Science and Vision, 4*(8), 1524-1529. doi:10.1364/josaa.4.001524

To, M. P. S., Lovell, P. G., Troscianko, T., & Tolhurst, D. J. (2010). Perception of suprathreshold naturalistic changes in colored natural images. *Journal of Vision, 10*(4). doi:10.1167/10.4.12

Tolhurst, D. J. (1975). Syustained and Transient Channels in Human Vision. *Vision Research, 15*(10), 1151-1155. doi:10.1016/0042-6989(75)90014-0

Virsu, V., Rovamo, J., Laurinen, P., & Nasanen, R. (1982). Temporal Contrast Sensitivity and Cortical Magnification. *Vision Research, 22*(9), 1211-1217. doi:10.1016/0042-6989(82)90087-6

Wagenmakers, E. J., & Farrell, S. (2004). AIC model selection using Akaike weights. *Psychonomic Bulletin & Review, 11*(1), 192-196. doi:10.3758/bf03206482

Wallis, T. S. A., Bethge, M., & Wichmann, F. A. (2016). Testing models of peripheral encoding using metamerism in an oddity paradigm. *Journal of Vision, 16*(2). doi:10.1167/16.2.4

Wandell, B. A., & Winawer, J. (2015). Computational neuroimaging and population receptive fields. *Trends in cognitive sciences, 19*(6), 349-357. doi:10.1016/j.tics.2015.03.009

Watson, A. B. (2014). A formula for human retinal ganglion cell receptive field density as a function of visual field location. *Journal of Vision, 14*(7). doi:10.1167/14.7.15

Westheimer, G. (1960). Modulation Thresholds for Sinusoidal Light Distributions on the Retina. *Journal of Physiology-London, 152*(1), 67-74. doi:10.1113/jphysiol.1960.sp006469

Wilkinson, M. O., Anderson, R. S., Bradley, A., & Thibos, L. N. (2016). Neural bandwidth of veridical perception across the visual field. *Journal of Vision, 16*(2). doi:10.1167/16.2.1

Williams, D. R., Artal, P., Navarro, R., McMahon, M. J., & Brainard, D. H. (1996). Off-axis optical quality and retinal sampling in the human eye. *Vision Research, 36*(8), 1103-1114. doi:10.1016/0042-6989(95)00182-4

Zhaoping, L. (2018). *Understanding Vision: Theory Models and Data*. Oxford, UK: Oxford University Press.

Zhu, H. F., Zele, A. J., Suheimat, M., Lambert, A. J., & Atchison, D. A. (2016). Peripheral detection and resolution with mid-/long-wavelength and short-wavelength sensitive cone systems. *Journal of Vision, 16*(10). doi:10.1167/16.10.21

## Appendix A

|  | Model | Function | Curve | Freq dep | Paras | n | AICc | ΔAICc | AW |
|---|---|---|---|---|---|---|---|---|---|
| JW | G1 | Freq Gauss | Single | Ind | 4 | 71 | -296.6 | 164.2 | 0.00 |
|  | G2 | Freq Gauss | Single | Dep | 7 | 71 | -364.7 | 96.1 | 0.00 |
|  | G3 | Freq Gauss | Dual | Ind | 7 | 71 | -346.3 | 114.5 | 0.00 |
|  | G4 | Freq Gauss | Dual | Dep | 12 | 71 | -460.8 | 0.0 | 0.83 |
|  | G5 | Freq Gauss | Dual | Dep | 13 | 71 | -457.7 | 3.1 | 0.17 |
|  | P1 | Power law | Single | Ind | 4 | 71 | -355.1 | 105.7 | 0.00 |
|  | P2 | Power law | Single | Dep | 7 | 71 | -394.1 | 66.7 | 0.00 |
|  | P3 | Power law | Dual | Ind | 7 | 71 | -365.8 | 95.0 | 0.00 |
|  | P4 | Power law | Dual | Dep | 12 | 71 | -437.9 | 22.9 | 0.00 |
|  | P5 | Power law | Dual | Dep | 13 | 71 | -435.9 | 24.9 | 0.00 |
|  |  |  |  |  |  |  |  |  |  |
| NM | G1 | Freq Gauss | Single | Ind | 4 | 55 | -228.1 | 78.7 | 0.00 |
|  | G2 | Freq Gauss | Single | Dep | 7 | 55 | -263.7 | 43.1 | 0.00 |
|  | G3 | Freq Gauss | Dual | ind | 7 | 55 | -227.1 | 79.7 | 0.00 |
|  | G4 | Freq Gauss | Dual | Dep | 12 | 55 | -306.8 | 0.0 | 0.66 |
|  | G5 | Freq Gauss | Dual | Dep | 13 | 55 | -304.0 | 2.8 | 0.16 |
|  | P1 | Power law | Single | Ind | 4 | 55 | -233.1 | 73.7 | 0.00 |
|  | P2 | Power law | Single | Dep | 7 | 55 | -259.9 | 46.9 | 0.00 |
|  | P3 | Power law | Dual | Ind | 7 | 55 | -233.7 | 73.1 | 0.00 |
|  | P4 | Power law | Dual | Dep | 12 | 55 | -294.2 | 12.6 | 0.00 |
|  | P5 | Power law | Dual | Dep | 13 | 55 | -304.1 | 2.6 | 0.18 |
|  |  |  |  |  |  |  |  |  |  |
| TH | G1 | Freq Gauss | Single | Ind | 4 | 44 | -192.6 | 39.8 | 0.00 |
|  | G2 | Freq Gauss | Single | Dep | 6 | 44 | -206.0 | 26.3 | 0.00 |
|  | G3 | Freq Gauss | Dual | Ind | 7 | 44 | -204.6 | 27.8 | 0.00 |
|  | G4 | Freq Gauss | Dual | Dep | 10 | 44 | -232.4 | 0.0 | 0.65 |
|  | G5 | Freq Gauss | Dual | Dep | 11 | 44 | -230.6 | 1.8 | 0.27 |
|  | P1 | Power law | Single | Ind | 4 | 44 | -213.7 | 18.7 | 0.00 |
|  | P2 | Power law | Single | Dep | 6 | 44 | -220.4 | 11.9 | 0.00 |
|  | P3 | Power law | Dual | Ind | 7 | 44 | -208.4 | 24.0 | 0.00 |
|  | P4 | Power law | Dual | Dep | 10 | 44 | -227.7 | 4.7 | 0.06 |
|  | P5 | Power law | Dual | Dep | 11 | 44 | -224.2 | 8.2 | 0.01 |

Table A1. Comparison of the AIC$_c$ values and Akaike weights for each model, for the three participants, with the "Best" model highlighted in green, and the "Next Best" in yellow. *G1, P1* etc are model labels referring to the model type (Gaussian or Power Law), as shown in the next column, *Single/Dual* refers to single or dual-segment functions, *Ind/Dep* refers to whether the model is independent or dependent on temporal frequency, *Paras* defines the number of parameters in the model, *n* is the number of datapoints, *AIC$_c$* is the corrected Akaike Information content coefficient, Δ*AIC$_c$* is the difference between the model AIC value and the lowest value in the set and *AW* is the Akaike Weight.

| Model | Function | Curve | Freq dep/ind | Multi/Add | Paras | n | AICc | ΔAIC | AW |
|-------|----------|-------|--------------|-----------|-------|-----|--------|------|------|
| G6 | Freq Gauss | Single | Dep | Multi | 9 | 170 | -830.9 | 67.5 | 0.00 |
| G7 | Freq Gauss | Dual | Dep | Multi | 16 | 170 | -898.4 | 0.0 | 0.71 |
| G8 | Freq Gauss | Dual | Dep | Multi | 17 | 170 | -892.6 | 5.8 | 0.04 |
| G9 | Freq Gauss | Dual | Dep | n/a | 34 | 170 | -885.4 | 13.1 | 0.00 |
| G10 | Freq Gauss | Dual | Dep | Add | 16 | 170 | -896.1 | 2.3 | 0.23 |
| P6 | Power law | Single | Dep | Multi | 9 | 170 | -853.2 | 45.2 | 0.00 |
| P7 | Power law | Dual | Dep | Multi | 16 | 170 | -887.0 | 11.4 | 0.00 |
| P8 | Power law | Dual | Dep | Multi | 17 | 170 | -891.3 | 7.1 | 0.02 |

Table B1. Comparison of AICc values and Akaike weights for Gaussian and Power Law base models, with multiplicative or additive parameters for the other two participants (NM, TH) for the full (combined) dataset, with the "Best" model highlighted in green, and the "Next Best" in yellow. The column headings have the same meanings as for Table 1, with the addition of Multi/Add which defines whether the two additional parameters per participant are multiplicative or additive fits to the cut-off wavelength values. Note that for model G9 (32 parameters) there are no scale/add corrections, as this model fully describes each individual participants data set.